EXPERIMENTAL CHARACTERIZATION AND MOLECULAR STUDY OF NATURAL GAS MIXTURES

A Dissertation

by

DIEGO EDISON CRISTANCHO BLANCO

Submitted to the Office of Graduate Studies of
Texas A&M University
in partial fulfillment of the requirements for the degree of

DOCTOR OF PHILOSOPHY

May 2010

Major Subject: Chemical Engineering

EXPERIMENTAL CHARACTERIZATION AND MOLECULAR STUDY OF NATURAL GAS MIXTURES

A Dissertation

by

DIEGO EDISON CRISTANCHO BLANCO

Submitted to the Office of Graduate Studies of
Texas A&M University
in partial fulfillment of the requirements for the degree of

DOCTOR OF PHILOSOPHY

Approved by:

Chair of Committee,	Kenneth R. Hall
Committee Members,	Perla Balbuena
	Maria Barrufet
	Tahir Cagin
Head of Department,	Michael Pishko

May 2010

Major Subject: Chemical Engineering

ABSTRACT

Experimental Characterization and Molecular Study of Natural Gas Mixtures

(May 2010)

Diego Edison Cristancho Blanco, B.S.; B.S.; M.S.,

Universidad Industrial de Santander, Colombia

Chair of Advisory Committee: Dr. Kenneth R. Hall

Natural Gas (NG) plays an important role in the energy demand in the United States and throughout the world. Its characteristics as a clean, versatile and a sustainable source of energy makes it an important alternative within the spectra of energy resources. Addressing industrial and academic needs in the natural gas research area requires an integrated plan of research among experimentation, modeling and simulation. In this work, high accuracy $P\rho T$ data have been measured with a high pressure single sinker magnetic suspension densimeter. An entire uncertainty analysis of this apparatus reveals that the uncertainty of the density data is less that 0.05% across the entire ranges of temperature (200 to 500) K and pressure (up to 200 MPa). These characteristics make the $P\rho T$ data measured in this study unique in the world. Additionally, both a low pressure (up to 35 MPa) and a high pressure (up to 200 MPa) isochoric apparatus have been developed during the execution of this project. These apparatuses, in conjunction with a recently improved isochoric technique, allow determination of the phase envelope for NG mixtures with an uncertainty of 0.45% in temperature, 0.05% in pressure and 0.12% in density. Additionally, an innovative technique, based upon Coherent Anti-Stokes Raman Scattering (CARS) and Gas Chromatography (GC), was proposed in this research to minimize the high uncertainty introduced by the composition analyses of NG mixtures. The collected set of $P\rho T$ and saturation data are fundamental for thermodynamic formulations of these mixtures. A study at the molecular level has provided molecular data for a selected set of main

constituents of natural gas. A 50-50% methane-ethane mixture was studied by molecular dynamics simulations. The result of this study showed that simulation time higher than 2 ns was necessary to obtain reasonable deviations for the density determinations when compared to accurate standards. Finally, this work proposed a new mixing rule to incorporate isomeric effects into cubic equations of state.

DEDICATION

To
Jennifer, Juan Diego
and
Our Families

ACKNOWLEDGMENTS

I hereby wish to thank Dr. Kenneth R. Hall for giving me the opportunity to work on this project and for his advice, both professional and personal. I appreciate his patience and understanding during the difficult times with the project. I am grateful to Dr. Hall for financially supporting me for last 4 years and making it possible for me to obtain my degrees at Texas A&M University. I would like to thank my advisory committee members, Dr. Maria A. Barrufet, Dr. Perla Balbuena, and Dr. Tahir Cagin, and Dr James Holste, for their time and advices.

I would like to gratefully acknowledge the contributions of Dr. Mark O. McLinden and Dr. Eric W. Lemmon of the National Institute of Standards and Technology (NIST) for their technical support in calibrating our apparatus parts and for providing us access to the Reference Properties (REFPROP) programs. I also thank them for their friendship and advice during my internship in the NIST at Boulder, Colorado.

I would like to extend my appreciation for the help I received from the various people in the department, directly or indirectly related to my research. I would like to express my sincere gratitude to Mr. Randy A. Marek of the machine shop who helped us with our mechanical works, and Mr. Jason W. Caswell of the physics electronic shop for spending countless hours with us advising on electrical and electronic problems and advancements of our experimental setup.

I am indebted to all my colleagues in the research group for the valuable time spent with them. I appreciate the help I received from Dr. Mert Atilhan and Dr. Saquib Ejaz during the early stages of my lab experience. I find myself extremely lucky to have worked with Mr. Ali Abedi, Mr. Ivan Mantilla, Mr. Diego Ortiz, Mr. Alejandro Coy, Mrs. Andrea Tibaduiza, Mr. Pedro Acosta, and Mr. Ullas Pathak, in the same research group. I would like to thank them here for their help, time and friendship.

I am very indebted and grateful to my parents Jose Rafael Cristancho and Audrey Blanco for their support and understanding. I thank them hereby for teaching me how to pursue real happiness. Also, I would like to extend my appreciation to my mother-in-

law, Edda Diaz, for her support and understanding in all respects. I send thanks to my brother Byron Cristancho, and sister Deissy Cristancho, for being role models for me throughout all stages of my life. I also thank my brother-in-law Mauricio Diaz, for his support.

Above all, I find myself fortunate to have such a wonderful wife Jennifer Carvajal, and son, Juan Diego Cristancho. They have been the driving force that makes me look for a better world every day. They create an environment of love, understanding, friendship, and motivation around me, leading my life always to a better state.

NOMENCLATURE

a	Calibration constant in the deviation equations of ITS-90 for a PRT or coil radius (in)
b	Calibration constant in the deviation equations of ITS-90 for a PRT
B	Second virial coefficient (cm^3/mole) or Constant in the reference function of ITS-90 for a PRT calibration
C	Third virial coefficient $(cm^3/mole)^2$
C_p	Isobaric heat capacity
C_v	Isochoric heat capacity
I	Current through platinum resistance thermometer (mA)
m	Mass of sinker (g)
M	Molar mass (kg/kmole) or magnetic moment
n	Number of moles
N	Number of components in a natural gas mixture or constant in a polynomial equation
P, p	Pressure (MPa) [psia]
R	Resistance of platinum resistance thermometer (ohm) or universal gas constant (8.314 J/mole K)
T	Temperature (K)
u	Uncertainty or speed of sound
V	Volume of sinker (cm^3) or voltage drop, volt
W	Ratio of the resistance of a platinum resistance thermometer at a temperature to its resistance at the triple point of water or balance reading or weight
x	Composition as mole fraction

Abbreviations

AC	Alternating Current
AGA	American Gas Association
AGA8-DC92	Detailed Characterization Method of the American Gas Association
BP	British Petroleum
CARS	Coherent Anti-Stokes Raman Scattering
CB	Cricondenbar
CP	Critical Point
CT	Cricondentherm
DC	Direct Current
DMM	Digital Multimeter
DPI	Differential Pressure Indicator
EoS	Equation of State
FT	Fischer-Tropsch
FTE	Force Transmission Error
FWM	Four Wave Mixing Signal
GERG	European Group for Gas Research
GERG-2004	GERG-2004 EOS for gas mixtures
GTL	Gas to Liquids
GTE	Gas to Ethylene
HIP	High Pressure Equipment Company
HP	Hand Pump
IC	Isochore
IEA	International Energy Agency
IT	Isotherm
ITS-90	International Temperature Scale of 1990
LNG	Liquefied Natural Gas
LVDT	Linear Variable Differential Transformer

MP	Measurement Point
MSD	Magnetic Suspension Densimeter
NIST	National Institute of Standards and Technology
NR	Non-Resonant
PID	Proportional Integral Derivative
PPM	Parts Per Million
PRT	Platinum Resistance Thermometer
PT6K	6,000 psia Range Pressure Transducer
PT30K	30,000 psia Range Pressure Transducer
SSR	Solid State Relay
T	Tee Fitting
Ta	Tantalum
Ti	Titanium
V	Valve
ZP	Zero Point

Greek letters

β	Temperature distortion coefficient (K^{-1}) or thermal coefficient of expansion (K^{-1}) or balance calibration factor
κ	Pressure distortion coefficient (MPa^{-1})
Δ	Difference or deviation
X	Internal temperature period of pressure transducer quartz crystal (μs)
ρ	Density (kg/m^3)
ρ'	Saturation density (kg/m^3)
σ	Standard deviation or deviation at the 68% confidence level or normal stress
φ	Coupling factor
ϕ_0	Apparatus contribution to the force transmission error

ε	Apparatus fluid specific constant (ppm) or strain (inch/inch)
χ	Magnetic susceptibility, m^3/kg
ω	Frequency
γ	Noxious volume to cell volume ratio

Subscripts

0	Index for constants *B* and *D* in reference functions of ITS-90 for PRT calibration
6+	Hexane and components heavier than hexane such as heptane, octane, etc
i	Component number or index for constants in the reference function of ITS-90 for PRT calibration
e-mag	Electromagnet
o	Reference condition of 23 ^oC for cross sectional area of piston cylinder assembly of dead weight gauge or reference condition of 20 ^oC and 1 bar pressure for sinker volume
p-mag	Permanent magnet
ref	Reference state
s	Initial set-point
S	Sinker
v	Vacuum condition

TABLE OF CONTENTS

Page

ABSTRACT iii

DEDICATION v

ACKNOWLEDGMENTS vi

NOMENCLATURE viii

TABLE OF CONTENTS xii

LIST OF FIGURES xiv

LIST OF TABLES xviii

INTRODUCTION 1

1.1 Economic Impact of Natural Gas In the United States and In the World 1
1.2 Objectives of the Current Research 5

EQUATIONS OF STATE FOR NATURAL GAS APPLICATIONS 7

2.1 State of the art for EoS 7
2.2 Multiparameter EoS 10
2.2.1 GERG-2004 14
2.3 The Quintic Equation of State 16

EXPERIMENTAL CHARACTERIZATION OF NATURAL GAS MIXTURES 23

3.1 $P\rho T$ Data 23
3.1.1 Force Transmission Error Analysis 25
3.1.1.1 Theoretical Model 26
3.1.1.2 Experimental 30
3.1.1.3 Results and Analysis 31
3.1.2 Pure Compounds $P\rho T$ Data 36
3.1.2.1 Accurate $P\rho T$ Data for Methane From (300 to 450) K Up to 180Mpa 36
3.1.2.1.1 Results and Analysis 37
3.1.2.2 Accurate $P\rho T$ Data for Ethane From

(298 to 450) K Up to 200 MPa……..... 44

Page

3.1.2.2.1 Results and Analysis…… 45
3.2 Isochoric and Phase Equilibrium Data…….. 50
3.2.1 Low Pressure Isochoric Apparatus……... 51
3.2.2 High Pressure Isochoric Apparatus…….. 52
3.2.2.1 Temperature Control……... 57
3.2.3 Phase Loop Determination Technique……. 61
3.2.3.1 Technique……. 62
3.2.3.2 Uncertainties in Temperature and Pressure…….. 64
3.2.3.3 Results and Analysis……. 65
3.2.4 Saturated Density Determination and Isochoric Derivative Corrections……... 70
3.3 Composition Data…….. 78
3.3.1 Coherent Anti-Stokes Raman Scattering (CARS)…… 79

EXPERIMENTAL RESULTS FOR SYNTHETIC NATURAL GAS MIXTURES 85

4.1 Ternary $P\rho T$ Data……... 85
4.1.1 Experimental ……..... 86
4.1.2 Results and Analysis …… 86
4.2 Synthetic Natural Gas ……... 93
4.3 High Pressure Isochoric Data for a Pipeline Sample……. 107

MOLECULAR STUDY OF NATURAL GAS MIXTURES……. 112

5.1 Molecular Dynamics Simulations…….. 116
5.2 Conformational Analysis and New Mixing Rule……... 118

CONCLUSIONS AND RECOMMENDATIONS……. 123

REFERENCES…… 126

APPENDIX A……. 138

APPENDIX B……. 140

APPENDIX C……. 142

VITA …….. 150

LIST OF FIGURES

Page

Figure 1. Monthly consumption, production, imports and exports in the US.. ... 1

Figure 2. Consumption of energy from different sources US 2

Figure 3. U.S. primary natural gas consumption by sector 3

Figure 4. PT, PTV, SW, GD, MMM EoS predictions for synthetic natural gas mixture. 4

Figure 5. Temperature-density diagram for the propylene glycol EoS and propane EoS…..... 12

Figure 6. Cvr-temperature diagram for propylene glycol EoS and propane EoS…..... 13

Figure 7. High pressure single-sinker magnetic suspension densimeter. 24

Figure 8. Apparatus constant calculations based on experimental data measured in the high pressure single sinker MSD..... 27

Figure 9. Operation of the single-sinker MSD: a) Suspension control (SC) 'off', Ti and Ta both raised, (b) SC 'on' zero position (ZP), Ta lowered, Ti raised, (c) Measuring position, SC 'on', Ta raised, Ti lowered. 28

Figure 10. Titanium sinker raw densities ($\phi = 1$) deviations..... 32

Figure 11. Copper sinker raw densities ($\phi = 1$) deviations..... 32

Figure 12. $(\phi - \phi_0)$ Values for the two-sinkers experiment. 34

Figure 13. Titanium sinker corrected densities deviations.. 34

Figure 14. Copper sinker corrected densities deviations.. 35

Figure 15. Percentage deviation of the experimental $P\rho T$ data from values calculated using Setzmann and Wagner.. 41

Figure 16. Procedure for the determination of the second virial coefficient using 298 K data 42

Page

Figure 17. Absolute deviations for second virial coefficient from values calculated using the Setzmann and Wagner equation of state $\Delta B = (B_{exp} - B_{calc})$ 43

Figure 18. Absolute deviations for third virial coefficient from values calculated using the Setzmann and Wagner [35] equation of state $\Delta C = (C_{exp} - C_{calc})$..... 43

Figure 19. Percentage deviation of the experimental $P\rho T$ data from values calculated using the Bücker and Wagner equation of state..... 48

Figure 20. Absolute deviations for second virial coefficient from values calculated using the Bücker and Wagner equation of state $\Delta B = (B_{exp} - B_{calc})$ 49

Figure 21. Absolute deviations for third virial coefficient from values calculated using the Bücker and Wagner equation of state $\Delta C = (C_{exp} - C_{calc})$. ... 49

Figure 22. Low-pressure isochoric apparatus. 52

Figure 23. Cut view of new isochoric apparatus 53

Figure 24. High pressure isochoric apparatus. 54

Figure 25. Feeding section of both the MSD and the high-pressure isochoric apparatus…. 54

Figure 26. High pressure isochoric manifold. 55

Figure 27. Isochoric cell and pressure transducer configuration. 56

Figure 28. Vacuum system. 57

Figure 29. Isochoric apparatus cut view. 59

Figure 30. Temperature control methodology. 60

Figure 31. Control box set-up. 60

Figure 32. Pressure residuals in the single and two-phase region: Solid circles are single phase data and hollow circles are two-phase data. 63

Figure 33. Interval errors for the pressure and temperature. 64

Page

Figure 34. Phase envelope for a 7-component natural gas mixture near the criconderbar. 65

Figure 35. Phase envelope for a 22-component natural gas mixture. 68

Figure 36. Percentage deviation of the phase boundary temperature. natural gas mixtures. 69

Figure 37. Percentage deviation in the calculation of the phase boundary pressure 69

Figure 38. Schematic of the mass interchange in the low-pressure isochoric apparatus…. 71

Figure 39. Methodology to determine the number of moles for calculating saturation densities. 72

Figure 40. Temperature, pressure and composition contribution to the total density uncertainty for a synthetic natural gas mixture at 1σ 78

Figure 41. CARS energy scheme. 80

Figure 42. CARS gas chamber. 81

Figure 43. Setup schematics. 82

Figure 44. CARS spectrogram. 83

Figure 45. CARS spectra normalized on the reference FWM profiles. 84

Figure 46. Percentage deviations of the experimental $P\rho T$ data from values calculated using the GERG-2004 and AGA8-DC2 89

Figure 47. Isochoric experimental design. 90

Figure 48. Experimental phase boundary.. 90

Figure 49. Experimental temperature-density diagram. 91

Figure 50. Relative deviations of the corrected (*dP/dT)* derivative compared to GERG-2004. 92

Page

Figure 51. Sample 1 density deviations. 101

Figure 52. Sample 2 density deviations 102

Figure 53. Sample 3 density deviations 103

Figure 54. Sample 4 density deviations. 104

Figure 55. Phase boundaries for the samples ♦ 1, ● 2, ▼ 3, ★ 4. 106

Figure 56. Temperature-density boundaries for the samples ♦ 1, ● 2, ▼ 3, ★ 4. 107

Figure 57. Density predictions for methane-ethane mixture. 117

Figure 58. Density deviations for methane-ethane mixture at 5 bar and 298 K. ... 117

Figure 59. Density deviations for methane-ethane mixture. 118

Figure 60. Radial distribution functions for methane-ethane mixture at 1 bar and 298 K… 119

Figure 61. Compressibility factor deviations from new Redlich-Kwong EOS at 400 K….. 121

Figure 62. Compressibility factor deviations for the new Redlich-Kwon EoS at 420 K….. 122

Figure 63. Compressibility factor deviations for the new Redlich-Kwon EOS at 450 K… 122

LIST OF TABLES

Page

Table 1. Economic Impact Of NG Custody Transfer 5

Table 2. Estimated Relative Experimental Uncertainties of the Most Accurate Binary and Multicomponent Mixture Data 15

Table 3. Mathematical Combinations for Functions $F_1(\rho)$ and $F_2(\rho)$ 18

Table 4. Two Sinkers Experiment Temperatures. 31

Table 5. Measured Density Values for Methane. 37

Table 6. Second and Third Virial Coefficients for Methane 44

Table 7. Measured Density Values for Ethane. 45

Table 8. Second and Third Virial Coefficients for Ethane. 50

Table 9. Low Pressure Isochoric Apparatus Features. 51

Table10. Comparison Between Determined Boundary Pressures and Temperatures and Literature Values. 66

Table 11. Low and High Pressure Isochoric Apparatus Parameters 72

Table 12. CARS Gas Chamber Characteristics. 81

Table 13. Density Values. 87

Table 14. Second and Third Virial Coefficients 89

Table 15. Binary Coefficient Parameters for Peng –Robinson Eos 91

Table 16. Phase Boundary Data 92

Table 17. Mixture Compositions (Mole Fraction). 93

Table 18. *Pρt* Data for Sample 1. 94

Table 19. *Pρt* Data for Sample 2. 95

Page

Table 20. *Pρt* Data for Sample 3 97

Table 21. *Pρt* Data for Sample 4 99

Table 22. Phase Boundary Data for the Sample 1. 105

Table 23. Phase Boundary Data for the Sample 2. 105

Table 24. Phase Boundary Data for the Sample 3. 105

Table 25. Phase Boundary Data for the Sample 4 106

Table 26. Pipeline Composition 108

Table 27. Isochoric 1 Experimental Data. 108

Table 28. Isochoric 2 Experimental Data. 109

Table 29. Phase Boundary Data for the Isochoric 2. 111

Table 30. Natural Gas Main Constituents 114

Table 31. Dipole Moment, Quadrupole Moment and Isotropic Polarizability for the Main Constituents of Natural Gas. 115

Table 32. Isomeric Data for Heptane Using Redlich-Kwong EOS 121

INTRODUCTION

1.1 Economic Impact of Natural Gas In the United States and In the World

Currently, all segments of society have a strong dependence upon energy. Figure 1 reveals a remarkable difference between consumption and production of energy over the last fifty years in the US [1]. Energy import in 2008 was almost 30 quadrillion Btu and shows an increasing trend for the coming years. Therefore, the US economy has a huge dependence upon fuel exporting countries for price and supply stability [2].

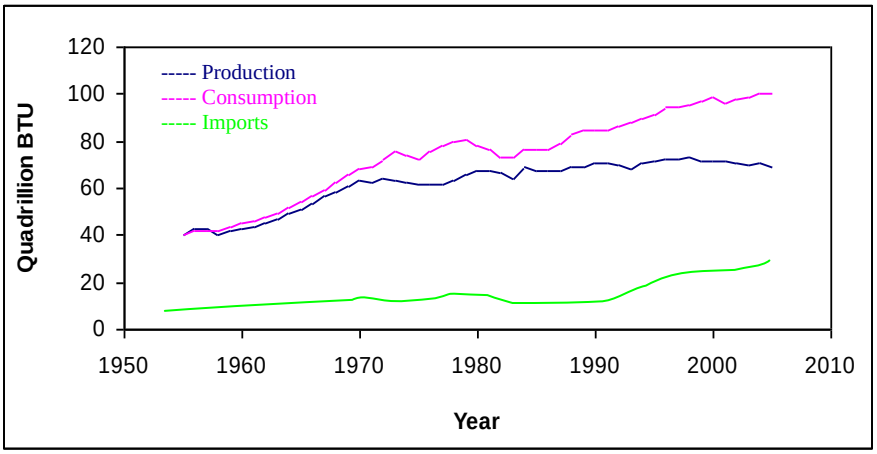

Figure 1. Monthly consumption, production, imports and exports in the US. [3]

Petroleum, coal and natural gas have been the major sources of energy in the US in the past (Figure 2). The high consumption and import of petroleum and the potential domestic reserves of coal have led the US Department of Energy (DOE) and the industrial sector to investigate new coal-based technologies to get clean energy more efficiently at lower capital cost [4]. Integrated Gasification Combined Cycle (IGCC) [5], advanced gas turbine [5] and coal-based zero emissions power plant [6] are some of the technological advances recently reported. It is important to note that these technologies are adaptable to natural gas feedstock. However, until clean coal technologies are well developed, production of natural gas must be sustained and increased to avoid dependence upon imported petroleum [2].

This dissertation follows the style of *Journal of Chemical Engineering Data*.

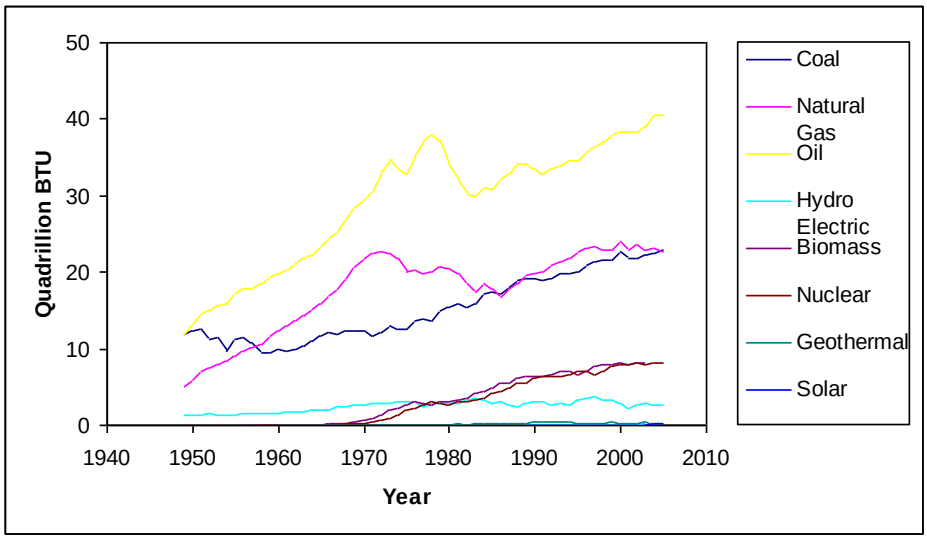

Figure 2. Consumption of energy from different sources US [3].

In addition to coal-based technologies, Gas to Liquids (GTL) technology has been developed. GTL technology involves converting natural gas into higher aliphatic hydrocarbons in the range of C_4-C_{10} [2], and it is more economical using natural gas feedstock than coal [7]. Recently, GTL plants have been commissioned in America, the Middle East, and Asia [8-11]. This information leads us to recognize that more understanding of liquid-gas mixtures is necessary to support technological developments that focus upon energy generation.

Natural gas exhibits reliable features as a clean, versatile and sustainable fuel. Figure 3 shows the flexibility of Natural Gas as an energy source when used in different demand sectors in the United States. As of December 31, 2007, the estimated total U.S proved reserves of dry natural gas were 237,726 Bcf [3]. Additionally; large volumes of natural gas classified as undiscovered recoverable resources exist [3]. Approximately 79% of deepwater reserves of oil and gas remain to be explored, as well as 20% of shallow-water reserves [12].

The conditions of deepwater reserves are in the pressure range of (89.6-124.1 MPa) and a temperature range of (365.6-408.15 K) [2]. At the production wellhead, the temperature range can be (283.49-293.8 K) and the pressure can be (10.3-20.7 MPa). These abrupt changes of pressure and temperature create operational problems such as

natural gas hydrate formation [13] and retrograde condensation [14]. A good base of data and an accurate EoS, validated in this range of operation, would help predict and avoid these inconveniences [2].

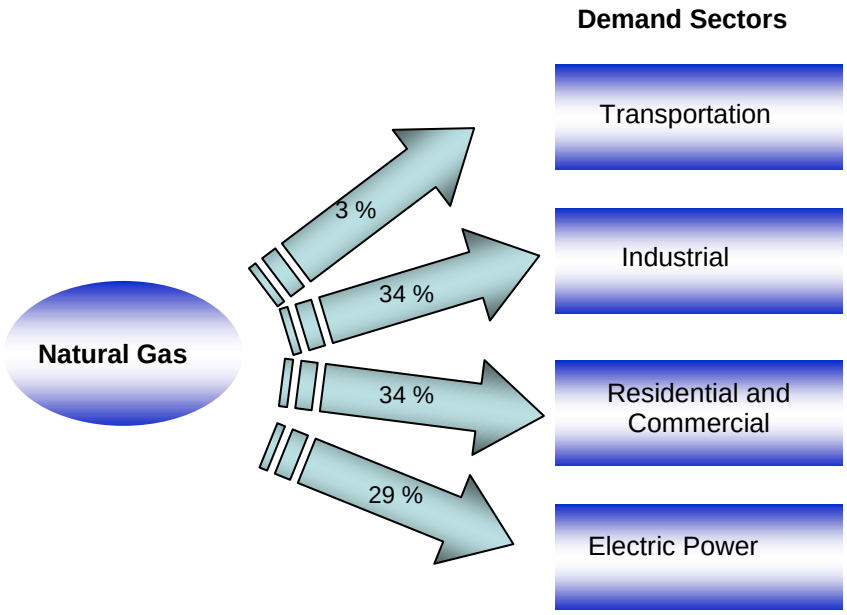

Figure 3. U.S. primary natural gas consumption by sector [3].

Although many years of research have emphasized determination of empirical and theoretical models for the prediction of equilibrium properties of natural gas, high uncertainty still exists in their determination [15]. This information is vital for design and operation of natural gas facilities and processes based upon natural gas as a feedstock. Figure 4 exemplifies the deviations of some EoS extensively used in the industry to predict phase envelopes for natural gas.

When natural gas undergoes custody transfer, the selling and buying process of the natural gas is quantified by measurements of mass flow rate using specific mass flow-meters such as orifice meters [2]. Equation 1 represents the methodology used for determining the Natural Gas price.

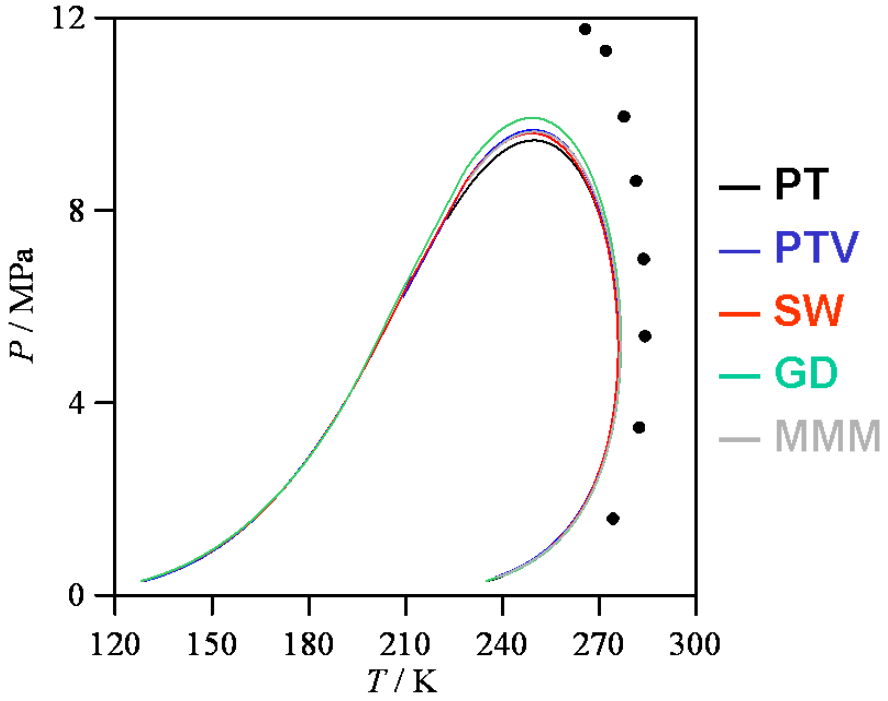

Figure 4. PT, PTV, SW, GD, MMM EoS predictions for synthetic natural gas mixture.

$$\frac{\$}{day} = \left(\frac{m^3}{day}\right)\left(\frac{kg}{m^3}\right)\left(\frac{J}{kg}\right)\left(\frac{\$}{J}\right) \qquad (1.\ 1.1)$$

The first factor on the right-hand side of the equation corresponds to the volumetric flow rate. Flow meters, such as orifice meters, determine this quantity. The second factor is the density. Table 1 demonstrates the effect of the accuracy of the density in the final profit or loss for either the selling or the buying companies during custody transfer. The third factor corresponds to the heating value of the gas, which results from either calorimetric measurements or composition analysis. The final term is the gas price determined by competition. Therefore, uncertainties in the mass flow measurements and equivalent energy values become relevant in the financial transactions between selling and buying companies. The use of an accurate and validated EoS in this process helps facilitate custody transfer and reduce errors in large volume trades.

Table 1. **Economic Impact of NG Custody Transfer** [3]

Accuracy	Density			Economic impact of inaccurate density measurements	
	Lower Boundary	True Value	Upper Boundary		
% Deviation	(kg/m^3)			($/year)	
0.03	0.9343	0.9346	0.9349	498,225	498,225
0.50	0.9299		0.9392	8,305,210	8,305,210
3.00	0.9065		0.9626	49,830,165	49,830,165
			Producer →	Loss	Profit
			Buyer →	Profit	Loss

1.2 Objectives of the Current Research

After the analysis of the economic importance of natural gas for society, evaluation of the actual situation of the natural gas industry, and lack of knowledge in academia about these systems, different challenges have driven in this research project. Two principal objectives of this project exist for contributing to the solution of the industrial and academic problems and improving understanding of natural gas mixtures:

1. To measure high-accuracy $P\rho T$ and equilibrium data over a wide range of pressures and temperatures for natural gas mixtures and its main constituents.
2. To contribute understanding of the molecular behavior for natural gas mixtures by using state of the art theoretical techniques.

These two principal objectives have secondary objectives:

1. To compensate the Force Transmission Error experienced during the operation of the High Pressure Single-Sinker Magnetic Suspension Densimeter (MSD) in order to minimize the uncertainty of density data collected with this apparatus.
2. To measure high-accuracy $P\rho T$ data for the main constituents of natural gas and natural gas mixtures up to very high pressure (200 MPa).
3. To develop a methodology that allows determination of phase equilibrium properties and isomolar derivatives for natural gas mixtures based upon isochoric data.
4. To design and build a new, high-pressure isochoric apparatus that allows determination of bubble points and expands the temperature and pressure range of the isochoric and $P\rho T$ high accuracy data for natural gas mixtures collected by the Thermodynamics Research group at Texas A&M University.
5. To propose an alternative methodology for determining natural gas composition that minimizes the uncertainty associated with long chain hydrocarbons present in the mixture.
6. To perform molecular mechanics and molecular dynamics calculations in order to develop a systematic and consistent data base that contributes to a better understanding of natural gas mixtures.
7. To incorporate the conformational effects into an analytical model that improves the prediction of mixtures with long chain hydrocarbons.

The enormous and complex task that involves the thermodynamics of natural gas mixtures makes conclusive results difficult in this research area. However, the new high-accuracy experimental data and scientific tools provide a path toward better understanding of these systems. The following sections present a detailed description of the experimental and theoretical activities and results obtained during the execution of this work.

EQUATIONS OF STATE FOR NATURAL GAS APPLICATIONS

2.1 State of the Art for EoS

A vast literature background exists in the EOS area [16]. Research in EoS includes experimental and theoretical activities, and both fields interact dynamically to improve their results. The experimental research includes collecting accurate thermodynamic data such as pressure, temperature, density, and thermal properties [17] and compositions for gas mixtures [2].

Numerous EoS have appeared in the past [16], and they have been able to attain good accuracy in the prediction of thermodynamic behavior of pure substances. Cubic, molecular-based and multiparametric EoS have performed well in the prediction of complex systems as well [16]. However, the problems of phase equilibrium and prediction of behavior at high pressures and temperatures for natural gas mixtures remain unresolved [18]. Heavy hydrocarbon effects in natural gas mixtures produce remarkable differences between the EoS predictions and experimental data [2, 18].

The cubic EoS present a balance between accuracy, reliability, simplicity and speed of computation [16]. However, they normally lack the necessary structure in some regions of phase space and produce inappropriate behavior for first and second derivatives. Still, industry uses the cubic EoS to predict phase equilibrium in multicomponent mixtures. The RK[19], SRK [20], PR [21] and PT [22] are examples of cubic EoS [23]. The quintic EoS [24] is a new attempt to develop an EOS with features similar to those of cubic EoS but with improved predictive capacity and flexibility. The quintic EoS is still in development phase and has not been extended to mixtures. The normal methods used to extend cubic EoS to mixtures have been classical, quadratic mixing rules, composition-dependent combining rules, density-dependent mixing rules and combining EoS with excess-Gibbs energy models [16].

In contrast to the cubic EoS, molecular-based EoS describe the thermophysical behavior of multicomponet systems. The major contribution of these EoS is to construct a real molecular understanding of thermodynamic behavior of fluids [25]. Beginning with Van der Waals theory and finishing with sophisticated statistics, molecular methods have produced a wide range of EoS. Perturbation theories, integral equation theories,

mechanical and dynamical molecular simulations and Monte Carlo methods have been used to build molecular-based EoS [16].

Inspired by the Van der Waals premise, which separates repulsive and attractive contributions to pressure, numerous authors [16] have developed theoretical approaches allowing generation of EoS that account for molecular interactions. Among these EoS, called generalized Van der Waals EoS, are: BACK (Boublic-Alder-Chen-Kresglewski,), PHCT (perturbed-hard-chain-theory), COR (chain of rotators), SAFT (statistical associated fluid theory) [25] and others [16]. Although the equations based upon the generalized Van der Waals theory can represent saturated data and PVT data outside the saturated region with few parameters, the complex functional forms of their universal parameters make them less desirable computationally than cubic EoS.

Multiparameter EoS are also an important family. The multiparameter EoS are based upon accurate experimental thermodynamic data[16]. The mathematical fitting of these experimental thermodynamic data using a mathematically arbitrary EoS produces remarkable agreement with experimental data. However, these EoS have a large number of parameters that affects computational time remarkably. The BWR (Benedict-Webb-Rubin), the Martin-Hou, and the Schimidt and Wagner are examples of multiparameter EoS [16]. Recently Kunz et al. [15] have developed a new reference equation of state for natural gas applications. This equation, GERG-2004, claims an accuracy of 0.1% in density determination of natural gas mixtures. Efforts at the National Institute of Standards and Technology (NIST) have developed a fluid property computer program named RefProp 8.0 [26] that includes a set of reference and technical EoS for a variety of fluids.

The virial EoS [27] is a valuable EoS because of its basis in statistical-mechanical theory. MGERG [28] and SGERG [29] are based upon the virial EoS. These EoS have been developed for pipeline custody transfer of natural gas. Iglesias-Silva and Hall (1996) extended the applicability range of SGERG. AGA8-DC92 [30], which is the current industry standard EoS for natural gas custody transfer, is an MBWR EoS because it involves virial terms as well as SGERG [2].

Theoretically, different alternatives have been developed to attack the EoS problem. The Van der Waals EoS has spawned multiple EoS [16]. The normal route used to solve the multicomponent themodynamic behavior has been to find an EoS with good prediction capability for pure components and to extend its scope using composition dependent mixing rules [31].

Recently, new developments in computational and statistical mechanics techniques have enabled development of a robust methodology to solve the complex molecular behavior of multicomponent systems[32-33]. This new window of knowledge allows one to continue theoretical research focusing upon the molecular based EoS and improving mixing rules in order to predict the thermodynamic behavior and to understand the driving forces that generate it.

In molecular dynamics and molecular mechanics simulations and the Monte Carlo technique, research has related to binary mixtures for hydrocarbons and associated compounds for natural gas components[34-36]. NERD, COMPASS, OPLS, AUA, UA have been the most used force fields. The predictability and reliability agree with experimental data. Nevauer et al. [34] employ Monte Carlo simulations using the NPT ensemble to determine the molar volume and compressibility factor of naturally occurring hydrocarbon mixtures. They had problems with calculations because of their pseudo-components representation of the real composition in the mixtures, the use of basic mixing rules for the Lennard-Jones potential parameters and the potential itself.

On the other hand, Boublík[37-38] has addressed the molecular-based BACK EOS improving the molecular representation of both the non-sphericity parameter (α) and the closed-packed volume (V^{00}). Starting from the old Scaled Particle Theory (SPT) developed by Reiss, Frisch, and Lebowitz [35] and its recent improvement [36], and modifying the respective values of α and V^{00} using enlarged, fused hard sphere models, they have obtained new numerical values for these parameters and some relative improvements in BACK EOS performance.

2.2 Multiparameter EoS

Recently, EoS based upon the Helmholtz energy functional have led to the most accurate reproductions of experimental data [39]. Despite the fact that the complex multiparameter functional used during their construction makes them computational expensive for process design and simulation, their unquestionable capability for reproducing high accuracy data makes them an indispensable tool for comparing standard quality data. This research project deals with high accuracy experimental data, therefore the understanding of these models is fundamental throughout this dissertation.

These EoS use the Helmholtz energy, a fundamental property function of density and temperature,

$$a(\rho,T) = a^0(\rho,T) + a^r(\rho,T) \tag{2.2.1}$$

where $a(\rho,T)$ is the Helmholtz energy, $a^0(\rho,T)$ is the ideal gas contribution to the Helmholtz energy, and $a^r(\rho,T)$ is the residual Helmholtz energy. Usually this formulation is represented better as dimensionless Helmholtz energy functions and dimensionless density and temperature:

$$\frac{a(\rho,T)}{RT} = \alpha(\delta,\tau) = \alpha^0(\delta,\tau) + \alpha^r(\delta,\tau) \tag{2.2.2}$$

where $\delta = \rho/\rho_c$ and $\tau = T_c/T$. A major advantages of this formulation is that any thermodynamic property can be determined from derivatives of the Helmholtz energy

$$Z(\delta,\tau,\bar{x}) = 1 + \delta\alpha^r_\delta \tag{2.2.3}$$

where $\alpha^r_\delta = \left(\partial\alpha^r / \partial\delta\right)_{\tau,\bar{x}}$ is the first derivative of the residual Helmholtz energy with respect to the residual density. The ideal gas Helmholtz energy in dimensionless form is

$$\alpha^0 = \ln\delta - \ln\tau + \sum a_k \tau^{i_k} + \sum a_k \ln\left[1 - \exp\left(-b_k\tau\right)\right] \tag{2.2.4}$$

where $\delta_0 = \rho_0 / \rho_c$ and $\tau_0 = T_c / T_0$.

The usual functional form for Helmholtz energy EoS is

$$\alpha^r(\delta,\tau) = \sum N_k \delta^{d_k} \tau^{t_k} + \sum N_k \delta^{d_k} \tau^{t_k} \exp\left(-\delta^{l_k}\right) \tag{2.2.5}$$

but some equations of state [39] use additional, Gaussian bell-shaped terms, first proposed by Setzmann and Wagner [40], for the methane EoS

$$\begin{aligned} \alpha^r(\delta,\tau) = & \sum N_k \delta^{d_k} \tau^{t_k} + \sum N_k \delta^{d_k} \tau^{t_k} \exp\left(-\delta^{l_k}\right) \\ & + \sum N_k \delta^{d_k} \tau^{t_k} \exp\left(-\eta\left(\delta-\varepsilon_k\right)^2 - \beta\left(\tau-\gamma_k\right)^2\right) \end{aligned} \tag{2.2.6}$$

Each summation typically has 4 to 20 terms.

Lemmon et al. have recently developed a robust methodology to construct multiparameter EoS incorporating the previous contributions of different authors [30, 41-42]. This methodology does not focus specifically upon the quantitative statistical analysis of the fitting procedure, but rather upon the quality and the physical sense of the model by analyzing different thermodynamic scenarios. The combination of accurate reproduction of experimental data and fulfillment of all the available thermodynamic constrains leads to the best, high-quality EoS developed so far.

As an example, two comparisons have appeared between the fundamental EoS for propane [39] and a new EoS for propylene glycol that is still under development by Cristancho et al. [43]. Figures 4 and 5 come from the RefProp 8.0 program. Figure 5 reveals that both equations represent the temperature-density diagram correctly. However a closer inspection of these plots reveals that the rectilinear diameter for the propylene glycol equation of state has a smooth curvature, in contrast to the perfectly rectilinear diameter displayed by the propane equation of state, which is the correct behavior.

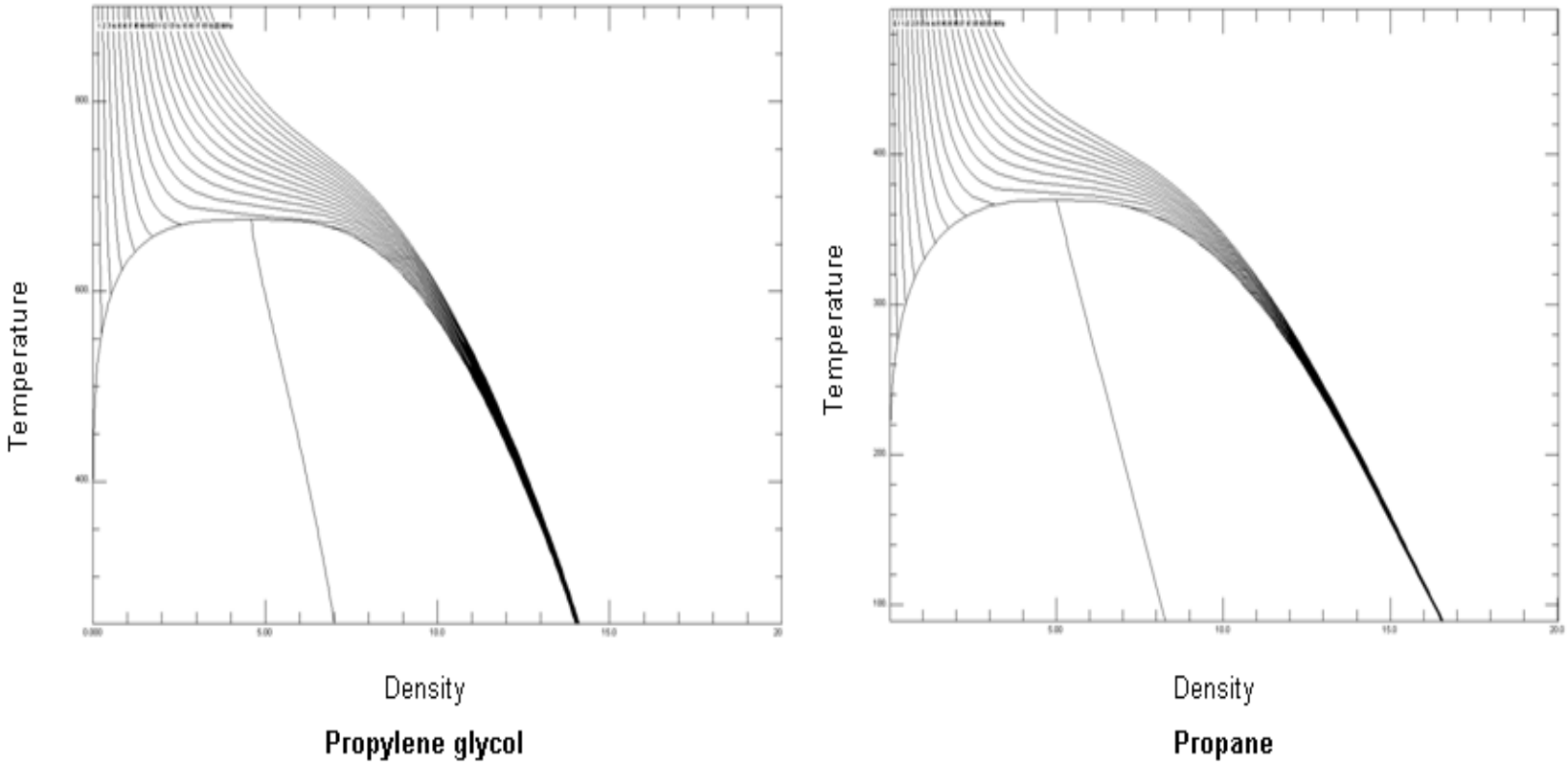

Figure 5. Temperature-density diagram for the propylene glycol EoS and propane EoS.

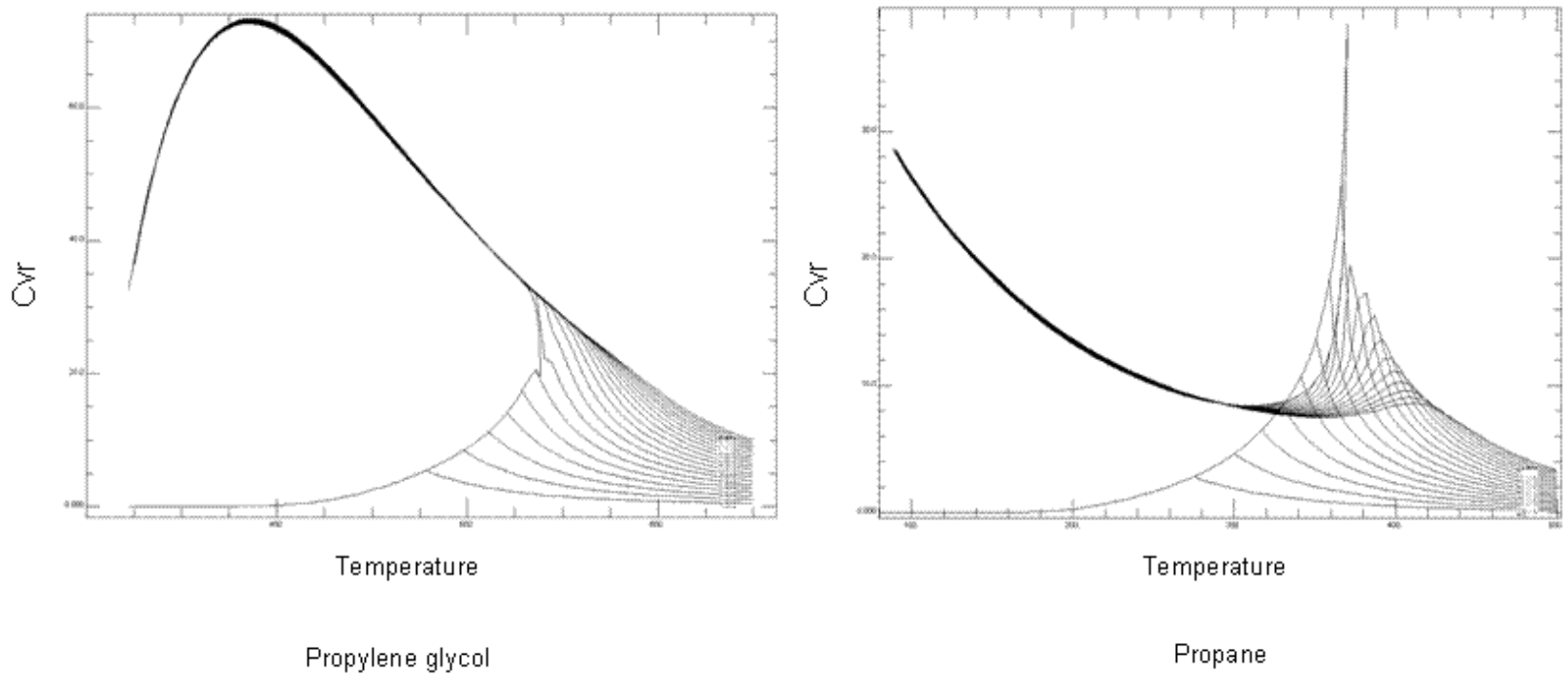

Figure 6. Cvr-Temperature diagram for propylene glycol EoS and propane EoS.

Figure 6 indicates that the propylene glycol EoS does not predict correct behavior for the residual heat capacity at constant volume $Cvr = (Cv - Cp)/RT$. The propane EoS represents correct behavior. In conclusion, many different scenarios should be analyzed to develop an outstanding multiparameter equation of state.

2.2.1 GERG-2004

GERG-2004 is a multiparameter EoS adopted by GERG (Groupe Europeen de Recherches Gazieres) in 2004. GERG-2004 is based upon a multi-fluid approximation explicit in the reduced Helmholtz energy

$$\alpha\left(\delta,\tau,\bar{x}\right) = \alpha^{0}\left(\rho,T,\bar{x}\right) + \alpha^{r}\left(\delta,\tau,\bar{x}\right) \tag{2.2.1.1}$$

where $\alpha^{0}\left(\rho,T,\bar{x}\right)$ accounts for the ideal Helmholtz energy part of the mixture

$$\alpha^{0}\left(\rho,T,\bar{x}\right) = \sum_{i=1}^{N} x_i \left[\alpha_{0i}^{0}\left(\rho,T\right) + \ln x_i\right] \tag{2.2.1.2}$$

and $\alpha^{r}\left(\delta,\tau,\bar{x}\right)$ is the residual Helmholtz energy of the mixture

$$\alpha^{r}\left(\delta,\tau,\bar{x}\right) = \sum_{i=1}^{N} x_i \alpha_{0i}^{r}\left(\delta,\tau\right) + \sum_{i=1}^{N-1}\sum_{j=i+1}^{N} x_i x_j F_{ij} \alpha_{ij}^{r}\left(\delta,\tau\right) \tag{2.2.1.3}$$

$\delta = \rho / \rho_r\left(\bar{x}\right)$ is the reduced density of the mixture and $\tau = T_r\left(\bar{x}\right)/T$ is the residual temperature of the mixture. A more detailed description of the mathematical structure of this equation appears in the GERG TM 15 2007 by Kunz et al. [15]. The optimized methodology utilized in the GERG-2004 EoS structure allows determining all thermodynamic functions just with direct derivatives of the reduced Helmholtz energy as follows for pressure

$$\frac{p\left(\delta,\tau,\bar{x}\right)}{\rho RT}=1+\delta\alpha_{\delta}^{r} \qquad (2.2.1.4)$$

where $\alpha_{\delta}^{r}=\left(\partial\alpha^{r}/\partial\delta\right)_{\tau,\bar{x}}$ is the first derivative of the residual Helmholtz energy with respect to the residual density. This peculiarity avoids integral calculations that can be difficult for the numerical performance of this EoS in process simulators. The most remarkable characteristic of this EoS is its high-accuracy predictions for thermodynamic properties in the homogeneous gas, liquid and supercritical regions as well as vapor-liquid equilibrium states. The data base used to develop GERG-2004 contains more than 100,000 experimental data for volumetric and thermal properties of binary mixtures, natural gas mixtures and other types of mixtures. This robust experimental support makes GERG-2004 a reference EoS for application in industrial process design to make more accurate calculations and to minimize the over- and under-design of industrial units.

Table 2. Estimated Relative Experimental Uncertainties of the Most Accurate Binary and Multicomponent Mixture Data [15]

Data Type	Property	Relative Uncertainty
$P\rho T$ data	$\Delta\rho/\rho$	≤ (0.05-0.1)%
Isochoric heat capacity	$\Delta c_v/c_v$	≤ (1-2)%
Speed of sound (gas phase)	$\Delta w/w$	≤ (0.05-0.1)%
Isobaric heat capacity	$\Delta c_p/c_p$	≤ (1-2)%
Enthalpy differences	$\Delta(\Delta h)/\Delta h$	≤ (0.2-0.5)%
Saturated liquid density	$\Delta\rho'/\rho'$	≤ (0.1-0.2)%
VLE data	$\Delta p_s/p_s$	≤ (1-3)%

The estimated relative uncertainties for the most accurate binary and multicomponent mixtures appear in the Table 2 [15]. These values support the outstanding reliability of this equation to predict thermodynamic properties for natural gas mixtures.

However, this EoS requires more computational time when used in process design and optimization. Within this work, GERG-2004 provides is the reference values for all comparisons to experimental data.

2.3 The Quintic Equation of State

Since the work of Hall and Atilhan [24] in which they propose a quintic EoS, additional improvements have been developed for this idea. The hypothesis behind this approach is to find a new quintic functional form that achieves accurate prediction like multiparameter equations but with a small number of parameters. This can lead to more efficient computing algorithms useful for process design and simulation. The generalized quintic form is:

$$Z = \frac{1 + n_1\rho + n_2\rho^2 + n_3\rho^3 + n_4\rho^4}{1 + d_1\rho + d_2\rho^2 + d_3\rho^3} \tag{2.3.1}$$

where Z is the compressibility factor, ρ is the density and the n_i and d_i are temperature dependent parameters. One of the principal challenges with this equation has been the unique determination of the set $\{n_i, d_i\}$. The non-linearity of the quintic equation leads to multiples solutions, most of them inconsistent with physical constraints. Therefore, Cristancho et al. [44] start a systematic approach seeking the most reliable and consistent functional in order to include thermodynamic constraints in the quintic form using the minimum number of parameters.

To simplify inclusion of additional thermodynamic constraints such as the phase equilibrium constraints, the original form of the quintic equation is transformed into a Helmholtz energy function. Starting with factorizing the denominator

$$Z = \frac{1 + n_1\rho + n_2\rho^2 + n_3\rho^3 + n_4\rho^4}{(1 + b\rho)(1 + D_1\rho + D_2\rho^2)} \tag{2.3.2}$$

where

$$D_1 = d_1 + b$$
$$D_2 = d_2 + bd_1 + b^2 = -d_3/b$$
$$d_3 + bd_2 + b^2 d_1 + b^3 = 0$$

Then,

$$\frac{Z-1}{\rho} = \frac{N_1 + N_2\rho + N_3\rho^2 + N_4\rho^3}{(1+b\rho)(1+D_1\rho + D_2\rho^2)} \tag{2.3.3}$$

where

$$N_1 = n_1 - d_1$$
$$N_2 = n_2 - d_2$$
$$N_3 = n_3 - d_3$$
$$N_4 = n_4$$

The residual Helmholtz Free Energy comes from

$$\frac{A^r}{RT} = \int_0^\rho \frac{Z-1}{\rho} d\rho \tag{2.3.4}$$

and

$$\frac{Z-1}{\rho} = \frac{F_1(\rho)}{1-b\rho} + \frac{F_2(\rho)}{1+D_1\rho + D_2\rho^2} \tag{2.3.5}$$

where $F_1(\rho)$ and $F_2(\rho)$ can take different combinations as represented in Table 3. After performing all the multiple possibilities in the determination of the Helmholtz energy, different cases result.

Table 3. Mathematical Combinations for Functions $F_1(\rho)$ and $F_2(\rho)$

$F_1(\rho)$	$F_2(\rho)$
N_1	$a_1\rho + a_2\rho^2$ or $a_2\rho^2$
$N_1 + N_2\rho$	$a_1\rho + a_2\rho^2$ or $a_1\rho$ or $a_2\rho^2$
$N_2\rho$	N_1 or $N_1 + a_1\rho + a_2\rho^2$ or $N_1 + a_2\rho^2$

Case I.

(a) $F_1(\rho) = N_1$ and $F_2(\rho) = a_1\rho + a_2\rho^2$

$$\frac{A^r}{RT} = -\frac{N_1}{b}\ln\left(1-b\rho\right) + \frac{a_2}{D_2}\rho + \frac{\left(a_1D_2 - a_2D_1\right)}{2D_2^2}\ln\left(1 + D_1\rho + D_2\rho^2\right) + \ldots$$
$$\frac{1}{2}\left\{\frac{D_1a_2D_2 + 2D_2a_2 - D_1^2a_2}{D_2^2\sqrt{D_1^2 - 4D_2}}\right\}\ln\left(\frac{1 + \dfrac{2D_2\rho}{\sqrt{D_1^2 - 4D_2} + 1}}{1 - \dfrac{2D_2\rho}{\sqrt{D_1^2 - 4D_2} - 1}}\right) \qquad (2.3.6)$$

(b) $F_1(\rho) = N_1$ and $F_2(\rho) = a_2\rho^2$

$$\frac{A^r}{RT} = -\frac{N_1}{b}\ln\left(1-b\rho\right) + \frac{a_2}{D_2}\rho - \frac{a_2D_1}{2D_2^2}\ln\left(1 + D_1\rho + D_2\rho^2\right) + \ldots$$
$$\frac{a_2}{2}\left\{\frac{2D_2^2 - D_1^2}{D_2^2\sqrt{D_1^2 - 4D_2}}\right\}\ln\left(\frac{1 + \dfrac{2D_2\rho}{\sqrt{D_1^2 - 4D_2} + 1}}{1 - \dfrac{2D_2\rho}{\sqrt{D_1^2 - 4D_2} - 1}}\right) \qquad (2.3.7)$$

Case II.

a) $F_1(\rho) = N_1 + N_2\rho$ and $F_2(\rho) = a_1\rho + a_2\rho^2$

$$\frac{A^r}{RT} = -\left\{\frac{N_1}{b} + \frac{N_2}{b^2}\right\}\ln\left(1-b\rho\right) + \left\{\frac{a_2}{D_2} + \frac{N_2}{b}\right\}\rho + \frac{\left(a_1D_2 - a_2D_1\right)}{2D_2^2}\ln\left(1 + D_1\rho + D_2\rho^2\right) + \ldots$$
$$\frac{1}{2}\left\{\frac{D_1\left(a_1D_2 - a_2D_1\right) + 2D_2a_2}{D_2^2\sqrt{D_1^2 - 4D_2}}\right\}\ln\left(\frac{1 + \dfrac{2D_2\rho}{\sqrt{D_1^2 - 4D_2} + 1}}{1 - \dfrac{2D_2\rho}{\sqrt{D_1^2 - 4D_2} - 1}}\right) \qquad (2.3.8)$$

b) $F_1(\rho) = N_1 + N_2\rho$ and $F_2(\rho) = a_1\rho$

$$\frac{A^r}{RT} = -\left\{\frac{N_1}{b} + \frac{N_2}{b^2}\right\}\ln\left(1-b\rho\right) + \frac{a_2}{D_2}\rho + \frac{a_1}{2D_2}\ln\left(1 + D_1\rho + D_2\rho^2\right) + \ldots$$
$$\frac{1}{2}\left\{\frac{D_1a_1}{D_2^2\sqrt{D_1^2 - 4D_2}}\right\}\ln\left(\frac{1 + \dfrac{2D_2\rho}{\sqrt{D_1^2 - 4D_2} + 1}}{1 - \dfrac{2D_2\rho}{\sqrt{D_1^2 - 4D_2} - 1}}\right) \qquad (2.3.9)$$

c) $F_1(\rho) = N_1 + N_2\rho$ and $F_2(\rho) = a_2\rho^2$

$$\frac{A^r}{RT} = -\left\{\frac{N_1}{b} + \frac{N_2}{b^2}\right\}\ln\left(1-b\rho\right) + \frac{a_2}{D_2}\rho + \frac{a_1}{2D_2}\ln\left(1 + D_1\rho + D_2\rho^2\right) + \ldots$$
$$\frac{1}{2}\left\{\frac{a_2\left(2D_2 - D_1^2\right)}{D_2^2\sqrt{D_1^2 - 4D_2}}\right\}\ln\left(\frac{1 + \dfrac{2D_2\rho}{\sqrt{D_1^2 - 4D_2} + 1}}{1 - \dfrac{2D_2\rho}{\sqrt{D_1^2 - 4D_2} - 1}}\right) \qquad (2.3.10)$$

Case III

a) $F_1(\rho) = N_2\rho$ and $F_2(\rho) = N_1$

$$\frac{A^r}{RT} = -\frac{N_2}{b^2}\ln\left(1-b\rho\right) + \frac{N_2}{b}\rho - \frac{N_1}{\sqrt{D_1^2 - 4D_2}}\ln\left(\frac{1 + \dfrac{2D_2\rho}{\sqrt{D_1^2 - 4D_2} + 1}}{1 - \dfrac{2D_2\rho}{\sqrt{D_1^2 - 4D_2} - 1}}\right) \qquad (2.3.11)$$

b) $F_1(\rho) = N_2\rho$ and $F_2(\rho) = N_1 + a_1\rho + a_2\rho^2$

$$\frac{A^r}{RT} = -\frac{N_2}{b^2}\ln\left(1-b\rho\right) + \left\{\frac{a_2}{D_2} + \frac{N_2}{b}\right\}\rho + \frac{\left(a_1D_2 - a_2D_1\right)}{2D_2^2}\ln\left(1 + D_1\rho + D_2\rho^2\right) + \ldots$$
$$\frac{1}{2}\left\{\frac{D_1\left(a_1D_2 - a_2D_1\right) + 2D_2a_2 - 2N_1D_2^2}{D_2^2\sqrt{D_1^2 - 4D_2}}\right\}\ln\left(\frac{1 + \dfrac{2D_2\rho}{\sqrt{D_1^2 - 4D_2} + 1}}{1 - \dfrac{2D_2\rho}{\sqrt{D_1^2 - 4D_2} - 1}}\right) \qquad (2.3.12)$$

c) $F_1(\rho) = N_2\rho$ and $F_2(\rho) = N_1 + a_2\rho^2$

$$\frac{A^r}{RT} = -\frac{N_2}{b^2}\ln\left(1-b\rho\right) + \left\{\frac{a_2}{D_2} + \frac{N_2}{b}\right\}\rho - \frac{a_2D_1}{2D_2^2}\ln\left(1 + D_1\rho + D_2\rho^2\right) + \ldots$$
$$\frac{1}{2}\left\{\frac{2D_2a_2 - a_2D_1^2 - 2N_1D_2^2}{D_2^2\sqrt{D_1^2 - 4D_2}}\right\}\ln\left(\frac{1 + \dfrac{2D_2\rho}{\sqrt{D_1^2 - 4D_2} + 1}}{1 - \dfrac{2D_2\rho}{\sqrt{D_1^2 - 4D_2} - 1}}\right) \qquad (2.3.13)$$

Each of these cases represents a possible way to define the quintic equation as a Helmholtz energy function. Initial work has focused upon determining the correct number of parameters to include in the quintic form and their corresponding functionalities with temperature [44].

An alternative procedure is to correlate this quintic functional based upon the multiparameter fitter developed by Lemmon et al. [26]. Basically a new functional form for the Helmholtz energy is defined based upon the different cases obtained earlier from the Helmholtz integral. Now, the Helmholtz energy function and the density are dimensionless:

$$\alpha^r(\delta,\tau) = \frac{A^r}{RT} = \int_0^\rho \frac{Z-1}{\delta}d\delta \qquad (2.3.14)$$

where $\alpha^r(\delta,\tau)$ is the dimensionless residual Helmholtz free energy, $\delta = \rho/\rho_c$ and $\tau = T_c/T$. When

$$\frac{Z-1}{\delta} = \frac{F_1(\delta)}{1-b\delta} + \frac{F_2(\delta)}{1+D_1\delta+D_2\delta^2} \tag{2.3.15}$$

and taking $F_1(\delta) = S_2\delta$ and $F_2(\delta) = N_1$, and $S_2 = N_4 / D_2$

$$\alpha^r(\delta,\tau) = \frac{A^r}{RT} = -\frac{S_2}{b^2}\ln\left(1-b\delta\right) + \frac{S_2}{b}\delta - \frac{N_1}{\sqrt{D_1^2-4D_2}}\ln\left(\frac{1+\dfrac{2D_2\delta}{\sqrt{D_1^2-4D_2}+1}}{1-\dfrac{2D_2\delta}{\sqrt{D_1^2-4D_2}-1}}\right) \tag{2.3.16}$$

This functional form leads to a simpler functional:

$$\alpha^r(\delta,\tau) = \eta(\tau)\left[\delta - \frac{\ln(1-b(\tau)\delta)}{b(\tau)}\right] - \varepsilon(\tau)\ln\left(\frac{1+\gamma(\tau)\delta}{1-\beta(\tau)\delta}\right) \tag{2.3.17}$$

where

$$\eta = S_2 / b$$
$$\varepsilon = N_1 / \sqrt{D_1^2-4D_2}$$
$$\gamma = \frac{2D_2}{\sqrt{D_1^2-4D_2}+1}$$
$$\beta = \frac{2D_2}{\sqrt{D_1^2-4D_2}-1}$$

Now in order to take advantage of the multiparamer fitter developed by Lemmon et al.[26] the first and second derivatives have to be calculated. The results are

$$\alpha^r_\delta(\delta,\tau) = \eta\left\{1+\frac{1}{(1-b\delta)}\right\} - \varepsilon\left\{\frac{\gamma}{1+\gamma\delta}+\frac{\beta}{1-\beta\delta}\right\} \tag{2.3.18}$$

$$\alpha^r_{\delta\delta}(\delta,\tau) = \frac{\eta b}{(1-b\delta)^2} + \varepsilon\left\{\frac{\gamma^2}{(1+\gamma\delta)^2} - \frac{\beta^2}{(1-\beta\delta)^2}\right\} \tag{2.3.19}$$

$$\alpha^r_{\delta\delta\delta}(\delta,\tau) = 2\frac{\eta b^2}{(1-b\delta)^3} - 2\varepsilon\left\{\frac{\gamma^3}{(1+\gamma\delta)^3} + \frac{\beta^3}{(1-\beta\delta)^3}\right\} \tag{2.3.20}$$

$$\begin{aligned}\alpha^r_{\tau} = \eta_\tau\left\{\delta - \frac{\ln(1-b\delta)}{b}\right\} + \frac{\eta b_\tau}{b}\left\{\frac{\ln(1-b\delta)}{b} + \frac{\delta}{(1-b\delta)}\right\} + \ldots \\ -\varepsilon_\tau \ln\left(\frac{1+\gamma\delta}{1-\beta\delta}\right) - \varepsilon\delta\left\{\frac{\gamma_\tau}{1+\gamma\delta} + \frac{\beta_\tau}{1-\beta\delta}\right\}\end{aligned} \tag{2.3.21}$$

$$\begin{aligned}\alpha^r_{\tau\tau} = \eta_{\tau\tau}\left\{\delta - \frac{\ln(1-b\delta)}{b}\right\} + \frac{1}{b}\left[2\eta_\tau b_\tau + \eta b_{\tau\tau} - \frac{\eta b_\tau^2}{b}\right]\left\{\frac{\ln(1-b\delta)}{b} + \frac{\delta}{(1-b\delta)}\right\} + .. \\ + \frac{\eta b_\tau^2}{b^2}\left\{\frac{\delta(2b\delta-1)}{(1-b\delta)^2} - \frac{\ln(1-b\delta)}{b}\right\} - \varepsilon_{\tau\tau}\ln\left(\frac{1+\gamma\delta}{1-\beta\delta}\right) - 2\varepsilon_\tau\delta\left\{\frac{\gamma_\tau}{1+\gamma\delta} - \frac{\beta_\tau}{1-\beta\delta}\right\} + .. \\ -\varepsilon\delta\left\{\frac{\gamma_{\tau\tau}}{1+\gamma\delta} + \frac{\beta_{\tau\tau}}{1-\beta\delta} - \delta\left(\frac{\gamma_\tau^2}{(1+\gamma\delta)^2} - \frac{\beta_\tau^2}{(1-\beta\delta)^2}\right)\right\}\end{aligned} \tag{2.3.22}$$

$$\begin{aligned}\alpha^r_{\delta\tau}(\delta,\tau) = \eta_\tau\left\{1 + \frac{1}{(1-b\delta)}\right\} + \frac{\eta b_\tau\delta}{(1-b\delta)^2} - \varepsilon_\tau\left\{\frac{\gamma}{1+\gamma\delta} + \frac{\beta}{1-\beta\delta}\right\} + \ldots \\ -\varepsilon\left\{\frac{\gamma_\tau}{1+\gamma\delta} + \frac{\beta_\tau}{1-\beta\delta} - \delta\left(\frac{\gamma\gamma_\tau}{(1+\gamma\delta)^2} - \frac{\beta\beta_\tau}{(1-\beta\delta)^2}\right)\right\}\end{aligned} \tag{2.3.23}$$

where $A_x = A(x,y)_x = (\partial A/\partial x)_y$. This equation is being initially fit to methane data and with simple temperature functions for $\eta(T)$, $\varepsilon(T)$, $\gamma(T)$ and $\beta(T)$.

The quintic EoS is an important approach that promises excellent performance. However, more work has to be done until a final conclusion can be drawn for this new functional.

EXPERIMENTAL CHARACTERIZATION OF NATURAL GAS MIXTURES*

It is well known that any thermodynamics property of a fluid can be determined from a set of volumetric, composition and saturation data [45]. With the former information over a wide range of thermodynamics states, a thermodynamic formulation results for a fluid. Obviously the quantitative quality of the predictions based upon any type of thermodynamics formulation relies upon the accuracy of the data used during the fitting process.

One of the main challenges of this research project has been to establish accurately a robust set of thermodynamic volumetric, composition and saturation data for natural gas, its main constituents and associated mixtures. Achieving this goal has required a detailed uncertainty analysis of the recent techniques developed in the Thermodynamics Research Group at Texas A&M [2, 17, 46-47]. Additional improvements for these techniques and a new high pressure isochoric apparatus have been developed. Finally a new technique for minimizing the uncertainty of the gas composition has been proposed and tested. The next sections contain descriptions and analysis of each data collection technique.

3.1 $P\rho T$ Data

Magnetic suspension densimeters have provided high accuracy $P\rho T$ data for different substances over wide ranges of temperature and pressure for three decades [48-49]. Wagner and Kleinrahm [50] discuss the advantages of this technique and contrast it to with

---

* Part of this chapter is reprinted with permission from "Force Transmission Error Analysis for a High-Pressure Single-Sinker Magnetic Suspension Densimeter" by Diego E. Cristancho, Ivan D. Mantilla, Saquib Ejaz, Kenneth R. Hall, Gustavo A. Iglesias-Silva and Mert Atilhan, 2010. *International Journal of Thermophysics*, DOI: 10.1007/s10765-010-0702-3 , Copyright 2010 by Springer Netherlands.

Part of this chapter is reprinted with permission from "Method and uncertainties to determine phase boundaries from isochoric" by Pedro L. Acosta-Perez, Diego E. Cristancho, Ivan D. Mantilla, Kenneth R. Hall and Gustavo A. Iglesias-Silva, 2009. *Fluid Phase Equilibria*, volume 283, pages 17-21, Copyright 2009 by Elsevier B.V.

Part of this chapter is reprinted with permission from "Accurate PρT Data for Methane from (300 to 450) K up to 180 MPa" by Diego E. Cristancho, Ivan D. Mantilla, Saquib Ejaz, Kenneth R. Hall, Mert Atilhan and Gustavo A. Iglesias-Silva, 2009. *Journal of Chemical Engineering Data*, DOI: 10.1021/je9004849, Copyright 2009 by American Chemical Society.

Part of this chapter is reprinted with permission from "Accurate PρT Data for Ethane from (298 to 450) K up to 200 MPa" by Diego E. Cristancho, Ivan D. Mantilla, Saquib Ejaz, Kenneth R. Hall, Mert Atilhan and Gustavo A. Iglesias-Silva, 2010. *Journal of Chemical Engineering Data*, DOI: 10.1021/je900978x, Copyright 2010 by American Chemical Society.

other techniques. The thermodynamics research group at Texas A&M University has utilized a unique, high-accuracy, high-pressure, single-sinker magnetic suspension densimeter, Figure 7. The main characteristics of this apparatus appear in the ref 2 with recent modifications in refs 46 and 47. Additionally, this research project implemented several improvements to the magnetic suspension densimeter. First, speeding the heating cycle minimized the heating time during high temperature measurements; second, technical analysis of the isothermal shields indicated that the external isothermal shield was not necessary to achieve the desired temperature stability, and, finally, anchoring the high-precision electronic balance to the aluminum platform avoided displacement of the electromagnet and minimized uncertainty in the measurements caused by vertical and horizontal alignment.

Figure 7. High pressure single-sinker magnetic suspension densimeter.

The capability of going to high pressure (200 MPa) in the single-sinker magnetic suspension densimeter allows determination of high-accuracy density data covering a wider range than any other MSD. Although preliminary analysis of the uncertainty for $P\rho T$ data measured using this apparatus have appeared [46-47], none have accounted properly for one of the main source of uncertainty for this apparatus, the force transmission error (FTE). Therefore, an important task for this research project was the accurate determination of the FTE.

3.1.1 Force Transmission Error Analysis

An MSD utilizes the Archimedes principle, and consists of a pressurized cell with an internal sinker that senses a buoyancy force when the cell contains a fluid. A magnetic suspension coupling system transmits the change its apparent weight to a high-precision mass balance without direct connection between the sample cell and the balance. Knowledge of the apparent weight of the sinker and its properties allows determination of accurate densities for the fluid.

The FTE is a significant source of uncertainty in this technique. FTE is the error caused by the magnetic behavior of the cell, the suspension coupling and the measured fluid that leads to inaccuracies in the transmitted force measured at the high-precision balance. Different approaches exist to estimate and compensate for the FTE [51-52]. Kano et al. [52] have proposed an analysis based upon a magnetostatic study of the MSD suspension. This analysis accounts for all the magnetic, gravitational and buoyancy forces during the measuring process. Unfortunately, this approach requires a detailed knowledge of both the magnetic and geometric properties of the MSD and the fluid, which are not always available. McLinden et al. [51] have developed an empirical analysis applicable to both two- and single-sinker magnetic densimeters. In their analysis, they attribute the FTE to two different sources, one is the magnetic error introduce by the MSD, the *"apparatus effect"*, which accounts for error caused by the magnetic characteristics of the densimeter cell and the suspension coupling. In principle, the apparatus effect is available from vacuum measurements of the sinker mass. The other source of error depends upon the magnetic properties of the fluid, the *"fluid-specific effect".*

McLinden et al. [51] present a detailed explanation of each of the different sources of error and a mathematical model for its determination. The mathematical model results from a force balance during the different measurements steps in the MSD. For a single-sinker MSD, they suggest performing experiments using two different sinkers to determine unknowns in the mathematical model. They applied their technique to the single-sinker densimeter developed by Brachthäuser et al. [53]. The results show different values for the apparatus effect for each type of densimeter, and they conclude that "the

apparatus effect must be determined for each densimeter." An additional important result in their analysis is that "with careful measurements and the necessary calibrations, a single-sinker densimeter can yield PρT data nearly as accurate as those from a two-sinker densimeter" presuming the two-sinker densimeter data are correct.

Rubotherm Präzisionsmesstechnik GmbH manufactured our single-sinker MSD, specially designed to work at pressures up to 200 MPa over a temperature range of 193-523 K. This apparatus has been used to measure densities of natural gas and associated mixtures as well as for low- and high-pressure densities for pure components[2, 46-47]. The FTE analysis for this apparatus follows both the analysis and the results of McLinden et al. [51]. It was not possible to implement exactly the same procedure because of the peculiarities of our MSD (thicker cell wall and a higher apparatus contribution to the FTE) reflected in the scatter of the apparatus constant determined from the McLinden et al. [51] approach, Figure 8. The apparatus constant results display an average value of 55.5 ± 211.5 ppm which cannot be considered as a statistically significant value. This result dictates a slightly different approach to quantify and compensate for of this source of error.

3.1.1.1 Theoretical Model

Figure 9 presents the operation of the single-sinker MSD. In the (a) position, the balance is tared; in the (b) position, the permanent magnet (pm) is weighted; and in the (c) position, the permanent magnet and the sinker are weighted. In all positions, the electromagnet (em) is weighted.

The forces on the balance are

$$w_1 = \alpha \left\{ \phi \left[m_{\mathrm{pm}} - \rho_{\mathrm{f}} V_{\mathrm{pm}} \right] + m_{\mathrm{em}} + m_{\mathrm{c1}} - \rho_{\mathrm{a}} \left(V_{\mathrm{em}} + V_{\mathrm{c1}} \right) + w_{\mathrm{zero}} \right\} \qquad (3.1.1.1.1)$$

$$w_2 = \alpha \left\{ \phi \left[m_{\mathrm{s}} + m_{\mathrm{pm}} - \rho_{\mathrm{f}} \left(V_{\mathrm{s}} + V_{\mathrm{pm}} \right) \right] + m_{\mathrm{em}} + m_{\mathrm{c2}} - \rho_{\mathrm{a}} \left(V_{\mathrm{em}} + V_{\mathrm{c2}} \right) + w_{\mathrm{zero}} \right\} \qquad (3.1.1.1.2)$$

$$w_2 - w_1 = \alpha \left\{ \phi \left[m_{\mathrm{s}} - \rho_{\mathrm{f}} V_{\mathrm{s}} \right] + m_{\mathrm{c2}} - m_{\mathrm{c1}} - \rho_{\mathrm{a}} \left(V_{\mathrm{c1}} - V_{\mathrm{c2}} \right) \right\} \qquad (3.1.1.1.3)$$

where α is the balance calibration factor, ϕ is the coupling factor, ρ_f is the fluid density, ρ_a is the density of the purge gas in the balance chamber (nitrogen), V is the total volume, m is the mass, w is the balance reading, and w_{zero} is the balance reading with nothing on the balance pan or weighing hook. The subscripts are: 1 denotes balance position 1, pm denotes the permanent magnet and includes the lifting fork, em denotes the electromagnet and includes linkage to the balance, c1 denotes compensation weight 1 (tantalum), and c2 denotes compensation weight 2 (titanium).

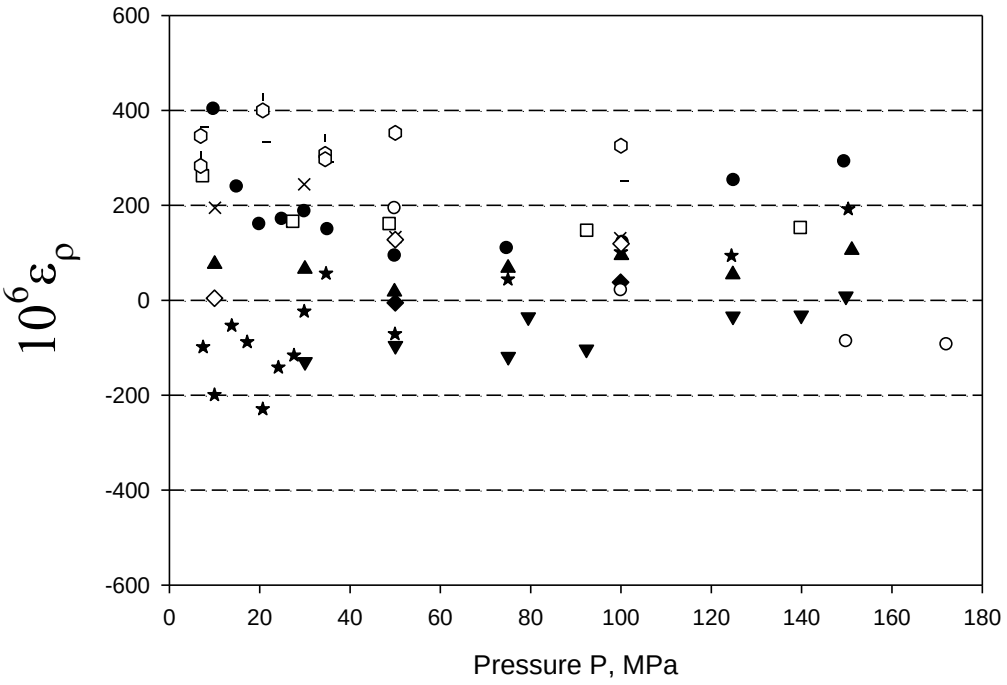

Figure 8. Apparatus constant calculations based on experimental data measured in the high pressure single sinker MSD. Nitrogen ● 265 K, ▲ 298 K, * 350 K; Carbon dioxide ▼ 310 K, ♦ 350 K; Methane – 305 K, ו 340 K, ⎔ 400 K; Ethane × 298 K, ○ 350 K, □ 400 K, ◊ 450 K.

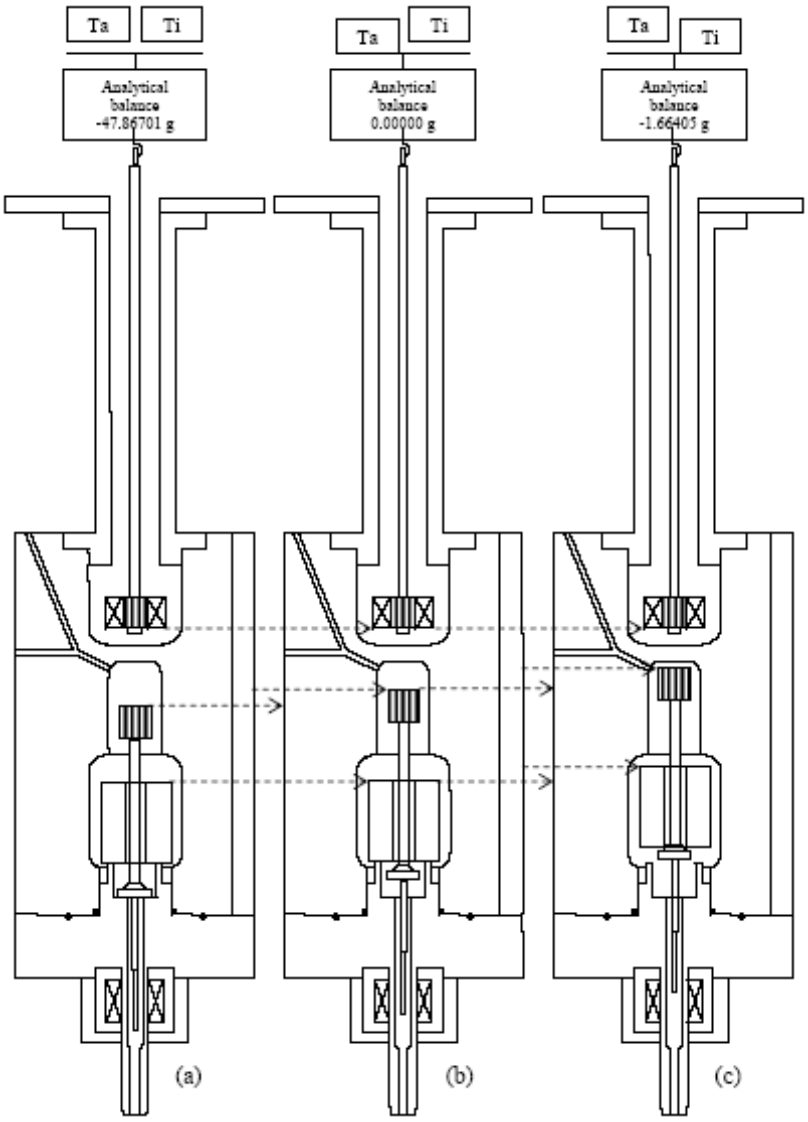

Figure 9. Operation of the single-sinker MSD: a) Suspension control (SC) 'off', Ti and Ta both raised, (b) SC 'on' zero position (ZP), Ta lowered, Ti raised, (c) Measuring position, SC 'on', Ta raised, Ti lowered.

Because $V_{c2} \approx V_{c1}$ and ρ_a are small

$$w_2 - w_1 = \alpha \left\{ \phi \left[m_s - \rho_f V_s \right] + \left(m_{c2} - m_{c1} \right) \right\} \qquad (3.1.1.4)$$

The coupling factor, ϕ, represents the correction to the force balance in the MSD caused by the FTE. For a vacuum measurement in the cell, $\rho_f = 0$ and

$$\left(w_2 - w_1\right)_0 = \alpha\left\{\phi_0 m_s + \left(m_{c2} - m_{c1}\right)\right\} \tag{3.1.1.1.5}$$

Here, ϕ_0 accounts for the apparatus effect of the force transmission error. Combining Eqs. 3.1.1.1.4 and 5,

$$\rho_f = \rho_s\left(1 - \frac{\phi_0}{\phi}\right) + \frac{\left(w_2 - w_1\right)_0 - \left(w_2 - w_1\right)_f}{\phi\alpha V_s} \tag{3.1.1.1.6}$$

and from Eq. 3.1.1.1.4

$$\rho_f = \rho_s + \frac{\left(m_{c2} - m_{c1}\right) - \left(w_2 - w_1\right)_f / \alpha}{\phi V_s} \tag{3.1.1.1.7}$$

Eqs. 3.1.1.1.6 and 7 are equivalent. Now, assuming

$$\rho_f = \rho_{\phi=1} + \Delta\rho_{FTE} \tag{3.1.1.1.8}$$

and postulating

$$\rho_f = \rho_{\phi=1} + \Delta\rho_{ApparatusEffect} + \Delta\rho_{FluidEffect} \tag{3.1.1.1.9}$$

and rewrite Eq. 3.1.1.1.8 as

$$\rho_f = \rho_{\phi=\phi_0} + \Delta\rho_{FluidEffect} \tag{3.1.1.1.10}$$

where

$$\rho_{\phi=\phi_0} \equiv \rho_{\phi=1} + \Delta\rho_{ApparatusEffect} \tag{3.1.1.1.11}$$

which basically corrects the raw density data with the apparatus effect. One important detail is that although the true fluid density ρ_f appears as two terms, the right hand side of Eq. 3.1.11.8 does not change. Density measurements for different fluids performed with two different sinkers (copper and titanium) determine the coupling factor by using Eqs. 3.1.1.1.7 and 8. Now, assuming

$$\Delta\rho_{FluidEffect}\left(T_1, P_1\right) \cong \Delta\rho_{FluidEffect}\left(T_2, P_2\right) \tag{3.1.1.1.12}$$

when (T_1,P_1) and (T_2,P_2) are nearly the same values for the same fluid. Now, combining Eqs. 3.1.1.1.7 and 11 for both titanium and copper sinkers

$$\rho^{s1}_{\phi=\phi_0}\left(T_1,P_1\right)+\Delta\rho_{\text{FluidEffect}}\left(T_1,P_1\right)=\rho_{s1}+\frac{\left(m_{c2}-m_{c1}\right)-\left(w_2-w_1\right)^{s1}_f/\alpha}{\phi V_{s1}} \quad (3.1.1.1.13)$$

$$\rho^{s2}_{\phi=\phi_0}\left(T_2,P_2\right)+\Delta\rho_{\text{FluidEffect}}\left(T_2,P_2\right)=\rho_{s2}+\frac{\left(m_{c2}-m_{c1}\right)-\left(w_2-w_1\right)^{s2}_f/\alpha}{\phi V_{s2}} \quad (3.1.1.1.14)$$

where s1 and s2 stand for sinker 1 (titanium) and sinker 2 (copper). Finally, with Eqs. 3.1.1.1.13 and 14, and the assumption of Eq. 3.1.1.1.1:

$$\phi=\frac{\left(m_{c2}-m_{c1}\right)\left(\frac{1}{V_{s2}}-\frac{1}{V_{s1}}\right)-\frac{1}{\alpha}\left[\frac{\left(w_2-w_1\right)^{s2}_f}{V_{s2}}-\frac{\left(w_2-w_1\right)^{s1}_f}{V_{s1}}\right]}{\left[\rho^{s2}_{\phi=\phi_0}-\rho^{s1}_{\phi=\phi_0}\right]-\left[\rho_{s2}-\rho_{s1}\right]} \quad (3.1.1.1.15)$$

Equation 3.1.1.1.15 is the expression to determine our FTE from the two sinkers experiments.

3.1.1.2 Experimental

To perform the two sinkers experiment, we collected data for four pure compounds (methane, ethane, carbon dioxide, and nitrogen) up to 180 MPa at temperatures ranging between 265 K and 400 K. Methane and nitrogen came from Scott Specialty Gases having a grade of Ultra High Purity (UHP) with mole fractions of 99.99 % and 99.9995 % respectively. Ethane and CO_2 came from Matheson Tri Gas with mole fractions of 99.95 % and 99.999 % respectively. The titanium sinker mass and volume are 30.39159 g and 6.741043 cm^3, and the copper sinker mass and volume are 30.398939 g and 3.403268 cm^3 determined using procedure described by McLinden and Splett [54]. Patil et al. [2, 55] describe the single-sinker MSD, and additional modifications to expand the range of measured temperature appear in refrs 46 and 47. The PRT (Minco Products

model S1059PA5X6) has calibration at fixed temperature points defined by ITS-90 and by a calibrated PRT traceable to NIST. The temperature stability was ±5 mK and the uncertainty of the PRT was 2 mK with respect to the triple point of water [46]. Two Digiquartz® transducers (40 MPa and 200 MPa) from Paroscientific Inc measure pressure. The uncertainty for these transducers is 0.01 % of full scale.

3.1.1.3 Results and Analysis

Table 4 contains the temperatures of the two sinkers experiments performed at pressures up to 180 MPa. All the data were collected at similar pressure and temperature conditions for both sinkers to justify Eq. 3.1.1.1.12. Then, additional data were collected for all the fluids to validate the FTE results The deviations for the raw densities (densities without FTE compensation) compared to densities calculated from EoS [40, 42, 56-57] as implemented in the NIST REPROP 8.0 [26] appear in Figures 10 and 11. The data have considerable deviations in the low-pressure range. This reflects that the FTE affects the low-pressure densities to a greater extent as mentioned by McLinden et al. [51]

Table 4. **Two Sinkers Experiment Temperatures**

Fluid	Copper - Titanium Sinkers
N2	(265, 298, 350) K
CO2	(310, 350) K
CH4	(305, 340, 400) K
C2H6	(298, 400, 450) K

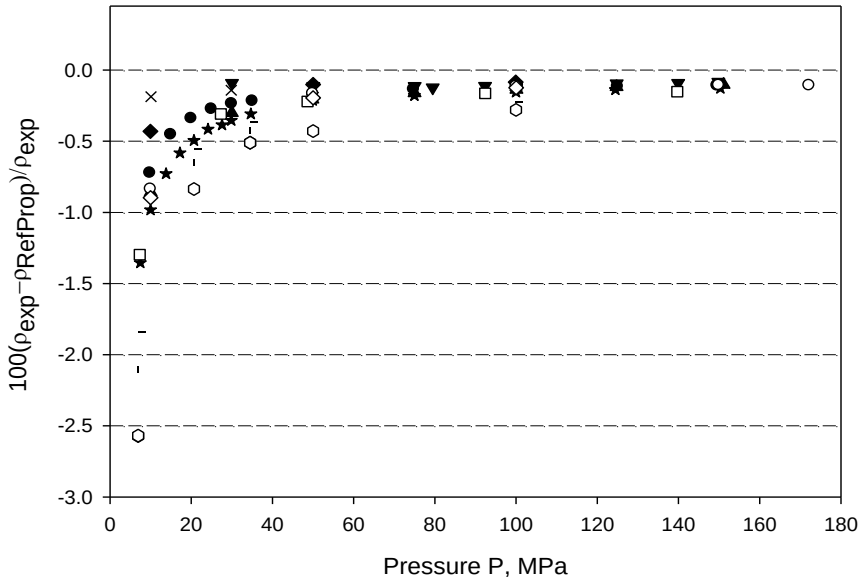

Figure 10. Titanium sinker raw densities ($\phi = 1$) deviations. Nitrogen ● 265 K, ▲ 298 K,* 350 K; Carbon dioxide ▼ 310 K, ♦ 350 K; Methane – 305 K, ו 340 K, ⎔400 K; Ethane × 298 K, ○ 350 K, □ 400 K, ◊ 450 K.

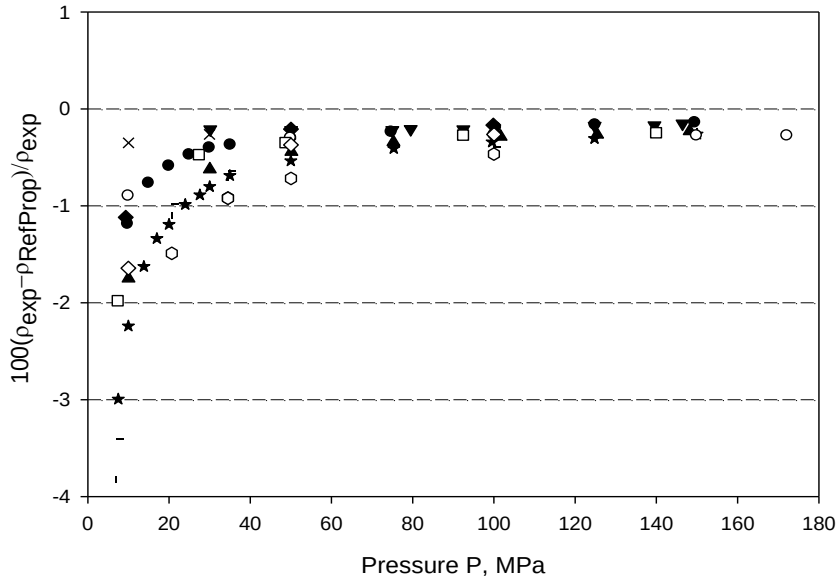

Figure 11. Copper sinker raw densities ($\phi = 1$) deviations. Nitrogen ● 265 K, ▲ 298 K,* 350 K; Carbon dioxide ▼ 310 K, ♦ 350 K; Methane – 305 K, ו 340 K, ⎔ 400 K; Ethane × 298 K, ○ 350 K, □ 400 K, ◊ 450 K.

Then Eqs. 3.1.1.1.11 and 15 determine both $\rho_{\phi=\phi_0}$ and the coupling factor, ϕ, for the copper and titanium sinkers. The determined value for the apparatus effect is about $(\phi_0 - 1)$ = 189 ± 16 ppm for all the experiments. This value corresponds to a correction of about 5.17 mg for our vacuum measurement. The apparatus contribution, ϕ_0, from the FTE for our high-pressure, single-sinker MSD is higher than any reported by McLinden et al. [51]. This result occurs because our cell design accommodates higher pressures (thick walls), and it is diamagnetic (beryllium copper material). The large fluctuations in the apparatus contribution to the FTE result from the two sinkers experiment; every time we change the sinkers, we introduce a considerable uncertainty into the experiment. This is one of the most important difficulties when performing the two sinkers experiment, and it is worse for the high-pressure single-sinker MSD.

Figure 12 shows the value for $(\phi - \phi_0)$ as a function of pressure. This plot reveals two important characteristics of our FTE: our coupling factor does not display significant pressure dependence (i.e. density and the fluctuations for the value $(\phi - \phi_0)$ are clear indications that the fluid contribution is not statistically significant for our MSD. These fundamental facts lead us to conclude that the fluid contribution of the FTE is negligible, and we can assume its independence with temperature and pressure without introducing much uncertainty. This does not mean that a fluid specific effect does not exist, but the apparatus contributions mask that effect. Thus, we compensate our experiments using only the apparatus effect. On the other hand, the 16 ppm of fluctuation in ϕ_0 is in total agreement with the fluctuations of the data when compared to the EoS as implemented in REFPROP 8.0 for the different fluids. This behavior is obvious in Figure 13.

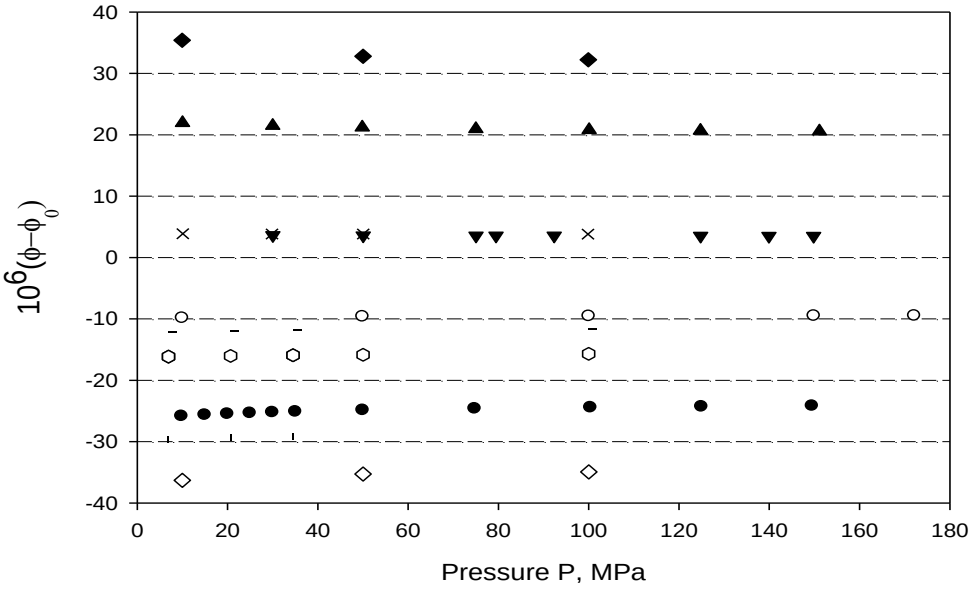

Figure 12. $(\phi - \phi_0)$ Values for the two-sinkers experiment. Nitrogen ● 265 K, ▲ 298 K; Carbon dioxide ▼ 310 K, ♦ 350 K; Methane – 305 K, ו 340 K, ⎔ 400 K; Ethane × 298 K, ○ 350 K, ◊ 450 K.

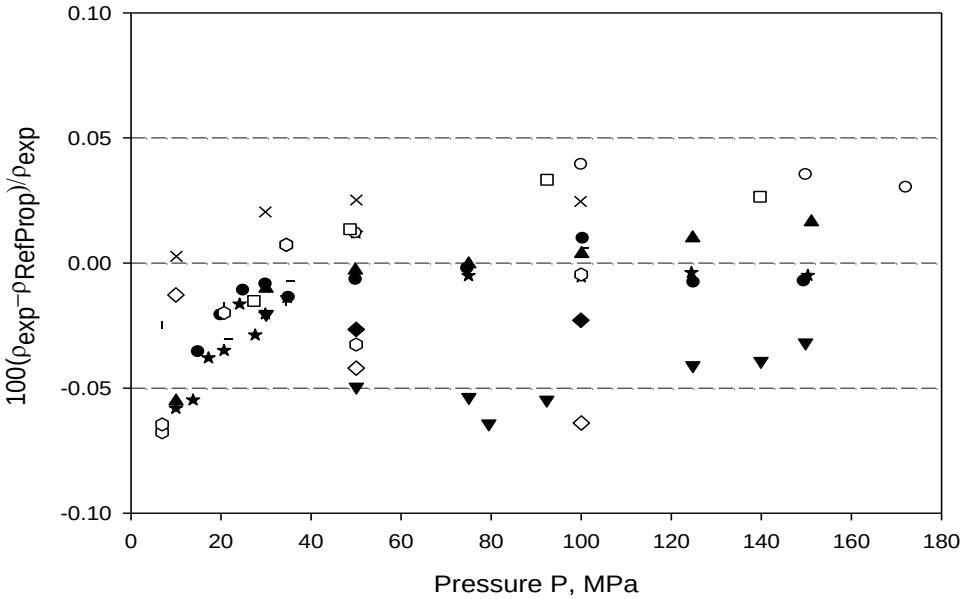

Figure 13. Titanium sinker corrected densities deviations. Nitrogen ● 265 K, ▲ 298 K,* 350 K; Carbon dioxide ▼ 310 K, ♦ 350 K; Methane – 305 K, ו 340 K, ⎔ 400 K; Ethane × 298 K, ○ 350 K, □ 400 K, ◊ 450 K.

Figure 13 indicates that our experimental data for pure compounds lie within a 2σ deviation band of 0.05 %. Higher deviations appear at pressures below 7 MPa caused by the intrinsic characteristics of the high-pressure, single-sinker MSD and its ancillary equipment. However, the low-pressure data fall within the experimental uncertainty.

An additional experimental observation is that the data measured with the copper sinker have higher deviations compared to RefProp 8.0 than the densities measured with the titanium sinker as apparent in Figure 14. This could be an effect caused by the differences between the sinker densities and the fluid densities. The density of copper is almost twice the density of titanium (8905.54 kg· m^{-3} and 4508.44 kg· m^{-3} respectively). Therefore, for more experimental accuracy, the density of the sinker should be as close as possible to the fluid density. McLinden et al. [51] and Wagner et al. [50] also reach this conclusion.

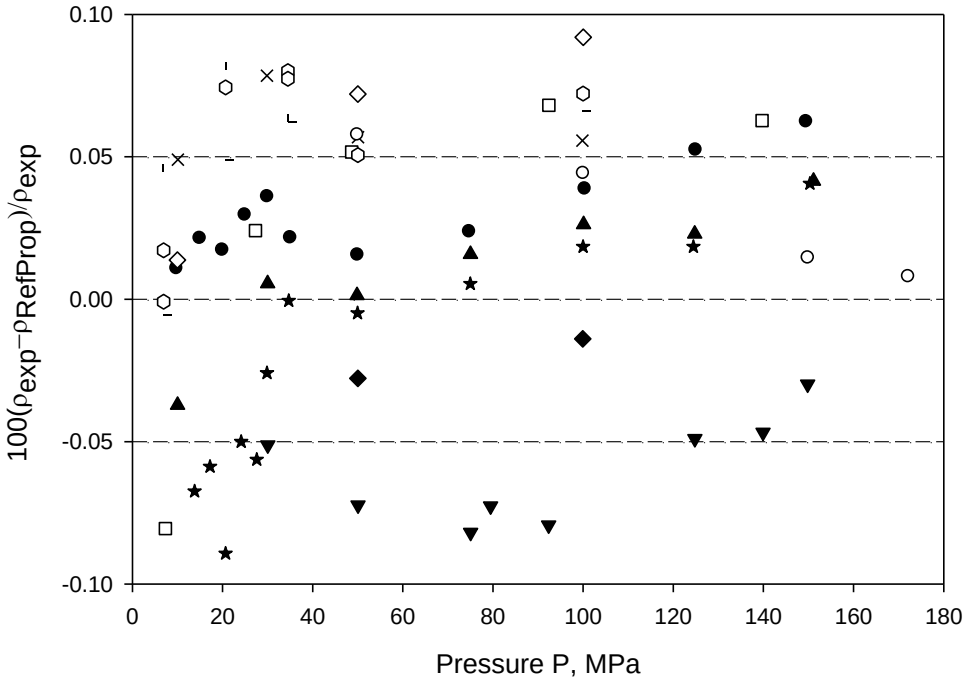

Figure 14. Copper sinker corrected densities deviations. Nitrogen ● 265 K, ▲ 298 K,* 350 K; Carbon dioxide ▼ 310 K, ♦ 350 K; Methane – 305 K, ו 340 K, ⎔ 400 K; Ethane × 298 K, ○ 350 K, □ 400 K, ◊ 450 K.

3.1.2 Pure Compounds $P\rho T$ Data

A first step to determine the performance of our MSD, after the FTE determination, is to measure and compare high purity pure compound $P\rho T$ data to the RefProp 8.0 [26]. Data for methane and ethane, the primary constituents of natural gas, have been measured. A detailed analysis for these data follows.

3.1.2.1 Accurate $P\rho T$ Data for Methane From (300 To 450) K Up to 180 Mpa

Methane is the principal constituent of natural gas and an important raw material for many industrial processes. Accurate thermophysical property data for methane are necessary for design and evaluation of these processes. Setzmann and Wagner [40] make an extensive analysis of the thermodynamic data for methane reported before 1991. On the basis of the uncertainty analysis of the data sources, they define three groups of data: group 1 has the most consistent sets of data and lower experimental uncertainties, and the other two groups do not follow their predefined quality standards. They have developed an EoS, using the group 1 data, based upon an explicit Helmholtz energy function with 40 coefficients. They claim a relative uncertainty in the density predictions of 0.03 % up to 12 MPa and from 0.03 % to 0.15 % for higher pressures.

Setzmann and Wagner [40] provide a detailed description of the data used for fitting their EoS. Four sets of data reside in group 1 for pressures greater than 35 MPa: Trappeniers et al., [58] (2 to 260) MPa; Morris, [59] (130 to 690) MPa; Mollerup, [60] (0.2 to 72) MPa; and Kortbeek and Schouten, [61] (150 to 1000) MPa. Mollerup reports an uncertainty in density of $10^{-3}\,\rho$, and Setzman and Wagner estimate the uncertainties for Kortbeek and Schouten at $10^{-3}\,\rho$ with Trappeniers et al. and Morris at $5 \cdot 10^{-4}\,\rho$.

Data for methane at (298, 305, 338, 400 and 450) K up to 180 MPa were measured. The methane came from Scott Specialty Gases having a grade of Ultra High Purity (UHP) with a mole fraction of 99.99 % methane. The characteristics of the MSD are the same as described in the FTE analysis. After compensation for the FTE in the raw data and based upon the assumption of uncorrelated errors for the different sources of error such as temperature and pressure, the uncertainty for our data is $3 \cdot 10^{-4}\,\rho$ for pressures greater than 7 MPa and up to $5 \cdot 10^{-4}\,\rho$ for pressures between 5 MPa and 7 MPa.

The two reported uncertainties exist because our MSD uses two different pressure transducers (40 MPa and 200 MPa), and they do not produce a uniform uncertainty across the entire range of pressures.

3.1.2.1.1 Results and Analysis

The five sets of isothermal data appear in Table 5, along with the predicted densities obtained from RefProp 8.0 [26]. The last column in the table contains the deviations with respect to the experimental data. Figure 15 shows a comparison between our experimental data and those of Trappeniers et al.[58], Mollerup [60], and Kortbeek and Schouten [61] referenced to RefProp 8.0 predictions.

Table 5. Measured Density Values for Methane

T/K	P/MPa	ρ/ kg· m^{-3}	ρ/ kg· m^{-3} (RefProp 8.0)	$100\cdot(\rho-\rho_{RefProp})/\rho$
		T = 298.15 K		
298.156	1.012	6.665	6.665	-0.001
298.189	5.009	35.316	35.329	-0.039
298.149	10.010	76.080	76.078	0.003
298.249	14.994	118.506	118.512	-0.005
298.145	20.012	157.172	157.183	-0.007
298.138	29.958	212.508	212.485	0.011
298.144	35.056	232.422	232.377	0.019
298.139	49.959	273.189	273.169	0.007
298.157	66.961	303.605	303.563	0.014
298.150	79.980	321.098	321.030	0.021
298.144	99.874	342.269	342.183	0.025
298.138	124.934	363.139	363.026	0.031

Table 5. Continued

T/K	*P*/MPa	ρ/ kg· m^{-3}	ρ/ kg· m^{-3} (RefProp 8.0)	$100\cdot(\rho-\rho_{RefProp})/\rho$
298.141	150.062	380.039	379.913	0.033
298.138	159.617	385.731	385.591	0.036
298.142	170.054	391.531	391.416	0.029
298.143	185.333	399.489	399.340	0.037
298.145	186.931	400.257	400.131	0.032
298.142	188.059	400.837	400.688	0.037
		T = 305.24 K		
305.236	5.001	34.173	34.175	-0.007
305.235	6.897	48.435	48.438	-0.006
305.231	9.993	72.932	72.931	0.002
305.240	15.006	113.440	113.440	0.000
305.242	20.696	155.024	155.030	-0.004
305.239	29.976	205.443	205.430	0.006
305.239	34.563	223.779	223.755	0.011
305.230	49.968	267.232	267.252	-0.008
305.233	60.012	287.019	287.012	0.002
305.239	69.988	302.917	302.884	0.011
305.227	79.855	316.163	316.098	0.020
305.234	99.904	337.939	337.879	0.018
305.233	124.930	359.159	359.090	0.019
305.225	149.862	376.248	376.153	0.025
		T = 338 K		
338.049	5.000	29.983	29.986	-0.009
338.037	6.905	42.093	42.086	0.017

Table 5. Continued

T/K	*P*/MPa	ρ/ kg· m^{-3}	ρ/ kg· m^{-3} (RefProp 8.0)	$100\cdot(\rho-\rho_{RefProp})/\rho$
338.103	9.969	62.054	62.044	0.016
338.079	15.026	95.246	95.243	0.003
338.082	20.687	130.132	130.139	-0.005
338.080	30.005	177.380	177.371	0.005
338.048	34.473	195.446	195.453	-0.004
338.083	50.031	241.969	242.001	-0.013
338.079	59.971	263.229	263.250	-0.008
338.063	70.001	280.639	280.679	-0.014
338.103	80.310	295.610	295.648	-0.013
338.112	99.908	318.744	318.719	0.008
338.068	124.895	341.685	341.626	0.017
338.066	149.542	359.787	359.752	0.010
338.094	164.905	369.665	369.505	0.043
338.121	179.829	378.164	378.121	0.011
		T = 400 K		
400.068	5.005	24.610	24.618	-0.031
400.013	6.915	34.195	34.199	-0.011
400.015	10.002	49.746	49.744	0.005
400.029	13.795	68.723	68.704	0.027
399.988	15.027	74.789	74.786	0.005
400.025	20.675	101.642	101.644	-0.002
399.984	30.014	141.158	141.137	0.015
400.036	34.510	157.640	157.611	0.019
400.001	50.037	203.469	203.518	-0.024

Table 5. Continued

T/K	*P*/MPa	ρ/ kg· m^{-3}	ρ/ kg· m^{-3} (RefProp 8.0)	$100\cdot(\rho-\rho_{RefProp})/\rho$
399.967	59.973	225.951	225.977	-0.011
400.042	69.978	244.725	244.750	-0.011
400.003	79.920	260.652	260.674	-0.009
399.943	89.964	274.637	274.631	0.002
400.089	99.984	286.800	286.796	0.001
400.022	124.882	312.062	312.064	-0.001
400.023	149.627	332.136	332.150	-0.004
		T = 450 K		
450.091	6.886	29.741	29.747	-0.022
450.010	20.697	87.478	87.464	0.016
450.048	30.002	121.791	121.792	-0.001
450.115	34.492	136.647	136.635	0.009
450.057	50.036	179.955	179.987	-0.018
450.027	59.975	202.137	202.170	-0.017
450.064	69.966	221.073	221.139	-0.030
450.083	80.008	237.571	237.606	-0.015
450.025	89.981	251.923	251.957	-0.013
450.011	99.932	264.608	264.645	-0.014
450.018	119.918	286.376	286.412	-0.013
450.034	139.476	304.187	304.188	0.000

Figure 15 demonstrates the deviations compared to our experimental data. It is clear that the calculations from the Setzmann and Wagner EoS are in excellent agreement with our experimental data, and that the predictions from the equation are better than expected for pressures greater than 12 MPa.

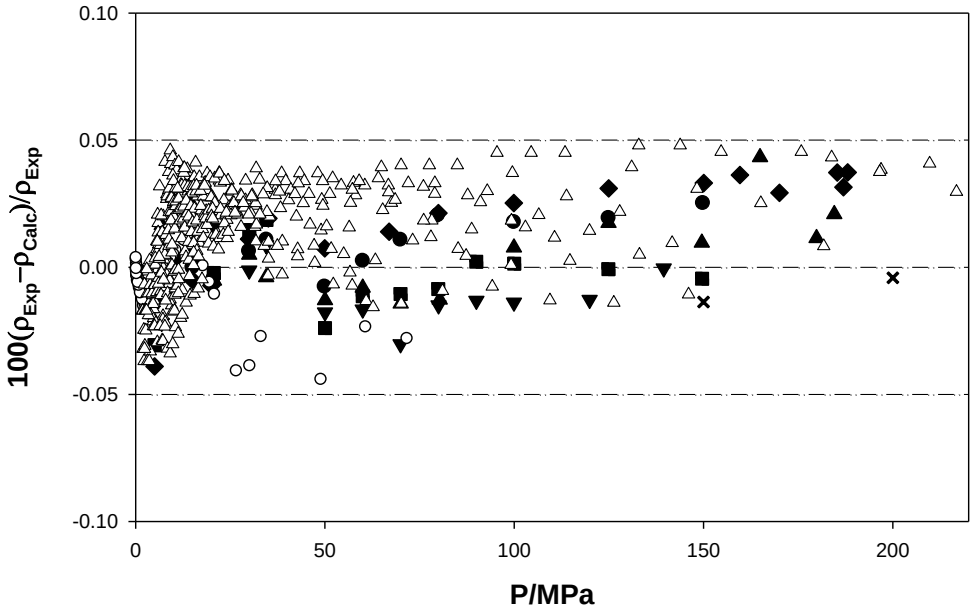

Figure 15. Percentage deviation of the experimental $P\rho T$ data from values calculated using Setzmann and Wagner [40]. This work ♦ 298 K, ● 305 K, ▲ 338 K, ■ 400 K, ▼ 450 K; ref 58, Δ (273.25 to 423.25) K ; ref 60, ○ 310 K: ref 61, x 298.15 K.

Second and third virial coefficients determined from the $P\rho T$ data indicate that extrapolation of the data into the low pressure range is reliable. Figure 16 presents the methodology to evaluate the second and third virial coefficients at 298 K. The selected low-density data exhibit both a linear trend and have good correlation coefficients.

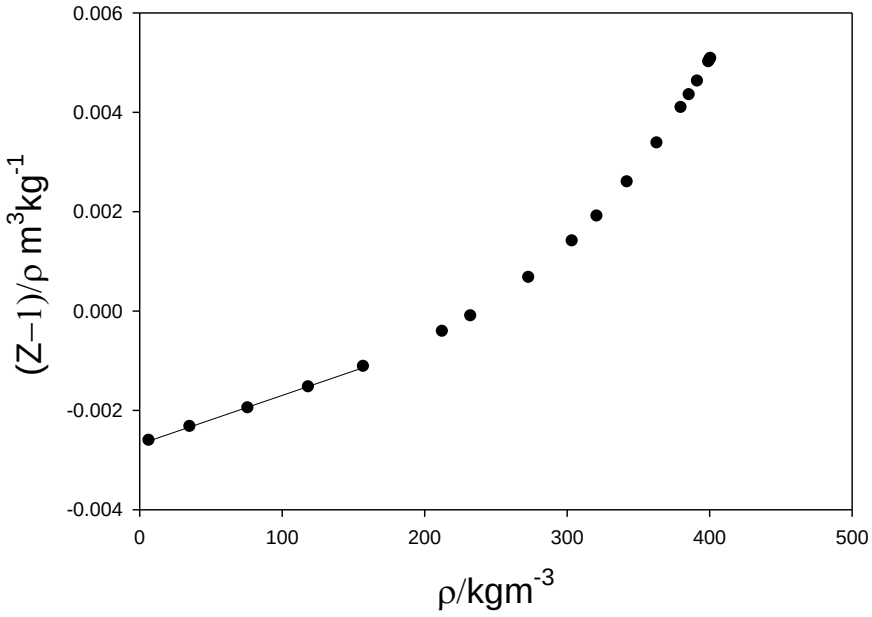

Figure 16. Procedure for the determination of the second virial coefficient using 298 K data. The intercept value, determined by mean square regression, is -0.002681 m^3kg^{-1}, the slope is $9.82x10^{-6}$ $(m^3kg^{-1})^2$ and the correlation coefficient R^2 is 0.999.

Figures 17 and 18 present comparisons of literature data [62-65] to the current data referenced to the Setzmann and Wagner equation. Most of these data lie in a band with an absolute deviation of 0.2 $cm^3 \cdot mol^{-1}$ for the second virial coefficients and of 150 $(cm^3 \cdot mol^{-1})^2$ for the third virial coefficients. The estimated uncertainty for the second and the third virial coefficients are respectively 0.57 $cm^3 \cdot mol^{-1}$ and 125 $(cm^3 \cdot mol^{-1})^2$. The current values for the 450 K virial coefficients have a higher absolute deviation of 0.48 $cm^3 \cdot mol^{-1}$ and 301.2 $(cm^3 \cdot mol^{-1})^2$, which is a reflection of the paucity of low-density data taken for this isotherm. However, it appears that the apparatus is capable of determining second and third virial coefficients. The second and third virial coefficients values appear in Table 6.

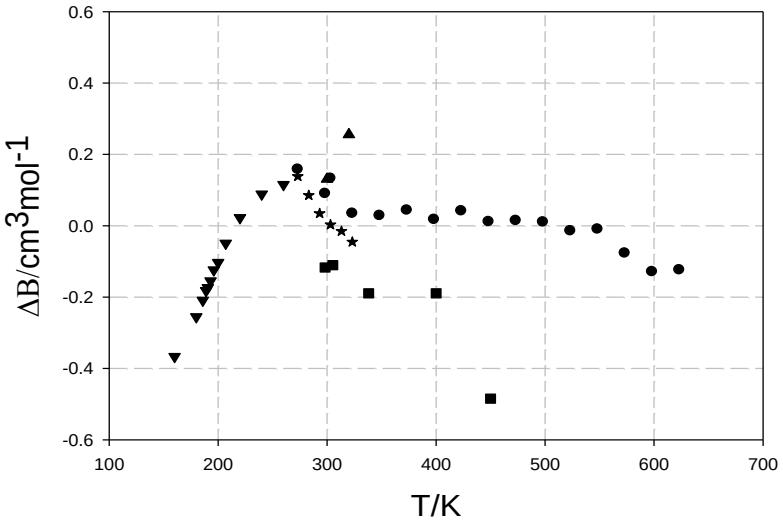

Figure 17. Absolute deviations for second virial coefficient from values calculated using the Setzmann and Wagner [40] equation of state $\Delta B = (B_{exp} - B_{calc})$. This work ■; ref 62 ●; ref 63 ★; ref 64 ▲; ref 65 ▼.

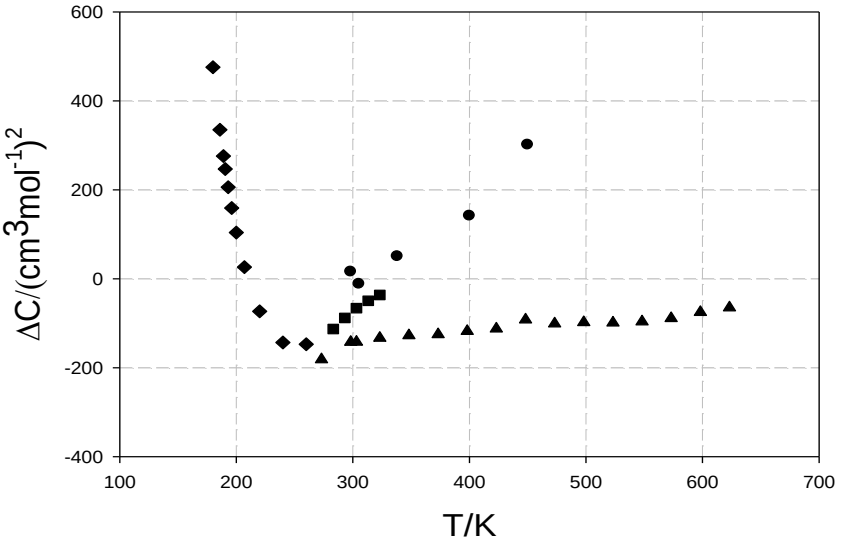

Figure 18. Absolute deviations for third virial coefficient from values calculated using the Setzmann and Wagner [40] equation of state $\Delta C = (C_{exp} - C_{calc})$. This work ●; ref 62 ▲; ref 63 ■; ref 65 ♦.

Table 6. Second and Third Virial Coefficients for Methane

T/K	B/(cm^3mol^{-1})	C/(cm^3mol^{-1})^2
298.190	-43.01	2527.8
305.235	-40.40	2430.1
338.092	-30.01	2220.5
400.017	-15.72	1978.8
450.038	-7.78	1973.2

3.1.2.2 Accurate $P\rho T$ Data for Ethane From (298To 450) K up to 200 MPa

Ethane is the second most abundant constituent of natural gas and an important raw material for many industrial processes and scientific applications. Accurate thermophysical property data for ethane are necessary for design and evaluation of these processes. Bücker and Wagner [42] make an extensive analysis of the thermodynamic data for ethane reported before of 2006. Based upon the uncertainty analysis of the data sources, they define three different groups of data: group 1 has the most consistent sets of data and lower experimental uncertainties, the other two groups do not follow their predefined quality standards. They have developed an EoS, using the group 1 data, based upon an explicit Helmholtz energy function with 44 coefficients. They claim a relative uncertainty in the density predictions of 0.02%-0.03% from the melting line up to temperatures of 520 K and pressures of 30 MPa.

Bücker and Wagner[42] provide a detailed description of the data used for fitting their EoS. Two sets of data reside in group 1 for pressures greater than 30 MPa and below than 200 MPa, Pal et al. [66] (0.52 to 73) MPa, Golovskii et al. [67] (1.2 to 60) MPa. The estimated relative uncertainties by Bücker and Wagner for the Pal et al. and Golovskii et al. data are 0.40% and 0.25% respectively. Byun et al. [68] published an additional set of high pressure data from (15 to 276) MPa; however these data have high relative deviations, up to 7%, compared to Bücker and Wagner EoS. Therefore, we do not include these data in our analysis. No additional, reliable data within the range temperatures and pressures of concern to this publication appear in the literature for comparison.

Density data for ethane at (298, 350, 400 and 450) K up to 200 MPa were measured. The ethane came from Matheson Tri Gas having a grade of Ultra High Purity (UHP) with mole fractions of 99.95% ethane. The data was corrected using the FTE analysis.

3.1.2.2.1 Results and Analysis

The four sets of isothermal data appear in Table 7, along with the predicted densities obtained from the Bücker and Wagner EoS as implemented in RefProp 8.0. [26]. The last column in the table contains the deviations with respect to the experimental data.

Table 7. Measured Density Values for Ethane

***P*/MPa**	**ρ/ kg· m^{-3}**	**ρ/ kg· m^{-3} (RefProp 8.0)**	**$100\cdot(\rho-\rho_{RefProp})/\rho$**
		T= 298.150 K	
2.000	29.226	29.228	-0.004
5.987	352.999	353.033	-0.010
7.909	371.593	371.571	0.006
10.071	385.867	385.799	0.018
14.959	407.911	407.811	0.024
20.004	423.934	423.827	0.025
24.927	436.235	436.121	0.026
29.893	446.599	446.474	0.028
35.020	455.820	455.683	0.030
39.905	463.582	463.434	0.032
49.977	477.362	477.162	0.042
75.091	503.592	503.383	0.041

Table 7. Continued

P/MPa	ρ/ kg· m^{-3}	ρ/ kg· m^{-3} (RefProp 8.0)	$100\cdot(\rho-\rho_{RefProp})/\rho$
99.827	523.125	522.954	0.033
119.760	536.225	536.070	0.029
149.807	552.995	552.905	0.016
		T= 350.000 K	
1.999	22.819	22.814	0.024
29.974	384.889	384.905	-0.004
49.928	430.315	430.124	0.044
74.959	464.696	464.424	0.058
100.019	489.111	488.825	0.058
124.863	508.192	507.902	0.057
149.906	524.195	523.931	0.050
172.157	536.528	536.301	0.042
		T= 400.000 K	
0.805	7.452	7.453	-0.016
7.325	84.481	84.487	-0.006
27.286	311.921	311.899	0.007
48.575	383.533	383.354	0.047
69.346	421.214	421.012	0.048
92.289	450.020	449.796	0.050
117.459	473.901	473.683	0.046
139.686	491.026	490.822	0.041
154.657	501.119	500.927	0.038
166.558	508.474	508.315	0.031
181.565	517.111	516.954	0.030

Table 7. Continued

***P*/MPa**	**ρ/ kg· m^{-3}**	**ρ/ kg· m^{-3} (RefProp 8.0)**	**$100\cdot(\rho-\rho_{RefProp})/\rho$**
196.062	524.823	524.691	0.025
		T= 450.000 K	
1.998	16.685	16.685	0.002
5.021	44.467	44.464	0.007
10.001	96.599	96.581	0.019
20.005	202.282	202.249	0.016
30.018	272.417	272.340	0.028
49.974	346.238	346.020	0.063
69.967	388.105	387.843	0.068
79.928	403.693	403.405	0.072
99.962	429.113	428.804	0.072
119.860	449.290	448.977	0.070
139.478	465.963	465.650	0.067

Figure 19 is a comparison between our experimental data and those of Pal et al.[66] and Golovskii et al. [67] referenced to RefProp 8.0 predictions. It is clear that the calculations from the Bücker and Wagner EoS are in excellent agreement with our experimental data, and that the predictions from the equation are better than expected for pressures greater than 30 MPa.

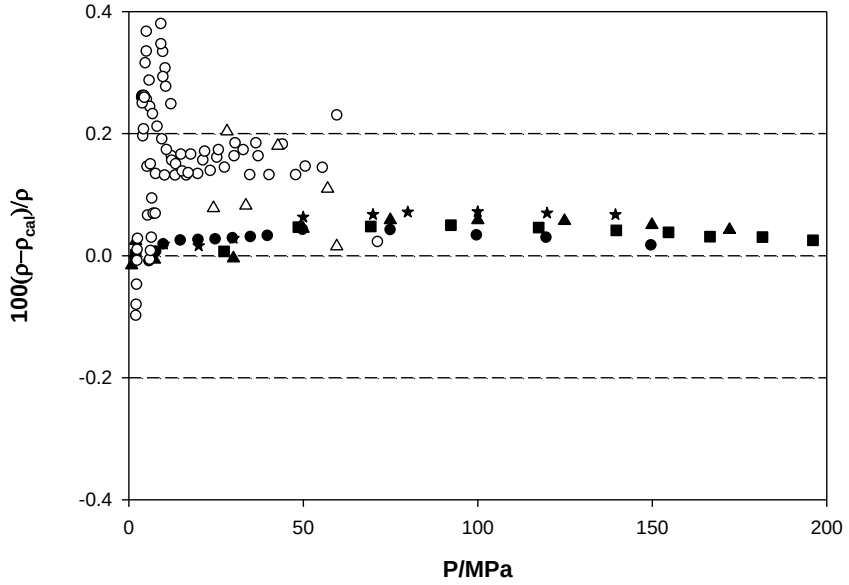

Figure 19. Percentage deviation of the experimental $P\rho T$ data from values calculated using the Bücker and Wagner [42] equation of state. This work ● 298.150 K, ▲ 350.000 K, ■ 400 K, ★ 450 K; ref 66, ○ (290 to345) K ; ref673, Δ (255 to 270) K.

Second and third virial coefficients determined from the $P\,\rho\,T$ data (as described earlier) indicate that extrapolation of the data into the low pressure range is reliable. No virial coefficients were determined for the isotherm 298.150 K because only a single vapor datum was available for the extrapolation. Figures 20 and 21 present comparisons of experimental literature data [62, 69-70] along with the current data based upon the Bücker and Wagner equation.

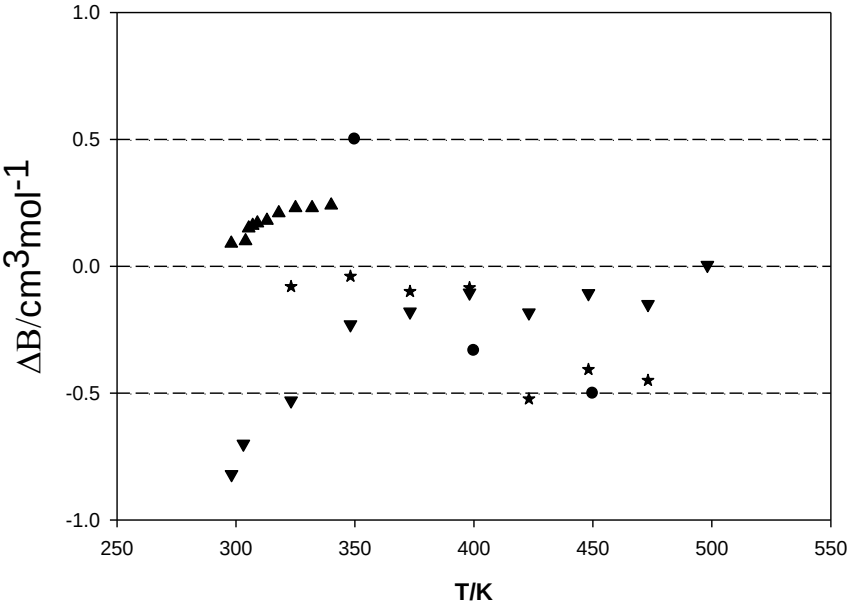

Figure 20. Absolute deviations for second virial coefficient from values calculated using the Bücker and Wagner [42] equation of state $\Delta B = (B_{exp} - B_{calc})$. This work ● ; ref 62 ▲; ref 15 69 ; ref 70★.

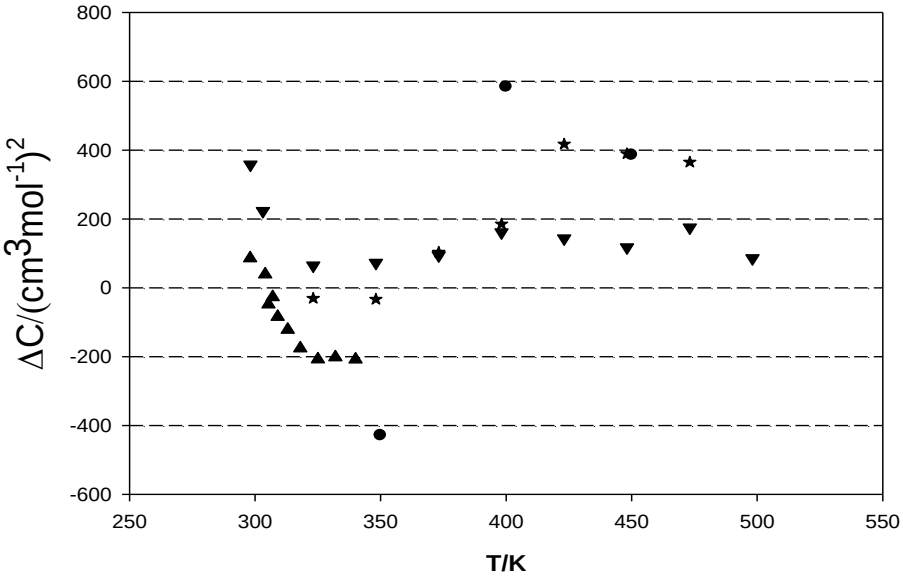

Figure 21. Absolute deviations for third virial coefficient from values calculated using the Bücker and Wagner [42] equation of state $\Delta C = (C_{exp} - C_{calc})$. This work ● ; ref 62 ▲; ref 69 ▼ ; ref 70★.

Most of these data lie in a band with absolute deviation of 0.5 $cm^3 \cdot mol^{-1}$ for the second virial coefficients and of 500 $(cm^3 \cdot mol^{-1})^2$ for the third virial coefficients. The estimated uncertainty for the second and the third virial coefficients are respectively 0.57 $cm^3 \cdot mol^{-1}$ and 270 $(cm^3 \cdot mol^{-1})^2$.Therefore, it appears that our apparatus is capable of determining second and third virial coefficients. The second and third virial coefficients values for ethane appear in Table 8.

Table 8. Second and Third Virial Coefficients for Ethane

T/K	$B/(cm^3 mol^{-1})$	$C/(cm^3 mol^{-1})^2$
350.000	-130.71	8084
400.000	-96.43	7327
450.000	-71.29	5912

3.2 Isochoric and Phase Equilibrium Data

Isochoric data are a valuable source of data for densities and vapor-liquid equilibrium of mixtures [71]. Since the publication of the Griffiths' proof of the collinearity constraints [72] and some alternatives approaches using isochoric data as a source of equilibrium information for mixtures [73], several theoretical and experimental investigations have taken advantage of the "change of slope" method[74-76]. The "change of slope" utilizes the break in the slope of the isochoric data when moving from the one-phase region to the two-phase region. With this information it is possible to determine dew and bubble points of phase envelopes for mixtures.

The Thermodynamics research group at Texas A&M University has built a low pressure isochoric apparatus to use the "change of slope" technique for the determination of natural gas mixtures phase loops [17, 77]. Coupling isochoric data with the isothermal density data from the MSD provides complementary information for these techniques. The pressure limitations of the isochoric apparatus developed in the past restrict the determination of the bubble points for natural gas mixtures. Therefore we decided to extend the range of the isochoric data by building a high pressure apparatus. The high

pressure isochoric apparatus was designed and constructed to work up to 200 MPa over the range of (100 to 500) K. With the capabilities of this new apparatus, the low pressure isochoric apparatus and the MSD, we now possess the infrastructure to characterize natural gas mixtures over a wide thermodynamic space with high accuracy.

Finally, we determined the uncertainty for the "change of slope" method. A new methodology to determine the saturation density from the isochoric and the isothermal data was resulted as well as a technique to correct the isochoric slopes.

3.2.1 Low Pressure Isochoric Apparatus

Zhou [17] developed the low pressure isochoric apparatus. A detailed description appears in [17, 77]. Table 9 contains the principal features of this apparatus.

Table 9. Low Pressure Isochoric Apparatus Features

Temperature Range	100K to 500K 0.02% accuracy ± 3mK stability ± 2mK ΔT across the cell
Pressure Range	up to 35 MPa 0.01% accuracy (full scale)

However, during this project we made some improvements to this apparatus while conserving its main characteristics. A new Varian DS-202 mechanical pump improved the vacuum system. We reassembled the apparatus in a new portable frame, which allowed a more versatile positioning in the lab space, Figure 22. These new features also facilitated implementation of simultaneous experiments using both the MSD and the new high-pressure isochoric apparatus. Additional modifications were implemented to the automated control system in LabView 6.1. Changing the control loop strategy achieved a better stability and almost zero gradients over the entire range of temperatures. Now the electrical trim heater at the top of the isochoric cell possesses an independent PID control, with the temperature gradient between the bottom and the

top part of the cell used as a set point. This modification reduces gradients present at low temperature.

Figure 22. Low-pressure isochoric apparatus.

3.2.2 High Pressure Isochoric Apparatus

The new high pressure isochoric apparatus system includes several principal and ancillary instruments. It consists of an isochoric cell of beryllium cupper (Cu-Be 175). The cell has been tested up to 340 MPa at room temperature and has a volume of 10.5 cm^3 [78]. Figure 23 presents a view of the isochoric apparatus.

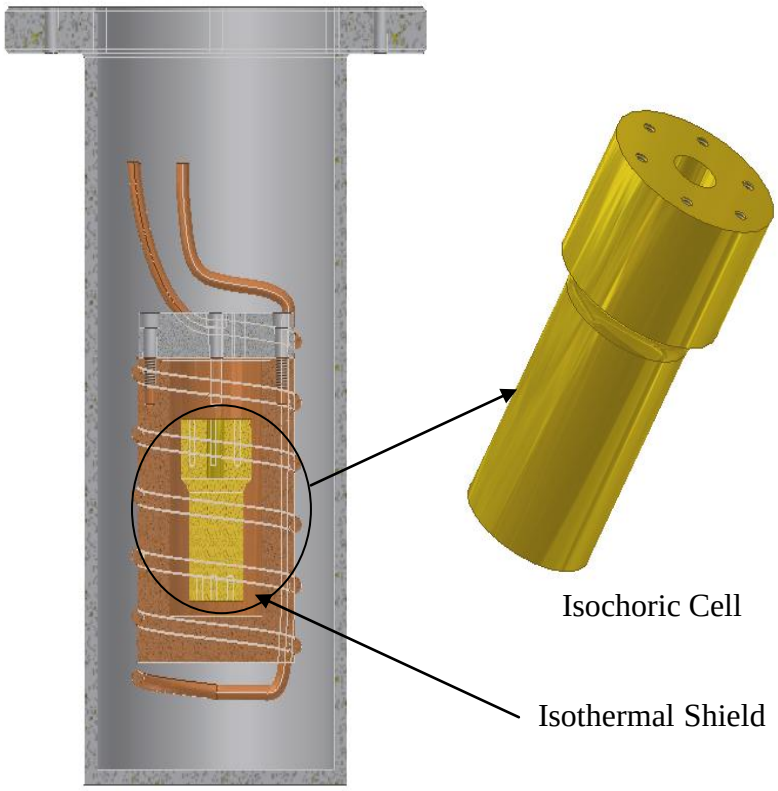

Figure 23. Cut view of new isochoric apparatus.

The ancillary instruments are: a cylinder storage hot box, feed charging and discharging manifolds, temperature control heat exchangers around the high pressure cell, two external isothermal shields, pressure and temperature measurement systems, a compressor, a vacuum system, a heating/cooling liquid constant-temperature circulation bath and a computer for data acquisition and control. Figure 24 is a picture of the high pressure isochoric apparatus.

The cylinder storage hot box and the feed charging manifold are those described by Atilhan [79] and Ejaz [46]. Some modifications that allow the simultaneous use for both the MSD and the high pressure isochoric apparatus appear in Figure 25. A system of two three way/two stem connection valves (FV1 and FV2) allow use the vacuum and the feed charging manifold as desired. The valves came from HIP and are operable up to 60,000 psia.

Figure 24. High pressure isochoric apparatus.

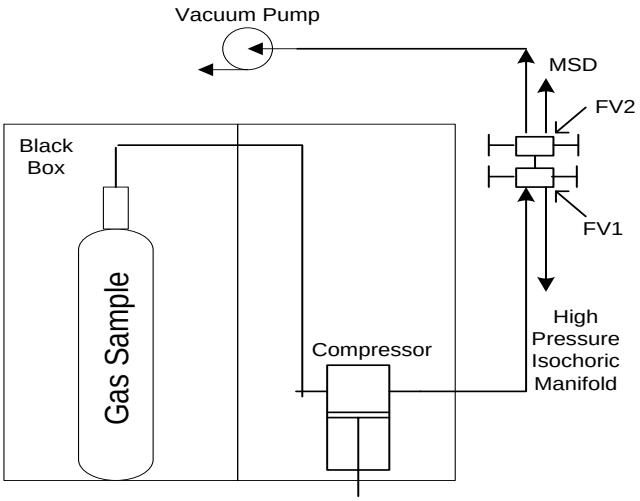

Figure 25. Feeding section of both the MSD and the high-pressure isochoric apparatus.

A high pressure manifold allows feeding and discharging the high-pressure isochoric cell. It consists of four high-pressure valves (30,000 psia), a high-pressure hand pump model #37-6-30 with a capacity of 11 cc, POLYPAK B-1372 (30,000 psia) for fine-tuning the pressure and the tubing lines (up to 60,000 psia) all coming from HIP. Finally it has a high-pressure gauge for monitoring the inlet pressure to the isochoric cell.

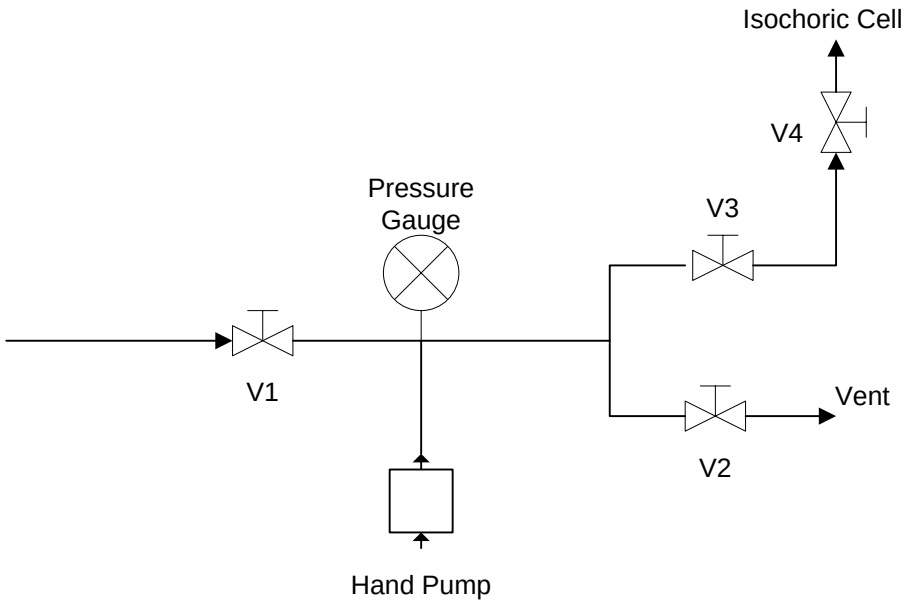

Figure 26. High pressure isochoric manifold.

The configuration of the high pressure isochoric cell and the pressure transducer appears in Figure 27. The tubing line between the isochoric cell and the pressure transducer has a volume less than 0.1% the volume of the cell as recommended by Matabe [80]. The pressure transducer is an oil-free, absolute pressure resonating crystal pressure transducer, model 430K-101 (Paroscientific, Inc). This instrument has automatic temperature compensation (the equation and parameters are in Appendix A). Location in an aluminum block allows temperature control and guarantees better stability. The aluminum block thermostating system includes a three-lead PRT, an auto-

tune PID temperature controller, a solid state relay (SSR) switch, a cartridge heater (all supplied by Omega Engineering) and a variable AC power supply. The PRT used in the thermostat is a three lead, ceramic encapsulated, 100 Ω PRT (Omega model: RTD-2-1PT100KN2528-108-T). The temperature stability achieved by this system is of ±0.1 ^{o}C. Additional temperature control of the feeding line uses a simple PID control scheme with Clayborn precision heat tape. The temperature was set to 60 ^{o}C to minimize the moles contained in the tubing line during operation.

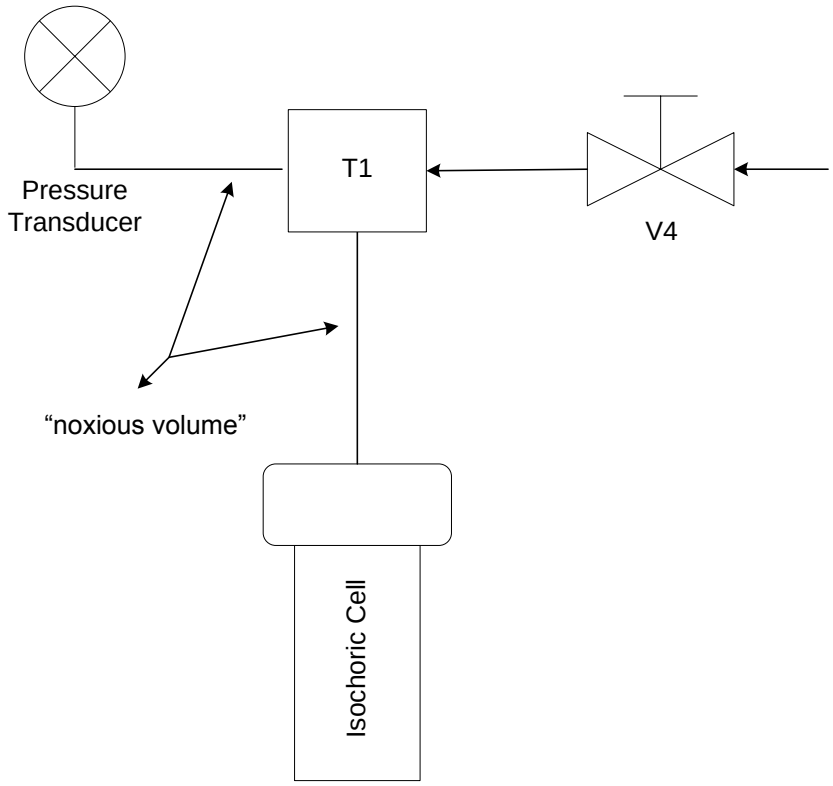

Figure 27. Isochoric cell and pressure transducer configuration.

A vacuum system achieves high vacuum in the isochoric apparatus. It consists of a mechanical vacuum pump from Welch Duo-Seal®, model 1402, a diffusion pump model 0159 and a vacuum gauge model 801 from Varian Inc. A cold trap located between the diffusion pump and the vacuum line going to the isochoric apparatus

reduces the backflow of oil molecules. A schematic of the vacuum system appears in Figure 28.

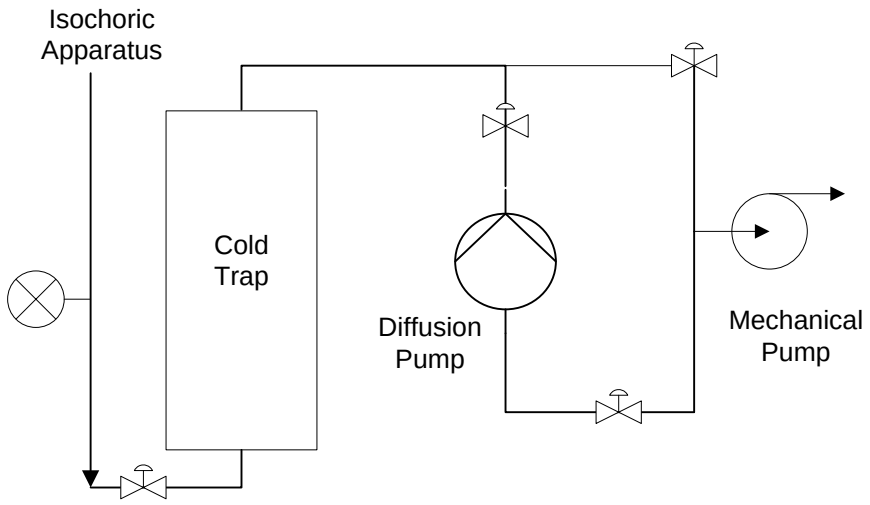

Figure 28. Vacuum system.

3.2.2.1 Temperature Control

A robust physical and digital control scheme establishes an optimum temperature control for the high-pressure isochoric apparatus. Figure 29 is a detailed, cut view of the isochoric apparatus. The isochoric apparatus consists of an external aluminum chamber, insulated with a fiberglass layer and an additional layer of spiral-on thermal insulated tape made of a high quality cork and synthetic rubber (Parker Products, Inc). This insulation provides an excellent isolation for the isochoric system from the surroundings. Two internal and external shields are between the external chamber and the isochoric cell. These shields are sources or sinks of heat for temperature control. High vacuum applied to the interior of the external chamber makes radiation the predominant mechanism for heat transfer between the shields and the isochoric cell.

A four wire PRT (Platinum Resistance Thermometer) from Minco® measures the temperature at the bottom of the high-pressure isochoric cell. The measurement methodology is similar to that described by Zhou [17], Atilhan [47] and Ejaz [46]. Based upon this technique, the temperature measurements have a resolution of less than 0.1 mK. The calibration parameters for the PRT used in this apparatus are in Appendix B.

Four heaters are located in the isochoric system (labeled as H1, H2, H3 and H4). H1 and H4 control the temperature gradient across the cell. They have a separate PID control loop to keep the temperature gradient below 3 mK. At very low temperatures (around 120 K), this task becomes more difficult because of heat conduction from the feed line and the aluminum platform to the isochoric cell. Therefore, the low temperature range has a gradient of 10 mK. However, a detailed analysis proves this gradient does not have a significant effect upon the measured pressure. Heaters H2 and H3 are responsible for the cell temperature control. Figure 30 represents the implemented methodology for temperature control. The control scheme was implemented totally in LabView® 8.0. The data acquisition and control occured through a connector block SCB-68 and a data acquisition (DAQ) card PCI-6704 both from National Instrument (NI) Company. The computer uses and sends TTL (transistor-transistor-logic) signals through a PCI-DAQ card to control the on/off action of solid state relays (SSR) that control the heater. Figure 31 shows the control box.

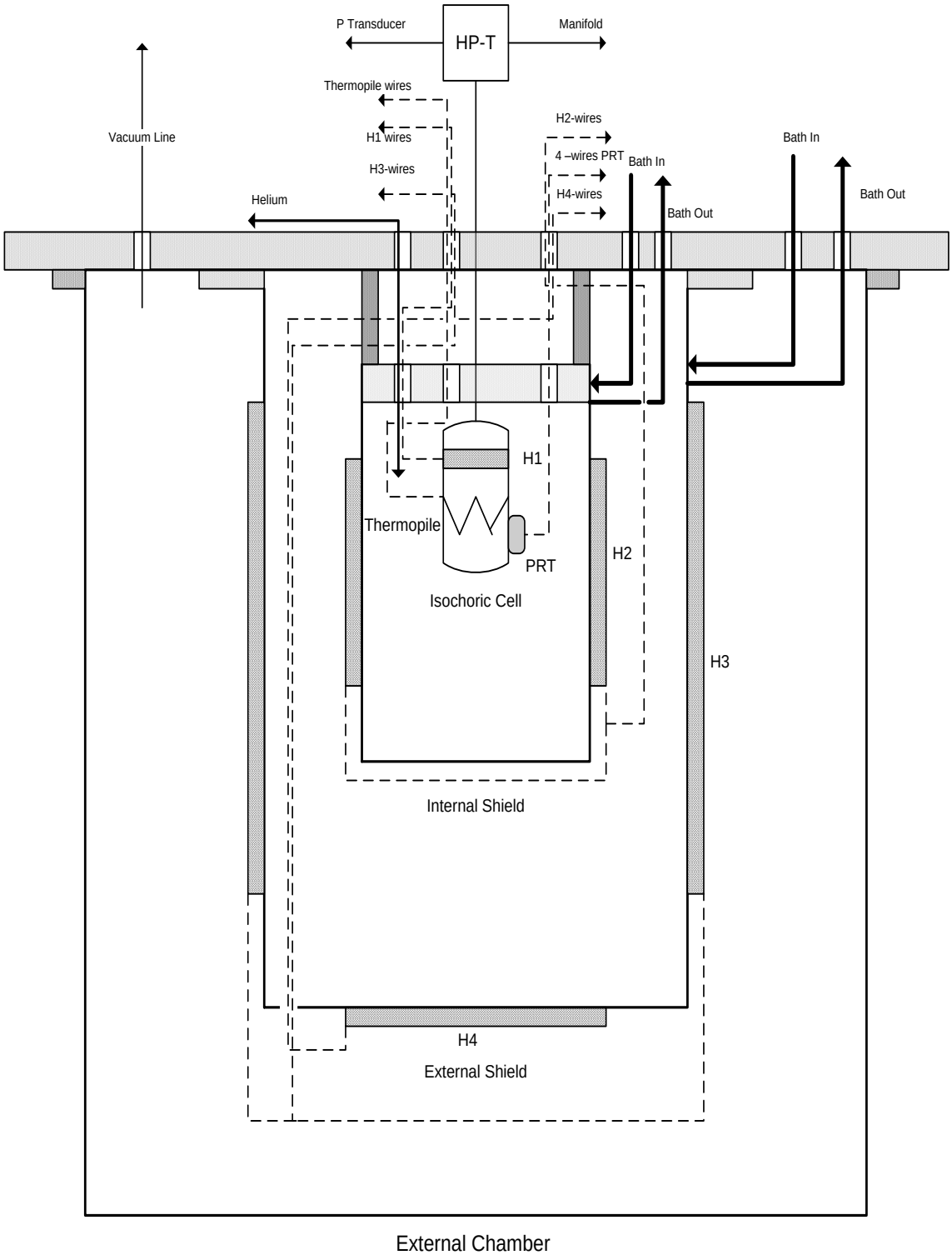

Figure 29. Isochoric apparatus cut view.

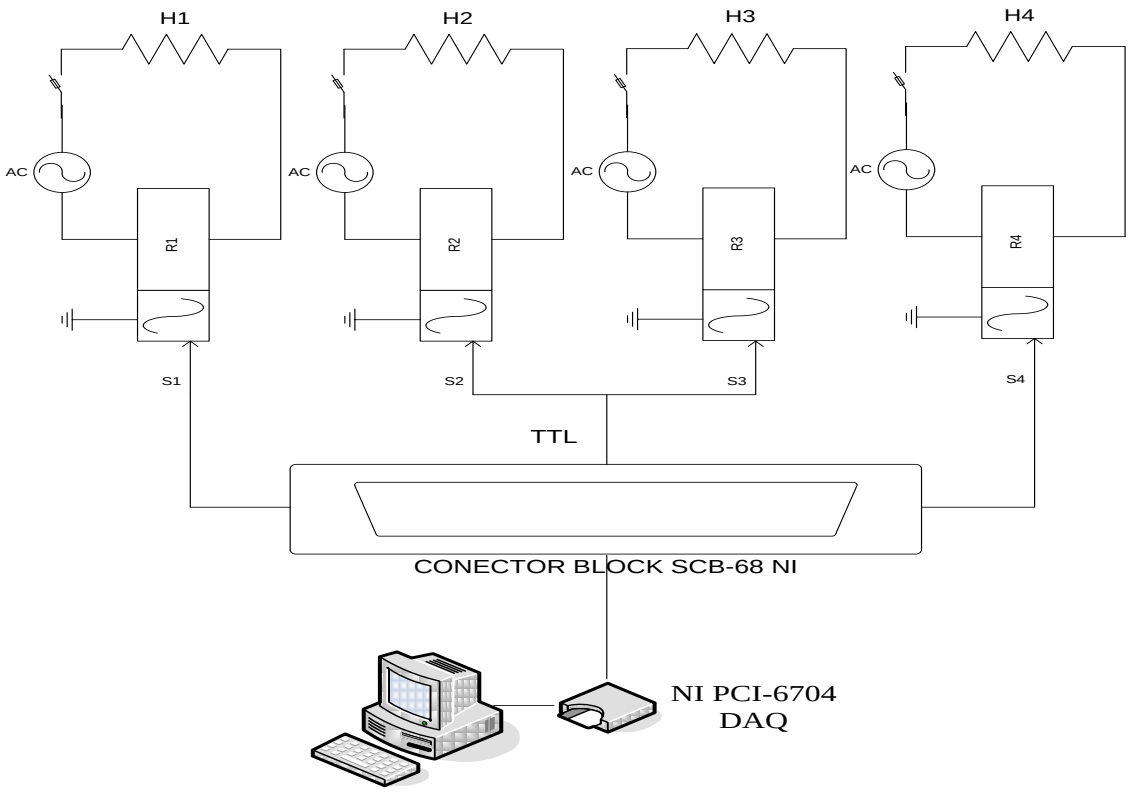

Figure 30. Temperature control methodology.

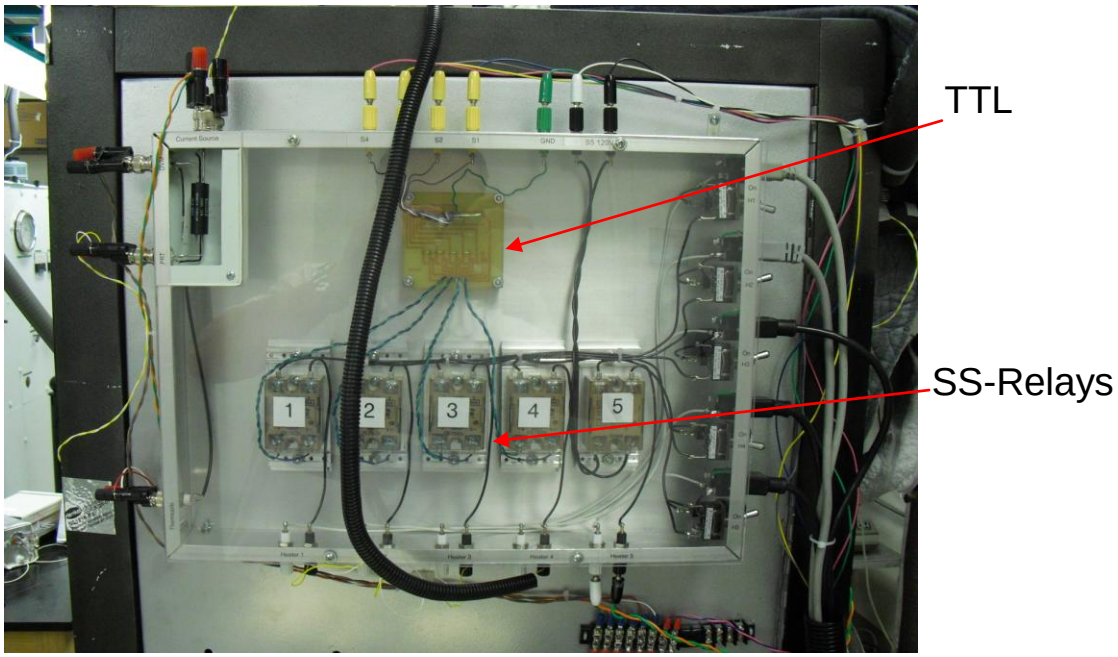

Figure 31. Control box set-up.

3.2.3 Phase Loop Determination Technique

A phase envelope is the pressure-temperature boundary for a mixture that separates its single-phase region from its two-phase region. Accurate phase envelope conditions have practical and theoretical uses. For example, the dew point of a natural gas mixture is important because liquid dropout can adversely affect flow measurement. It is also important to avoid heterogeneous flow in gas systems because liquids can damage compressors. A common practice is to operate the gas-gathering operation in the dense phase region above the cricondenbar, Melvin [81]. Accurate measurements are important to check the reliability of EoS. Hydrocarbon dew points in natural gas mixtures are important quality parameters stipulated in contracts and enforced throughout the supply chain.

Experimentally, it is possible to obtain dew or bubble points visually by observing the first appearance of a liquid drop or gas bubble in a vapor-liquid equilibrium cell. This procedure has large uncertainties near the critical point because the liquid and gas have identical properties. Also the procedure depends upon the visual skills of the experimenter. Industrially, a chilled mirror apparatus is popular because of speed and ease of use. However, sensitivity and repeatability depend upon the rate of mirror cooling and the flow rate of the fluid, Warner et al. [82]. Another method for obtaining the pressure-temperature conditions of the phase envelope is measuring pressure and temperature at constant density. Biswas and Ten Seldam [83] suggested this for pure fluids. Fluid isochores for mixtures at constant overall composition change slope on passing across the boundary. They are collinear only at the cricondentherm. Griffiths proved this behavior theoretically by as shown by Doiron et al. [84], and Rowlinson et al. [85] demonstrated the effect theoretically and experimentally.

Duarte-Garza et al. [76]determined the phase boundary by first fitting a linear or second order temperature function to the single-phase isochoric data and then fit another polynomial to the two-phase isochoric data. The intersection of these two functions determined the phase boundary. Later, Di Nicola et al. [86] used the same procedure, but employed quadratic polynomials in the single-phase region and an Antoine-type equation for the two-phase region. Zhou et al. [77]developed a procedure based upon the

residuals obtained from the fit of the temperature function to the single-phase isochoric data.

This work uses the changing slope at the phase envelope to obtain the temperature and pressure at the dew and bubble point. The method developed by Zhou et al. [77] is modified to improve the selection of the boundary point and to reduce the uncertainty in its determination. Different samples with fixed overall composition were tested and an uncertainty that depends upon the number of components was established.

3.2.3.1 Technique

The current technique fits a regression model to the experimental data. It assumes that the errors are uncorrelated random variables with mean zero and constant variance and that the errors have a normal distribution as suggested by Montgomery and Runger [87]. Because it is important that these assumptions be valid, we perform an analysis of the residuals to determine if the model requires additional terms. The following procedure provides the phase boundary pressure and temperature:

1. The isochoric experiment produces a set of data in the single-phase region and another in the two-phase region. As the data approach the phase boundary, it becomes difficult to determine if a point is in the single- or the two-phase region. To avoid omitting any point from the single-phase region, we fit a linear function to the experimental points that we are confident lie in the homogeneous region. If a systematic error appears in the residuals, we use a second-order function. Then, we add points, one-by-one, to the fitting procedure and analyze the residuals. After adding the first point of the heterogeneous region, the residuals exhibit a discontinuous jump. We exclude this point from the fit and retain the isochoric equation for the homogeneous region. The outliers are removed from the single phase by calculating standardized residuals with respect the fit. Nearly 95% of them should be in the interval (-2, +2) according to the assumption that the errors have a normal distribution (Montgomery and Runger [87]). The highest errors

occur near the cricondentherm because the discontinuous change in slope of an isochore is difficult to detect.

2. The pressure values at the experimental temperature of the single- and two-phase regions result from using the equation from step 1 and calculating the pressure residuals. These differences increase when crossing into the heterogeneous region as shown in Figure 32.
3. The residuals from the two-phase region are fit with a linear or second order polynomial. Rarely, a third order polynomial is necessary.
4. The temperature intercept is where the pressure residual is null. Figure 32 also shows the residuals and the polynomial passing through the residuals in the two-phase region. In the Zhou et al.[77] procedure, the intersection of the two equations determines the temperature. Their procedure can lead to higher errors in the temperature if the polynomial does not cross the zero line of the residual.
5. Finally, the pressure is estimated using the *P*-*T* polynomial obtained in step 1. This intercept belongs to phase loop, T_E, in Figure 33.
6. Because this is an isochoric experiment, the composition of the mixture is known from gravimetric construction.

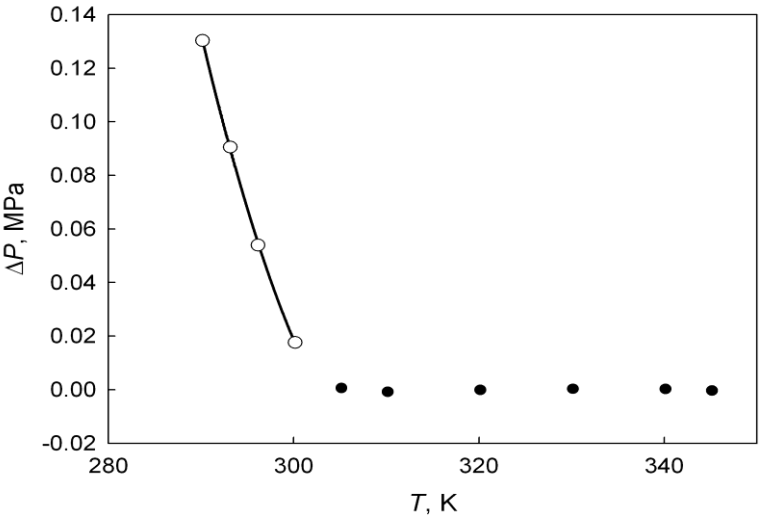

Figure 32. Pressure residuals in the single and two-phase region: Solid circles are single phase data and hollow circles are two-phase data.

Sometimes, outliers exist in the heterogeneous region (Figure 33 shows an example). The point is an outlier because lies outside the trend line.

Our procedure does not consider the correlation coefficient (R^2) as a condition of checking a change in slope. In general, a large value of R^2 does not imply a steep slope. In addition, it always increases if a variable is added to the model, but this does not necessarily mean that the new model is better than the old one.

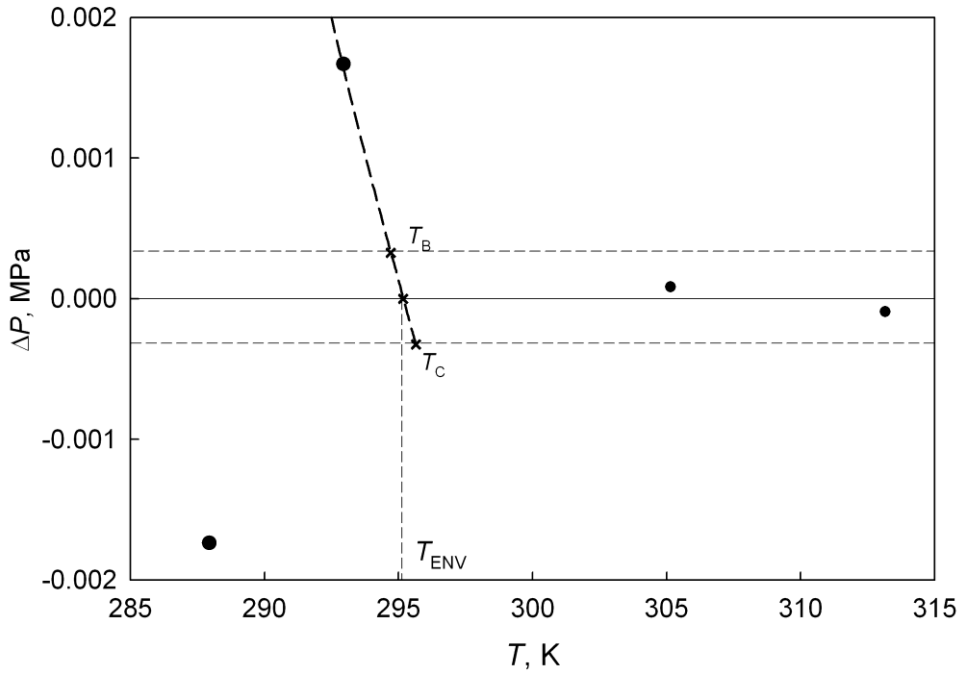

Figure 33. Interval errors for the pressure and temperature.

3.2.3.2 Uncertainties in Temperature and Pressure

The confidence interval for pressure and temperature to determine the error involved in the procedure is calculable. To obtain the standard deviation of the isochoric equation, we use the number of data points in the single-phase and the Student *t*, the uncertainty for pressure using a confidence level of 95%. The uncertainty for the pressure appears in Figure 33. The uncertainty bounds intercept the polynomial of the heterogeneous region residuals. Hence, two values for the temperature T_B and T_C are

obtained. The phase envelope temperature lies between them, and their difference is the temperature confidence interval. We use the largest temperature and pressure confidences for a given sample. The final value of the uncertainty for our procedure is the square-root of the sum of the quadratic pressure and temperature confidences, Figure 34.

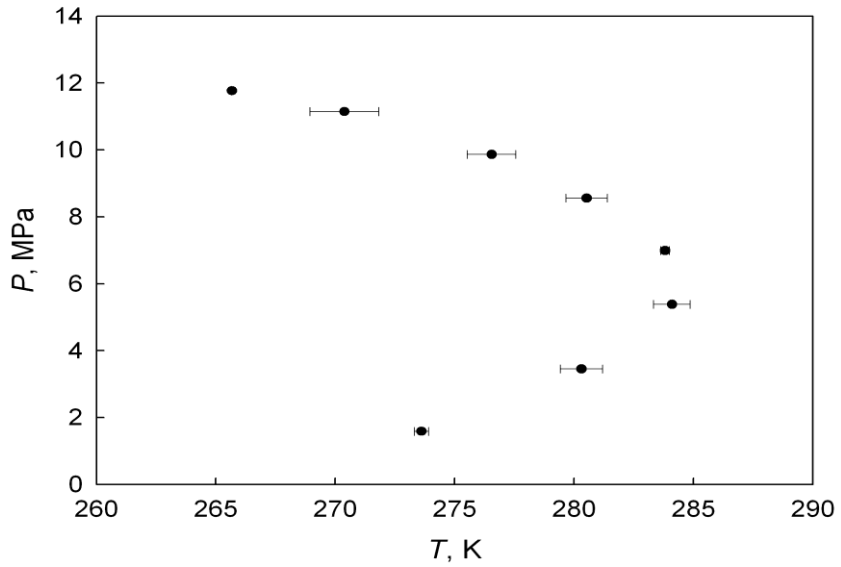

Figure 34. Phase envelope for a 7-component natural gas mixture near the criconderbar.

3.2.3.3 Results and Analysis

Mixtures with different numbers of components comprise the samples to calculate the dew and bubble temperatures and pressures. The results for some mixtures that appear in the literature are presented. The first example is an equimolar mixture of CO_2 + N_2. Duarte-Garza et al. [76] report the isochoric measurements for this mixture. The data consist of 19 isochores, but the last four isochores have only two points in the two-phase region. Consequently, it is not possible to apply the procedure for these data. Table 8 contains the calculated values for the phase boundary with the uncertainty at each point. The uncertainty is established at each point with this procedure along with an overall percentage deviation.

Table 10. Comparison Between Determined Boundary Pressures and Temperatures and Literature Values

P, MPa This work	σ_P	T, K This work	σ_T		P, MPa Ref. [76]	T, K Ref. [76]
$CO_2 + N_2$						
21.436	0.064	209.54	0.105		21.416	208.929
19.620	0.053	216.67	0.120		19.417	215.579
18.189	0.087	224.78	0.213		18.153	224.230
17.279	0.056	232.29	0.157		17.220	231.416
15.875	0.050	242.75	0.183		15.842	242.167
15.313	0.044	247.02	0.191		15.282	246.524
14.809	0.021	251.04	0.104		14.578	250.677
14.421	0.034	254.14	0.204		14.376	253.563
13.950	0.016	257.02	0.109		13.916	256.581
13.505	0.005	259.41	0.042		13.492	259.245
13.126	0.004	261.61	0.040		13.121	261.559
12.364	0.005	264.68	0.078		12.387	264.922
11.576	0.004	266.57	0.107		11.614	266.953
10.695	0.005	266.99	0.290		10.798	268.039
$CO_2 + N_2O$						
					Ref. [86]	Ref. [86]
3.0805	0.0015	272.368	0.029		3.076	272
2.0752	0.0024	257.523	0.054		2.072	257
2.1891	0.0008	258.785	0.018		2.187	259
2.8008	0.0013	267.194	0.025		2.797	267
2.4121	0.0010	261.381	0.020		2.413	261
0.9787	0.0004	233.168	0.017		0.981	233
3.8045	0.0012	278.092	0.017		3.788	278
3.3226	0.0015	272.452	0.027		3.319	272
1.3004	0.0008	240.645	0.023		1.301	241
2.8903	0.0013	267.060	0.024		2.885	267
4.1892	0.0013	280.992	0.020		4.185	281
2.6398	0.0017	263.310	0.020		2.635	263

The second example uses the data for CO_2 + N_2O from Di Nicola et al. [86]. After checking the standardized residuals, it appears that three points of the single-phase region could be outliers or belong to the two-phase region, specifically for the overall compositions 0.6099, 0.6953, and 0.9071. Including those values in the two-phase region does not result in deterioration of the curve-fit. Linear and quadratic functions represent attempts to fit the isochoric data in the single- and two-phase regions, but in all cases a quadratic polynomial is superior. Table 10 contains the results together with the values given by Di Nicola et al. [86]. They estimate uncertainties of ±1 kPa and ±0.3 K while our calculations indicate a maximum value of 2.4 kPa and 0.1 K.

The next example is a 7-component synthetic natural gas mixture measured in our laboratory. The accuracy of the temperature and pressure measurements is 0.01 K and 0.002 MPa. These small errors in pressure and temperature measurements are negligible in phase boundary determinations. In this mixture, straight lines represent the single-phase data. The region near the cricondenbar requires a second-order polynomial. In the two-phase region, selection of the order of the polynomial requires a different procedure. The order of the polynomial is increased until the difference between two consecutive, calculated phase boundary temperatures are within the uncertainty and no significant jump in the value occurs. This procedure requires care to avoid over-fitting the data. This particular mixture requires second and third order polynomials. The average deviation in the calculations of the phase boundary temperatures is 2σ = 1.3 K and the average percentage deviation of the pressure is 0.027%. This is the most complicated example examined because it is located in a narrow interval close to the cricondentherm $T > 0.93T_{\text{cricondenthem}}$. In this work, the percentage deviation is:

$$\%\,\text{deviation} = \frac{\Delta Y}{Y} \times 100 \qquad (3.2.3.3.1)$$

where ΔY is the uncertainty interval in the temperature or pressure and Y is the temperature or pressure at the phase boundary.

Figure 35 presents the phase envelope of a 22-component mixture [88]. The average deviation in the temperature is 2σ = 0.82 K. As seen in Figure 35, the closer the point is to the cricondentherm, the higher the uncertainty of the calculated temperature. Without the points near the cricondentherm, the value of 2σ drops to 0.3 K. The average percentage deviation in pressure is 0.022%. Here, second order polynomials and straight lines in the single- and two- phase regions represent the data.

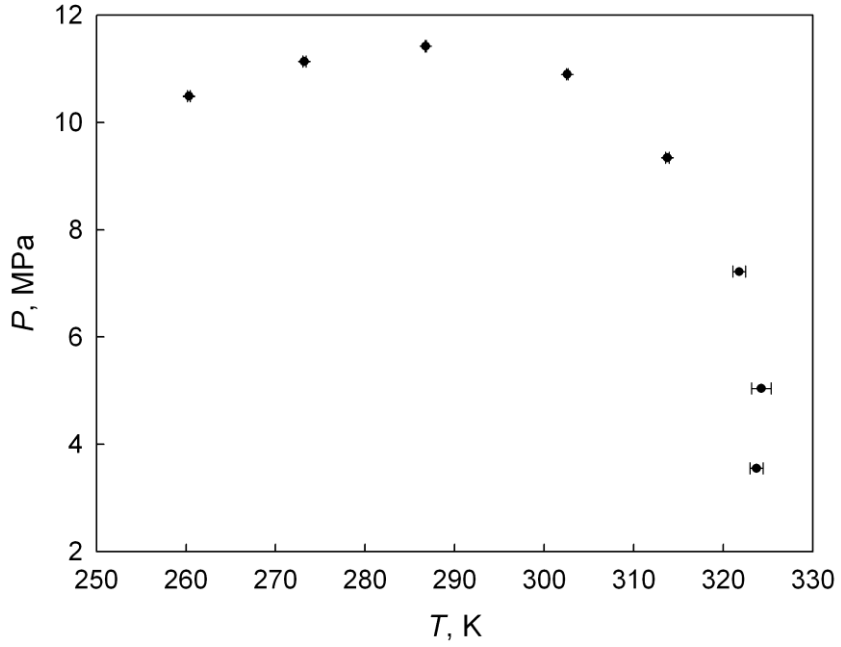

Figure 35. Phase envelope for a 22-component natural gas mixture.

Finally, Figures 36 and 37 present the percentage deviation of the temperature and pressure of all the multicomponent mixtures analyzed in this work. The pressure uncertainty increases near the cricondenbar (dP/dT = 0) and the temperature uncertainty increases near the cricondenthem (dT/dP = 0). The average percentage deviations for the temperature and pressure are 0.45% and 0.04%.

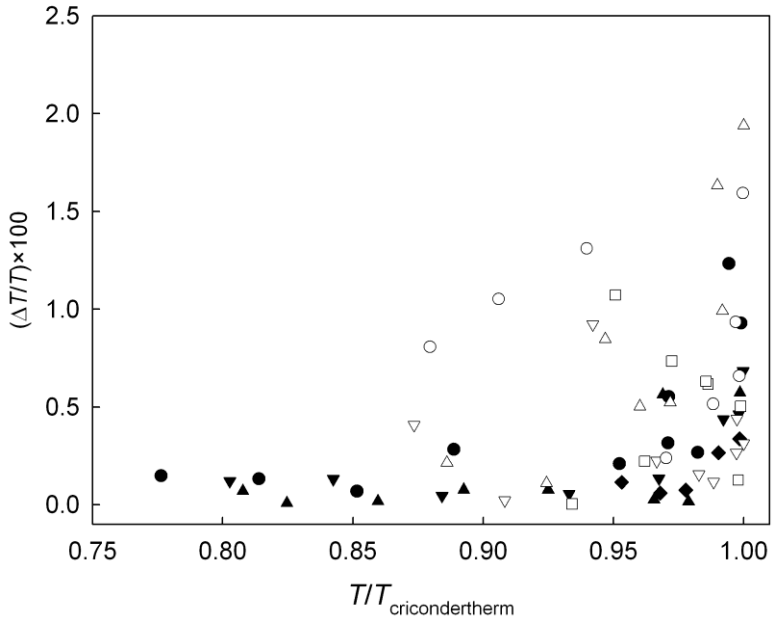

Figure 36. Percentage deviation of the phase boundary temperature. Natural gas mixtures. ○, 9-component; □, 7-component; △, 9-component; ▽, 9-component; ●, 14-component; ▲, 15-component; ▼, 22-component; ◆, $CH_4 + C_2H_6$.

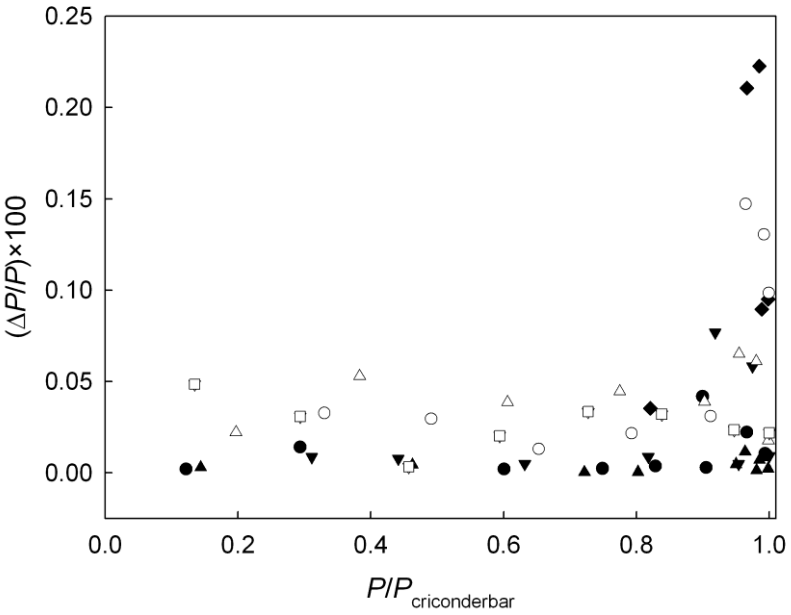

Figure 37. Percentage deviation in the calculation of the phase boundary pressure. Symbols description is the same as in Figure 36.

3.2.4 Saturated Density Determination and Isochoric Derivative Corrections

These two effects require compensation to determine the saturation density using isochoric data (actually, the "isochoric" data are isomolar) and phase boundaries. First, a volume change with temperature and pressure exists in the sample cell and in the transmission line between the isochoric cell and the pressure transducer. This effect can be correlated using the thermomechanical properties of both the gas cell and the transmission line materials:

$$\frac{V(T,P)}{V_{ref}(T_{ref},P_{ref})} = 1 + \beta(T - T_{ref}) + \kappa(P - P_{ref}) \qquad (3.2.4.1)$$

where β is the thermal expansion coefficient, κ is the pressure distortion parameter, and T_{ref} and P_{ref} are the reference temperature and pressure.

In addition, moles move between the sample cell and the transmission line during the experiment, and the phenomenon is a function of the pressure and the temperature in the sample cell and the transmission line. Figure 38 illustrates the apparatus. Compensation for this effect requires a model. The mole balance is

$$n_T = n_0 + n_{cell}, \qquad (3.2.4.2)$$

where n_T is the total number of moles, n_0 is the number of moles in the transmission line and n_{cell} is the number of moles in the cell. Now, substituting the real gas equation into Eq. 3.2.4.2

$$n_T = \frac{PV_0}{RT_0Z_0} + \frac{PV_{cell}}{RT_{cell}Z_{cell}} \qquad (3.2.4.3)$$

and using Eq. 3.2.3-1 for the volumes while considering the temperature of the transmission line is constant during the experiment, Eq. 3.2.4.3 becomes

$$n_T = \frac{P}{R}\left\{\frac{V_{ref}^0\left(1+\kappa_0(P-P_{ref})\right)}{T_0Z_0} + \frac{V_{ref}^{cell}\left(1+\alpha_{cell}(T-T_{ref})+\kappa_{cell}(P-P_{ref})\right)}{T_{cell}Z_{cell}}\right\} \qquad (3.2.4.4)$$

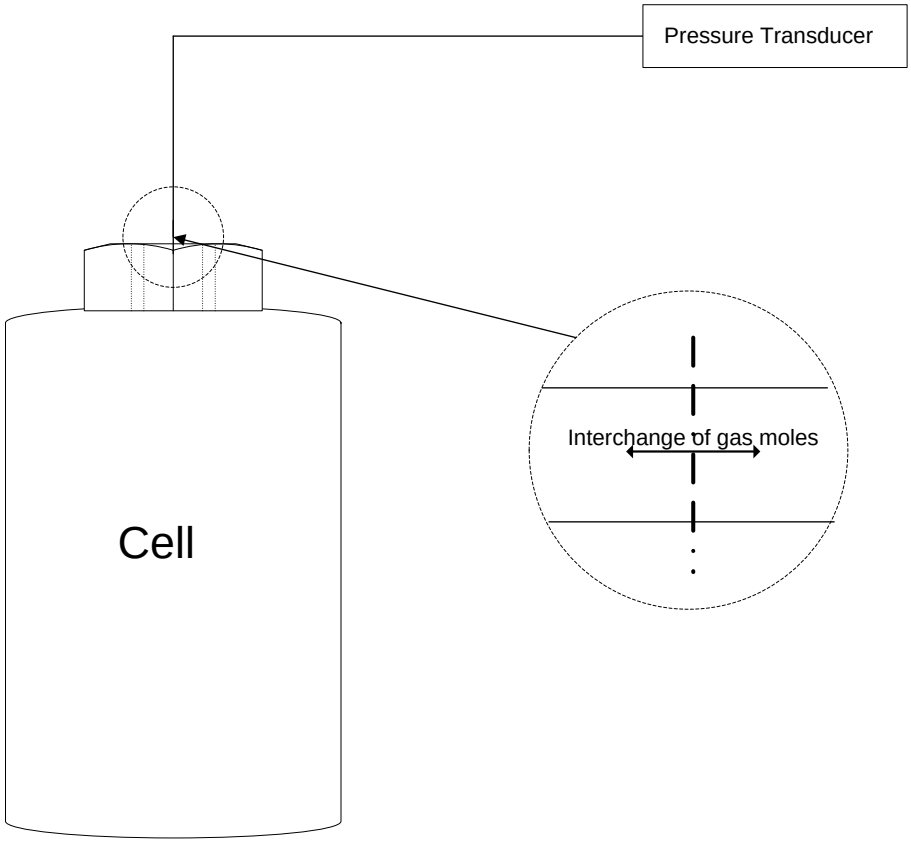

Figure 38. Schematic of the mass interchange in the low-pressure isochoric apparatus.

The unknown parameters in Eq. 3.2.4.4 are V_{ref}^{0}, V_{ref}^{cell} and n_T. The total number of moles n_T is different for each set of isochoric data. The *Z*-factor is available from the MSD $P\rho T$ data or any reliable EoS such as GERG-2004 [15]. The unknown parameters in Eq. 3.2.4.4 come from fitting the isochoric data. Table 11 contains the low-pressure and the high-pressure isochoric apparatuses parameters. The error introduced during this step corresponds to approximately 30 ppm in density. Determination of saturation densities (ρ') requires the number of moles in the cell as a function of temperature. Then extrapolation to the corresponding isochoric temperature provides the saturation value as shown in Figure 39.

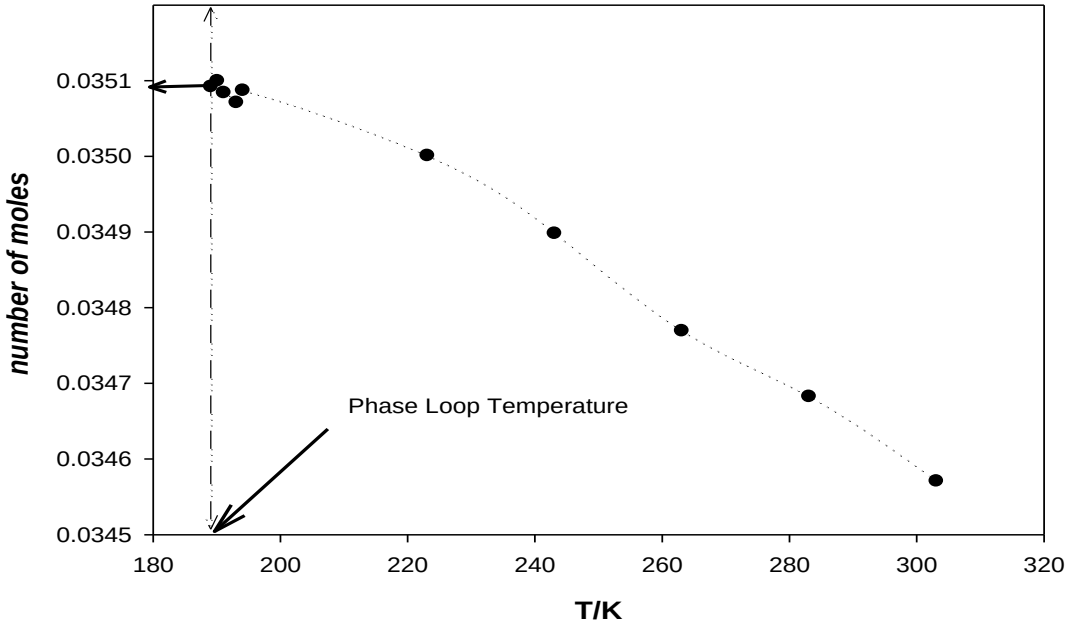

Figure 39. Methodology to determine the number of moles for calculating saturation densities.

Table 11. Low and High Pressure Isochoric Apparatus Parameters

Apparatus	Low Pressure	High Pressure
V_{ref}^{0} /m^3	1.55E-07	1.08E-05
V_{ref}^{cell} /m^3	6.08E-05	1.08E-08
κ_{cell} / MPa^{-1}	4.86E-05	1.60E-4
β_{cell}, β_0 /K^{-1}	2.53E-05	1.6E-4 /2.53E-05

Finally, with the number of moles in the cell corresponding to the phase boundary temperature and the volume of the cell, the saturation density is

$$\rho' = \frac{n'_{cell}}{V(T', P')} \tag{3.2.4.5}$$

where T' and P' are the phase boundary temperature and pressure. The estimated relative uncertainty for the saturation densities is 0.12%.

The isochoric derivative $\left(dP / dT\right)_\rho$ is necessary for thermal properties determination as illustrated by Eqs. 3.2.3-6 and 7

$$U\left(T,V_2\right) - U\left(T,V_1\right) = \int_{V_1}^{V_2} \left[T\left(\frac{\partial P}{\partial T}\right)_V - P \right] dV \tag{3.2.4.6}$$

$$S\left(T,V_2\right) - S\left(T,V_1\right) = \int_{V_1}^{V_2} \left(\frac{\partial P}{\partial T}\right)_V dV \tag{3.2.4.7}$$

Accurate determination of this derivative leads to accurate thermal data. To compensate for volume change and the mass interchange in the isochoric apparatus, the derivation for the derivative follows. The pressure in the sample cell is a function of temperature and density

$$P = P\left(T, \rho\right) \tag{3.2.4.8}$$

The differential of this function is

$$dP = \left(\frac{\partial P}{\partial T}\right)_\rho dT + \left(\frac{\partial P}{\partial \rho}\right)_T d\rho \tag{3.2.4.9}$$

Dividing both sides by *dT* and imposing the condition of the experiment

$$\left.\frac{dP}{dT}\right|_{\text{exp}} = \left(\frac{\partial P}{\partial T}\right)_\rho + \left(\frac{\partial P}{\partial \rho}\right)_T \left.\frac{d\rho}{dT}\right|_{\text{exp}} \tag{3.2.4.10}$$

where the left side of the equation is the derivative measured in the experiment. Then, the quantity required to evaluate the energy functions is

$$\left(\frac{\partial P}{\partial T}\right)_{\rho} = \left.\frac{dP}{dT}\right|_{\exp} - \left(\frac{\partial P}{\partial \rho}\right)_{T} \left.\frac{d\rho}{dT}\right|_{\exp} \tag{3.2.4.11}$$

The second term in this expression contains the contributions from the non-isochoric nature of the experiment. The density is related to the total volume of the cell, V_{cell}, and the number of moles of fluid in the cell, *n*, by

$$\rho = \frac{n}{V_{cell}} \quad \Rightarrow \quad \left.\frac{d\rho}{dT}\right|_{\exp} = \left(\frac{1}{V_{cell}}\right) \left.\frac{dn}{dT}\right|_{\exp} - \left(\frac{n}{V_{cell}}\right)\left(\frac{1}{V_{cell}}\right) \left.\frac{dV_{cell}}{dT}\right|_{\exp} \tag{3.2.4.12}$$

The first term contains changes that occur because of a noxious volume. A noxious volume is a portion of the sample container that is not at the same temperature as the measuring cell. The second term describes the changes that arise when the volume of the measuring cell varies with temperature and internal pressure.

Cell Volume Changes. The cell volume varies with both temperature and pressure, therefore

$$dV_{cell} = \left(\frac{\partial V_{cell}}{\partial T}\right)_{P} dT + \left(\frac{\partial V_{cell}}{\partial P}\right)_{T} dP \tag{3.2.4.13}$$

then

$$\left.\frac{dV_{cell}}{dT}\right|_{\exp} = V_{cell}\left(\beta_{cell} + \kappa_{cell} \left.\frac{dP}{dT}\right|_{\exp}\right) \tag{3.2.4.14}$$

where the thermal expansion and pressure distortion of the cell are

$$\text{Thermal expansion: } \beta_{cell} \equiv \frac{1}{V_{cell}}\left(\frac{\partial V_{cell}}{\partial T}\right)_{P} \tag{3.2.4.15}$$

$$\text{Pressure distortion: } \kappa_{cell} \equiv \frac{1}{V_{cell}}\left(\frac{\partial V_{cell}}{\partial P}\right)_{T} \tag{3.2.4.16}$$

The numerical values of the thermal expansion and pressure distortion of the cell come from the materials of construction and the geometry of the cell design, and

$$\left.\frac{d\rho}{dT}\right|_{\exp} = \left(\frac{1}{V_{cell}}\right)\left.\frac{dn}{dT}\right|_{\exp} - \rho\left(\beta_{cell} + \kappa_{cell}\left.\frac{dP}{dT}\right|_{\exp}\right) \tag{3.2.4.17}$$

Noxious Volume Effects. If a portion of the volume containing the sample is at a fixed temperature (in a pressure transducer, for example), then

$$n + n_0 = \text{constant} \quad \Rightarrow \quad dn = -dn_0 \tag{3.2.4.18}$$

where the subscript 0 denotes values for the noxious volume. Then

$$\left.\frac{dn}{dT}\right|_{\exp} = -\left.\frac{dn_0}{dT}\right|_{\exp} \qquad \text{where} \qquad n_0 = \rho_0 V_0 \tag{3.2.4.19}$$

Here, ρ_0 is the density in the noxious volume, and V_0 is the total volume of the noxious volume. Then

$$\left.\frac{dn_0}{dT}\right|_{\exp} = \rho_0 \left.\frac{dV_0}{dT}\right|_{\exp} + V_0 \left.\frac{d\rho_0}{dT}\right|_{\exp} \tag{3.2.4.20}$$

The first term in this equation describes the contribution from changes in the noxious volume during the experiment, and the second term describes effects that arise from the *P-V-T* behavior of the fluid in the noxious volume.

Noxious Volume Changes. For the noxious volume

$$dV_0 = \left(\frac{\partial V_0}{\partial T_0}\right)_P dT_0 + \left(\frac{\partial V_0}{\partial P}\right)_{T_0} dP_0 \tag{3.2.4.21}$$

The noxious volume and measuring volume have direct connection, therefore

$$P = P_0 \quad \Rightarrow \quad dP = dP_0 \tag{3.2.4.22}$$

Dividing by *dT* and imposing the experimental conditions

$$\left.\frac{dV_0}{dT}\right|_{\exp} = \left(\frac{\partial V_0}{\partial T_0}\right)_P \left.\frac{dT_0}{dT}\right|_{\exp} + \left(\frac{\partial V_0}{\partial P}\right)_{T_0} \left.\frac{dP}{dT}\right|_{\exp} = \beta_0 V_0 \left.\frac{dT_0}{dT}\right|_{\exp} + \kappa_0 V_0 \left.\frac{dP}{dT}\right|_{\exp} \quad (3.2.4.23)$$

where the thermal expansion and pressure distortion for the noxious volume are analogous to those for the measuring cell

$$\text{Thermal expansion: } \beta_0 \equiv \frac{1}{V_0}\left(\frac{\partial V_0}{\partial T}\right)_P \quad (3.2.4.24)$$

$$\text{Pressure distortion: } \kappa_0 \equiv \frac{1}{V_0}\left(\frac{\partial V_0}{\partial P}\right)_T \quad (3.2.4.25)$$

If the noxious volume is constant, then

$$\left.\frac{dT_0}{dT}\right|_{\exp} = 0 \quad (3.2.4.26)$$

and

$$\left.\frac{dV_0}{dT}\right|_{\exp} = \kappa_0 V_0 \left.\frac{dP}{dT}\right|_{\exp} \quad (3.2.4.27)$$

Fluid P-V-T Effects. Writing the fluid density as a function of temperature and pressure

$$d\rho_0 = \left(\frac{\partial \rho_0}{\partial T_0}\right)_P dT_0 + \left(\frac{\partial \rho_0}{\partial P}\right)_{T_0} dP \quad (3.2.4.28)$$

and, as for the previous case,

$$\begin{aligned}\left.\frac{d\rho_0}{dT}\right|_{\exp} &= \left(\frac{\partial \rho_0}{\partial T_0}\right)_P \left.\frac{dT_0}{dT}\right|_{\exp} + \left(\frac{\partial \rho_0}{\partial P}\right)_{T_0} \left.\frac{dP}{dT}\right|_{\exp} = 0 + \left(\frac{\partial \rho_0}{\partial P}\right)_{T_0} \left.\frac{dP}{dT}\right|_{\exp} \\ &= \left(\frac{\partial \rho_0}{\partial P}\right)_{T_0} \left.\frac{dP}{dT}\right|_{\exp}\end{aligned} \quad (3.2.4.29)$$

Combined Effects. Collecting the noxious volume results gives

$$\left.\frac{dn_0}{dT}\right|_{\exp} = \rho_0 V_0 \kappa_0 \left.\frac{dP}{dT}\right|_{\exp} + V_0 \left(\frac{\partial \rho_0}{\partial P}\right)_{T_0} \left.\frac{dP}{dT}\right|_{\exp} = V_0 \left(\rho_0 \kappa_0 + \left(\frac{\partial \rho_0}{\partial P}\right)_{T_0} \right) \left.\frac{dP}{dT}\right|_{\exp} \quad (3.2.4.30)$$

and

$$\begin{aligned} \left.\frac{d\rho}{dT}\right|_{\exp} &= -\frac{V_0}{V_{cell}} \left(\rho_0 \kappa_0 + \left(\frac{\partial \rho_0}{\partial P}\right)_{T_0} \right) \left.\frac{dP}{dT}\right|_{\exp} - \rho \left(\beta_{cell} + \kappa_{cell} \left.\frac{dP}{dT}\right|_{\exp} \right) \\ &= -\rho \beta_{cell} - \left[\rho \kappa_{cell} + \gamma \left(\rho_0 \kappa_0 + \left(\frac{\partial \rho_0}{\partial P}\right)_{T_0} \right) \right] \left.\frac{dP}{dT}\right|_{\exp} \end{aligned} \quad (3.2.4.31)$$

Combining the measuring cell and noxious volume results

$$\begin{aligned} \left(\frac{\partial P}{\partial T}\right)_{\rho} &= \left.\frac{dP}{dT}\right|_{\exp} - \left\{ -\rho \beta_{cell} - \left[\rho \kappa_{cell} + \gamma \left(\rho_0 \kappa_0 + \left(\frac{\partial \rho_0}{\partial P}\right)_{T_0} \right) \right] \left.\frac{dP}{dT}\right|_{\exp} \right\} \left(\frac{\partial P}{\partial \rho}\right)_T \\ &= \left.\frac{dP}{dT}\right|_{\exp} + \left(\frac{\partial P}{\partial \rho}\right)_T \left\{ \rho \beta_{cell} + \left[\gamma \left(\frac{\partial \rho_0}{\partial P}\right)_{T_0} + \rho \kappa_{cell} + \gamma \rho_0 \kappa_0 \right] \left.\frac{dP}{dT}\right|_{\exp} \right\} \end{aligned} \quad (3.2.4.32)$$

Rearranging Eq. 3.2.4.32:

$$\begin{aligned} \left(\frac{\partial P}{\partial T}\right)_{\rho} &= \left.\frac{dP}{dT}\right|_{\exp} + P \frac{\rho}{P} \left(\frac{\partial P}{\partial \rho}\right)_T \left\{ \beta_{cell} + \left[\frac{\gamma}{\rho} \left(\frac{\partial \rho_0}{\partial P}\right)_{T_0} + \kappa_{cell} + \gamma \kappa_0 \frac{\rho_0}{\rho} \right] \left.\frac{dP}{dT}\right|_{\exp} \right\} \\ &= \left.\frac{dP}{dT}\right|_{\exp} + P \left(\frac{\partial \ln P}{\partial \ln \rho}\right)_T \left\{ \beta_{cell} + \left[\frac{\gamma}{\rho} \left(\frac{\partial \rho_0}{\partial P}\right)_{T_0} + \kappa_{cell} + \gamma \kappa_0 \frac{\rho_0}{\rho} \right] \left.\frac{dP}{dT}\right|_{\exp} \right\} \end{aligned} \quad (3.2.4.33)$$

Eq. 3.2.4.33 provides the correction to the experimental isochoric derivatives and allows the determination of caloric properties more accurately.

3.3 Composition Data

In order to establish the actual coordinates into the thermodynamics space for a specific state of a fluid requires the composition. This fact is the most important and difficult task when determining mixtures properties. Composition is the major source of error and uncertainty in the specification of natural gas properties. In fact, it contributes around 75% with of the total 2σ uncertainty in the determination of natural gas densities, Figure 40.

Therefore special emphasis has been given to the determination of the natural gas mixtures composition, which is usually done by gas chromatography (GC). In its final report in 2003, "Preparation of Natural Gas Blends Used as Calibration Standards: Sources of Uncertainty and Best Preparation Practices", the Southwest Research Institute® provides an important analysis of the influence of natural gas composition in the determination of natural gas price during custody transfer [89]. Two hypothetic scenarios were evaluated to examine the effect of GC accuracy on the computed heating values:

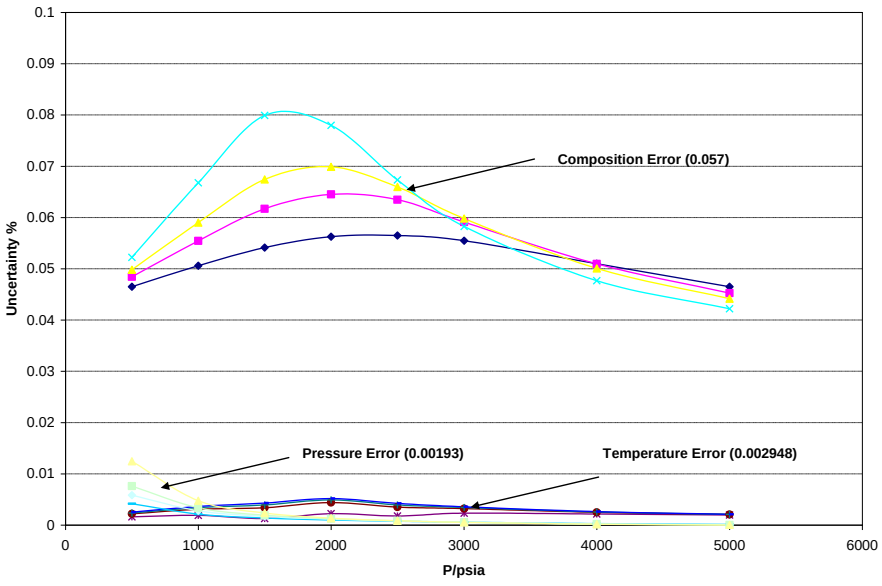

Figure 40. Temperature, pressure and composition contribution to the total density uncertainty for a synthetic natural gas mixture at 1σ.

1. A simulated error in the analytical hexane content of ± 0.1% for a 1050 Btu/scf gas. The other components were renormalized proportionately to return the total 100 mol%.
2. The modification of the original composition to simulate errors of ± 0.1% into a lumped C_{6+} fraction.

The two evaluated examples lead to errors in the heating value of up to -4.27 Btu/scf, or -0.4% that corresponds to an error of $584,000 per year for a pipeline gas flowing at 100 MMSCFD. The report concludes that: "Large uncertainties in the heavier components introduce the potential for errors in GC calibration, specifically by biasing the computed response factor for those components" [89]. Additionally, the report notes that few certified gas standards were available that contained ppm levels of C_9 and heavier components.

Based upon the relevance of the mixture composition in the determination of accurate thermodynamics properties, this project proposes an alternative methodology. The fundamental idea is to take advantage of the high accuracy GC analysis for key compounds in the gas mixtures and propagate it to the heavy hydrocarbons via Coherent Anti-Stoke Raman Scattering (CARS).

3.3.1 Coherent Anti-Stokes Raman Scattering (CARS)

Since 1928, when Raman found that a substance irradiated with light of a certain frequency scatters not only light with the same frequency of the incident beam but also lines with lower (Stokes) and higher (anti-Stokes) frequencies, the use of the Raman spectrum has become an important tool for characterizing molecular structure of materials [90].

Recently, Pestov et al. [91] have developed a hybrid technique to enhance the efficiency of the Raman scattering process caused by the broadband preparation with an order of 10^5 compared to former techniques. Figure 41 illustrates the general principle of this technique.

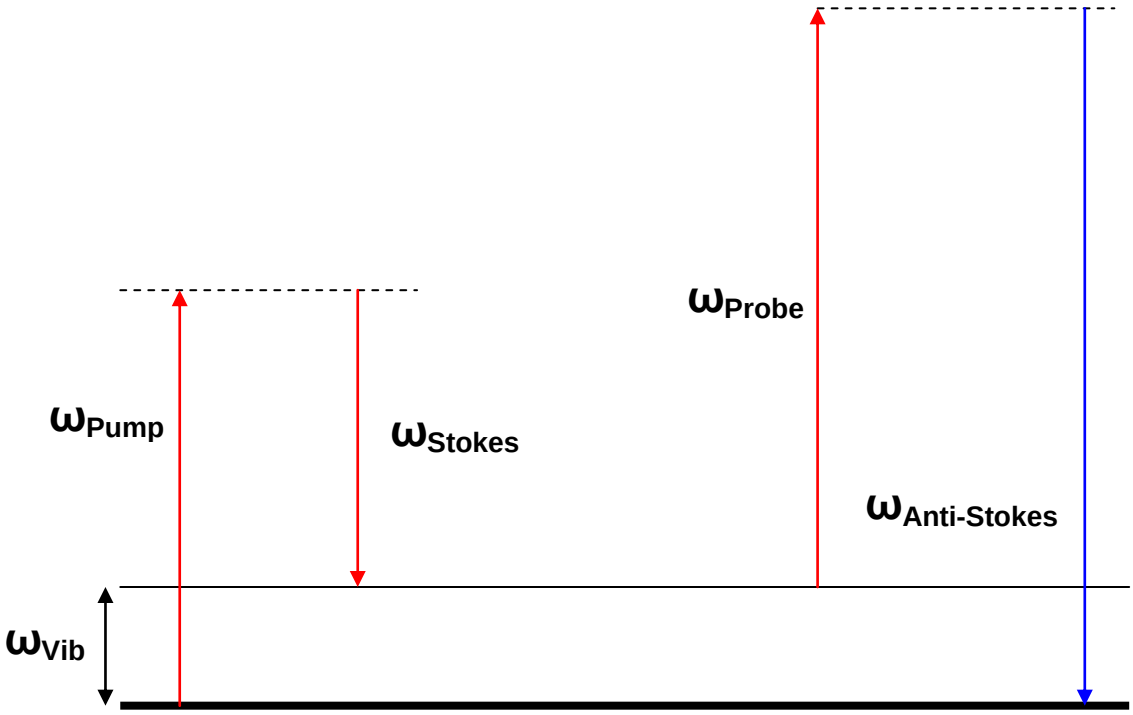

Figure 41. CARS energy scheme.

The coherent anti-stokes Raman scattering technique is based upon the irradiation of a sample with two coherent laser beams (pump and stokes) that generate a resonant state between the ground state and the vibrational state of the molecules in the sample; then a third laser beam (probe beam) is used to scatter off an additional blue-shift high frequency signal $(\omega_{Pump} - \omega_{Stokes}) + \omega_{Probe}$ (anti-stokes). Essentially, this new technique uses the shifting of the probe beam to minimize the non-resonant (NR) four-wave mixing (FWM) signal from other molecules. Therefore, using the ratios between the Raman lines in the normalized background-free CARS spectra can provide real-time monitoring of gas composition.

In order to evaluate the performance of this new approach determining natural gas mixture compositions using CARS, a high pressure gas chamber has been designed and built. The characteristics of the gas chamber appear in the Table 12 and in Figure

42. The gas cell needed to work at high-pressure to improve the signal intensity in the spectrogram.

Table 12. CARS Gas Chamber Characteristics

Material:Ultra-Violet quality synthetic fused silica.
Refractive index: 1.46 @500nm
Surface flatness: 1/10
Parallelism: ≤5arcsec or 3arcmin
Pressures up to 1000 psia

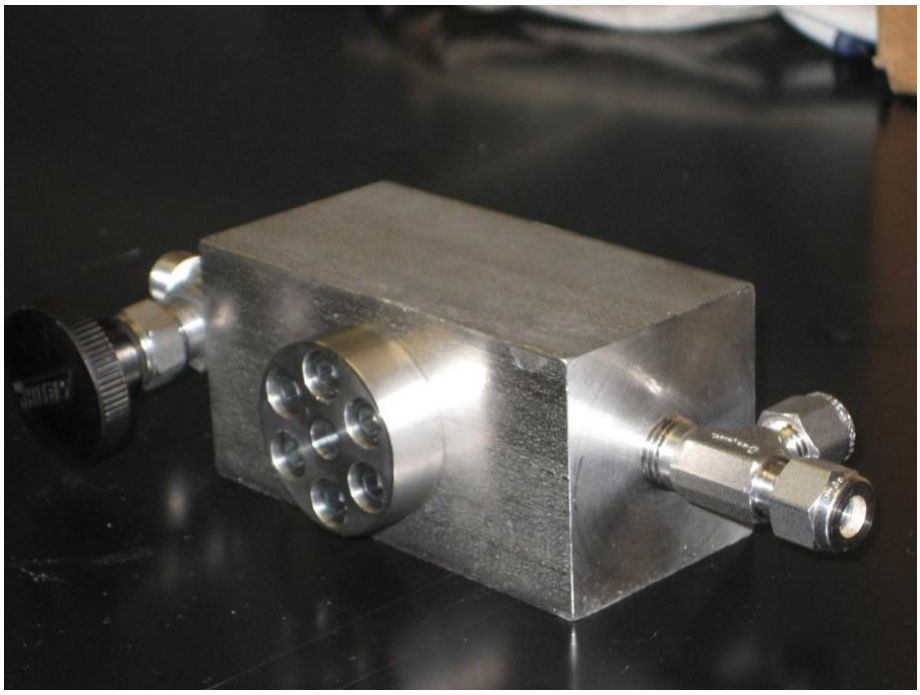

Figure 42. CARS gas chamber.

This preliminary evaluation was performed in cooperation with the quantum optics group and the thermodynamics research group at Texas A&M University. The schematic for the Raman technique is Figure 43.

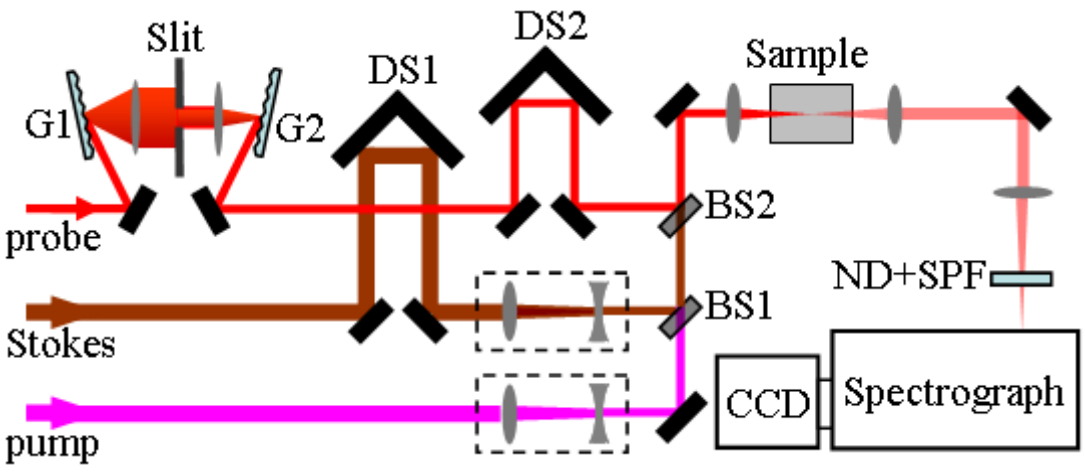

Figure 43. Setup schematics. G1,2, gratings; DS1,2, delay stages; BS1,2, beam splitters, ND+SPF, a set of neutral density and shortpass filters; CCD, charge-coupled device [92].

The test was performed with a gravimetrically prepared sample, at room temperature and pressure. The background-free CARS spectra were determined by tuning the probe signal. The CARS spectrogram appears in Figure 44. The normalized spectra and the gas composition are Figure 45. A remarkable base line results for the normalized spectra in Figure 45. This result leads to the hypothesis of using the "ratio-method"[93] coupled with GC analysis to minimize the uncertainty of composition determination for natural gas mixtures.

The proposed methodology is: first, characterize some key compound using GC analysis. Uncertainties of less than 0.04% are achievable for these key compounds (methane, carbon dioxide, etc). Then at the beginning of sampling, the compositions for these key compounds must be determined via GC analysis. Second, the CARS analysis must be performed at constant temperature and pressure. Here, an accurate control of these variables is necessary because of the strong interdependency of the signal intensity,

temperature and pressure. Finally, based upon the composition of the key compound and the spectra information, the composition of the unknown compounds can be determined using the "ratio-method" from the correlation between the gas compositions, the area of the bands $A_{x(\nu_x)}$ at frequencies ν_x and the relative normalized differential Raman scattering (RNDRS) cross sections (Eq 3.3.1.1). From Eq. 1, a direct propagation of the low uncertainty of the key compounds compositions from GC can be expected.

$$\frac{C_x}{C_{methane}} = \frac{A_{x(\nu_x)} \cdot \sum_{methane(\nu_l)}}{A_{methane(\nu_l)} \cdot \sum_{x(\nu x)}} \qquad (3.3.1.1)$$

Raman spectroscopy has been used in the past for the determination of natural gas compositions. However, the characteristics of the precedent studies [93-95] were not as good as the new methodology for CARS developed by Pestov et al. [92]. Uncertainties of 0.002 in the mole fraction were obtained in the past, while the new methodology should achieve uncertainties less than 0.0005 in the mole fraction for the long chain and low composition compounds present in natural gas mixtures.

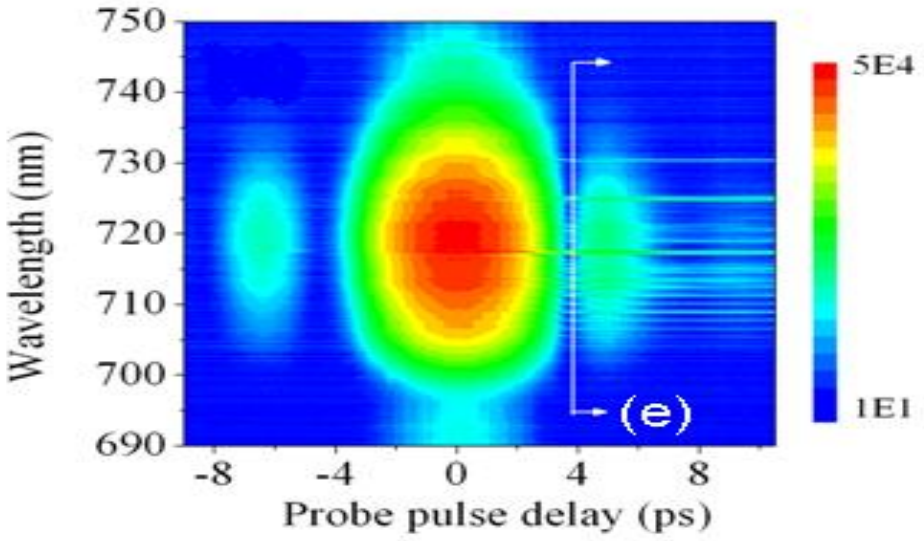

Figure 44. CARS spectrogram.

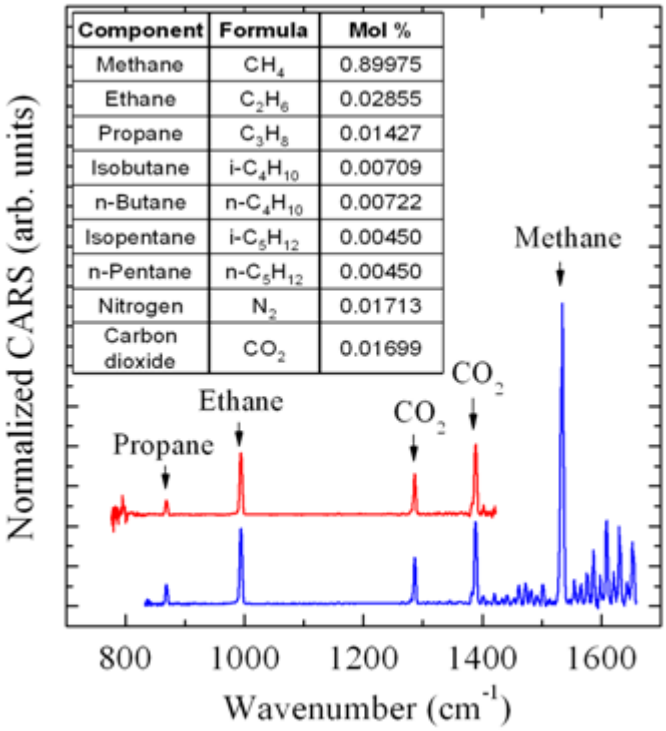

Figure 45. CARS spectra normalized on the reference FWM profiles.

EXPERIMENTAL RESULTS FOR SYNTHETIC NATURAL GAS MIXTURES

After the development and improvement of all the necessary apparatus and methodologies for the isothermal densimeter and the isochoric apparatus, new measurements for natural gas mixtures were collected and old measurements were corrected and used to determine additional properties such us the saturation densities. The following analysis focuses upon the measurement of a new, ternary natural gas sample and the correction of density and isochoric data of four synthetic natural mixtures.

4.1 Ternary $P\rho T$ Data

Residual or pipeline natural gas is the principal product of a natural gas processing plant. Its importance as an energy source for industrial process, residential and commercial uses, transportation and generation of electric power is unquestionable[3]. Although its composition is variable, a ternary mixture of methane, ethane and propane is a suitable surrogate. Accurate characterization of such mixtures has been a fundamental research problem for many years[15, 96]. Accurate $P\rho T$ data combined with experimental phase boundaries are necessary to develop and validate reference EoS. The formulation of highly accurate EoS for mixtures is an important research topic that depends upon the reliability of experimental data[97].

During the past twenty years, new reference EoS for the main compounds of natural gas have appeared[5-9]. Recently, the Thermodynamics Laboratory at Texas A&M University has produced new, highly-accurate data at high pressure for methane[98], ethane[99], nitrogen[100] and carbon dioxide[101] using a magnetic-suspension, single-sinker densimeter. These data have demonstrated that the fundamental EoS used as reference standards for these compounds [26] behaves well at high pressure. This is apparent in the preceeding chapter. This work presents new $P\rho T$ data for a residual natural gas sample as part of a systematic study to validate and support natural gas standard EoS such as AGA8 DC92[102] and GERG-2004[15] at high pressure.

In addition, equilibrium data have been measured with the low-pressure isochoric apparatus. The results are compared to the Peng-Robinson[21] EoS, which is commonly used in industry for phase equilibrium calculations using a phase behavior simulator developed in the Laboratory. Finally, the new methodology to predict saturation densities using isochoric data and to correct isochoric derivatives is applied.

4.1.1 Experimental

Isothermal density data for a ternary mixture at (300, 350 and 400) K up to 200 MPa as well as isochoric and equilibrium data were measured. The ternary mixture came from DCG PARTNERSHIP Inc. having a molar composition of 95.039 % methane, 3.961 % ethane and 1.000 % propane with ± 0.037% estimated gravimetric uncertainty (NIST traceable by weight). The characteristics of the MSD and the isochoric apparatuses appeared in the third chapter.

4.1.2 Results and Analysis

The density data for the sample and their comparisons to GERG-2004 and AGA8-DC2 predictions (implemented in RefProp 8.0,[26]) appear in Table 13, and the deviations are in Figure 46. This figure indicates that GERG-2004 has better predictive capability across the range of pressure than AGA8-DC2. GERG-2004 predicts density data with a relative deviation of approximately 0.02% up to 170 MPa. This result is consistent with those found previously for pure component density data at high pressure [98-99]. Therefore, it appears that the approach developed by different authors recently[15, 97] to construct multiparameter EoS can predict high-pressure density data with excellent accuracy, at least up to 200 MPa. AGA8-DC2 has a relative deviation of 0.04% across the pressure range. Using the procedure described by Cristancho et al. [98] provides the second and the third virial coefficients, which appear in Table 14. The estimated absolute uncertainty for the second and the third virial coefficients are 0.57 $cm^3 \cdot mol^{-1}$ and 125 $(cm^3 \cdot mol^{-1})^2$ respectively.

The procedure using isochoric data to determine the phase boundaries was described in Chapter 3 and represented in Figure 47. The predicted phase envelope that appears in Figure 48 is a calculation using the Peng-Robinson equation with binary interaction parameters determined from equilibrium data for natural gas mixtures in Table 15. The equation predictions follow the trend of the experimental data, but they have higher deviations approaching the cricondenbar.

Table 13. Density Values

P/MPa	ρ/ kg· m^{-3}	ρ/ kg· m^{-3} (GERG-2004)	ρ/ kg· m^{-3} (AGA8-DC2)	$100\cdot(\rho-\rho_{GERG})/\rho$	$100\cdot(\rho-\rho_{AGA8-DC2})/\rho$
		T=300.000 K			
4.965	36.976	36.988	36.991	-0.032	-0.040
5.998	45.559	45.570	45.574	-0.023	-0.032
6.994	54.107	54.122	54.125	-0.027	-0.032
8.002	63.008	63.024	63.028	-0.025	-0.032
9.998	81.252	81.275	81.278	-0.028	-0.032
12.427	103.999	104.020	104.030	-0.020	-0.029
14.992	127.615	127.640	127.640	-0.019	-0.019
20.017	168.796	168.810	168.780	-0.008	0.009
25.012	200.944	200.940	200.910	0.002	0.017
30.021	225.761	225.740	225.710	0.009	0.023
44.944	274.513	274.470	274.350	0.016	0.059
49.920	285.997	285.970	285.820	0.010	0.062
50.254	286.701	286.680	286.540	0.007	0.056
		T=350.000 K			
2.002	11.854	11.857	11.857	-0.024	-0.024
4.998	30.447	30.452	30.455	-0.017	-0.027
10.001	63.246	63.251	63.263	-0.007	-0.026

Table 13. Continued

***P*/MPa**	***ρ*/ kg· m^{-3}**	***ρ*/ kg· m^{-3} (GERG-2004)**	***ρ*/ kg· m^{-3} (AGA8-DC2)**	**$100\cdot(\rho-\rho_{GERG})/\rho$**	**$100\cdot(\rho-\rho_{AGA8-DC2})/\rho$**
19.987	128.080	128.070	128.090	0.008	-0.008
30.019	180.470	180.460	180.410	0.006	0.033
39.996	218.303	218.300	218.280	0.001	0.011
49.953	246.399	246.350	246.320	0.020	0.032
69.915	286.052	286.050	285.960	0.001	0.032
79.946	301.044	301.060	300.940	-0.005	0.035
99.921	325.172	325.190	325.060	-0.006	0.034
119.976	344.390	344.400	344.270	-0.003	0.035
139.909	360.259	360.240	360.150	0.005	0.030
149.927	367.348	367.310	367.240	0.010	0.030
169.848	380.063	379.990	379.970	0.019	0.025
		T=400.000 K			
4.999	25.994	25.993	25.996	0.003	-0.008
10.004	52.804	52.802	52.814	0.003	-0.019
19.992	104.944	104.920	104.960	0.023	-0.015
30.035	150.199	150.170	150.170	0.019	0.019
40.009	186.143	186.130	186.090	0.007	0.028
49.929	214.526	214.470	214.450	0.026	0.035
59.959	237.631	237.590	237.600	0.017	0.013
69.948	256.657	256.640	256.640	0.006	0.006
79.919	272.755	272.750	272.740	0.002	0.005
89.963	286.787	286.790	286.760	-0.001	0.009
99.971	299.071	299.080	299.030	-0.003	0.014
119.622	319.587	319.580	319.510	0.002	0.024
139.783	337.056	337.020	336.940	0.011	0.035

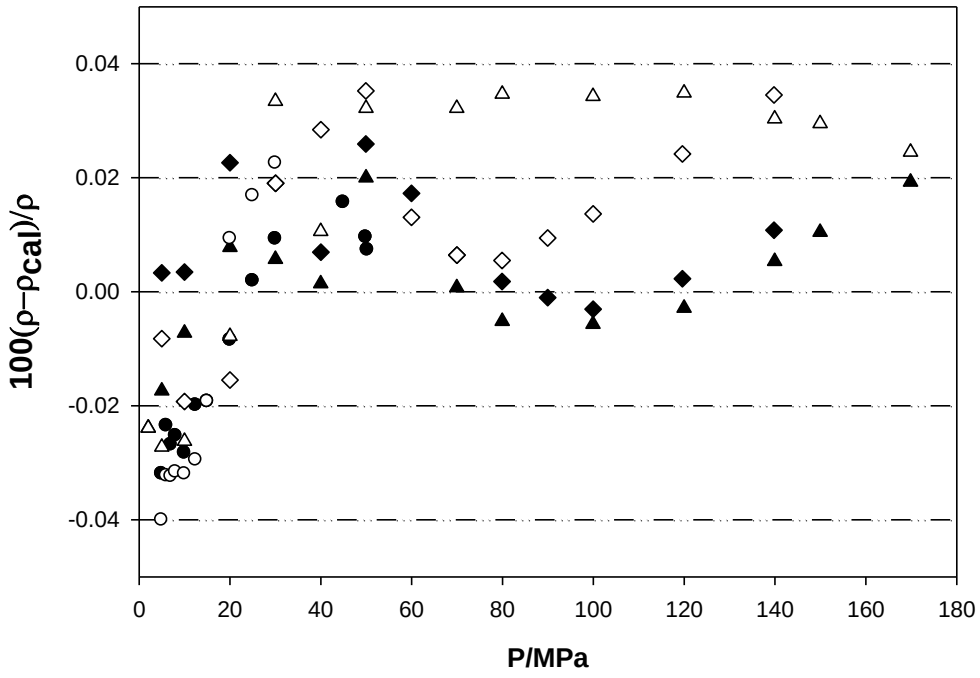

Figure 46. Percentage deviations of the experimental $P\rho T$ data from values calculated using the GERG-2004 and AGA8-DC2[102]. GERG-2004 ● 300.000 K, ▲ 350.000 K, ♦ 400; AGA8-DC2 ○ 400 K, Δ 350.000 K, ◊ 450.000 K.

Table 14. Second and Third Virial Coefficients

T/K	B/(cm^{3}mol^{-1})	C/(cm^{3}mol^{-1})^2
300.000	-47.5407	2638.812
350.000	-31.0707	2539.004
400.000	-19.437	2338.606

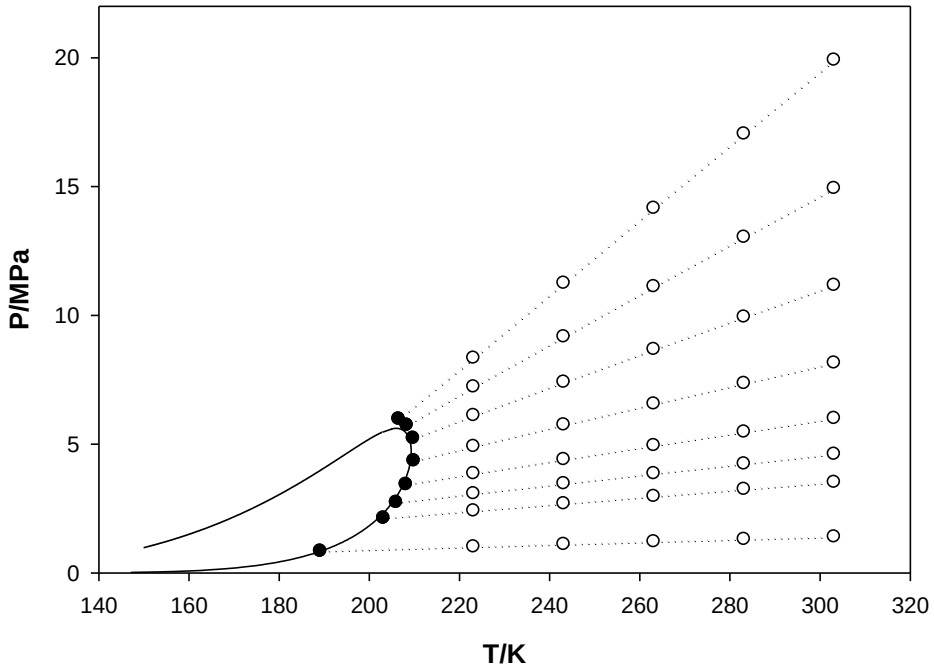

Figure 47. Isochoric experimental design.

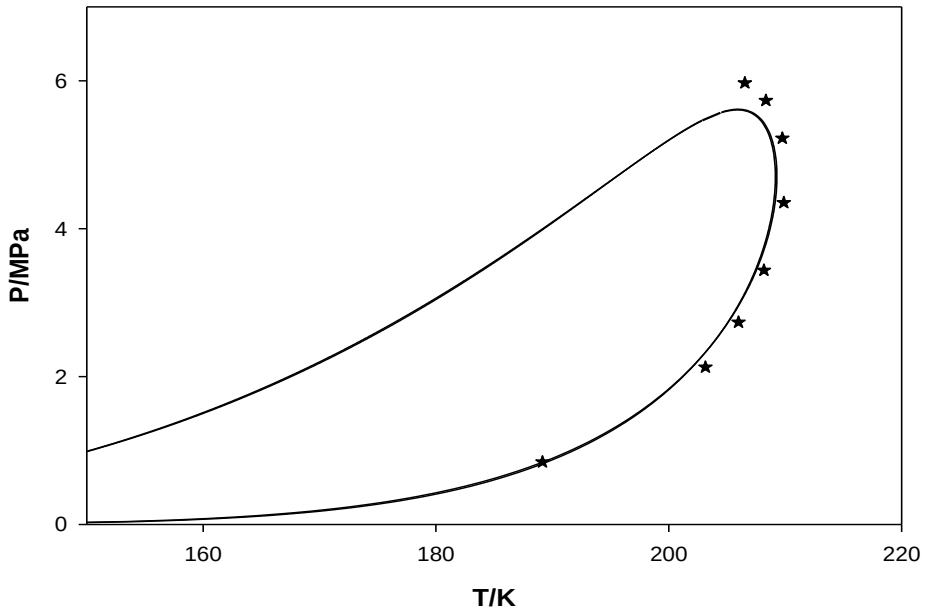

Figure 48. Experimental phase boundary. ★ Experimental data; ___ Peng-Robinson EoS.

Table 15. **Binary Coefficient Parameters for Peng –Robinson EoS**

	Methane		
Methane	-	Ethane	
Ethane	-0.0021	-	Propane
Propane	-0.0029	0.008	-

The saturation densities and the correction for the isochoric derivatives used the procedures describes in the Chapter III. Figure 49 presents the experimental temperature and density diagram for the ternary sample. The numerical values are in Table 16.

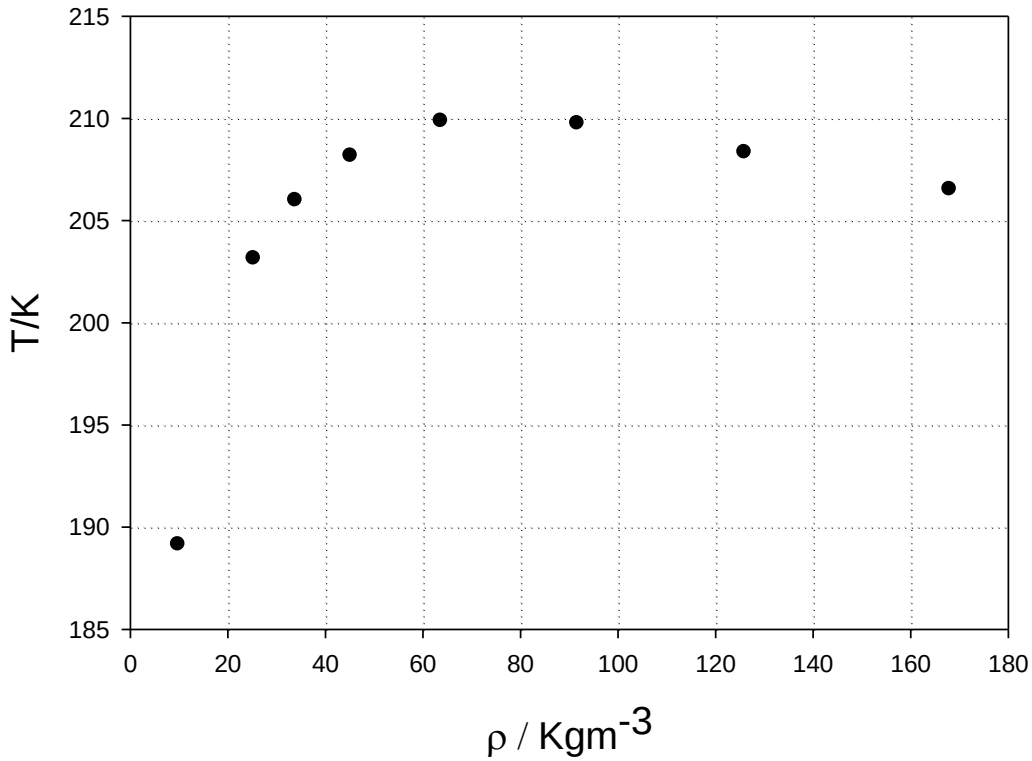

Figure 49. Experimental temperature-density diagram.

Table 16. Phase Boundary Data

T/K	P/MPa	ρ' /Kgm^{-3}
206.540	5.972	167.946
208.340	5.734	125.913
209.756	5.224	91.623
209.879	4.350	63.656
208.174	3.436	45.159
205.999	2.735	33.829
203.150	2.127	25.275
189.149	0.845	9.795

A comparison between the corrected experimental derivatives and GERG-2004 EoS appear in Figure 50. A deviation of 0.5% exists with GERG-2004 for points distant from the phase loop that becomes 1% for the points close to the phase loop.

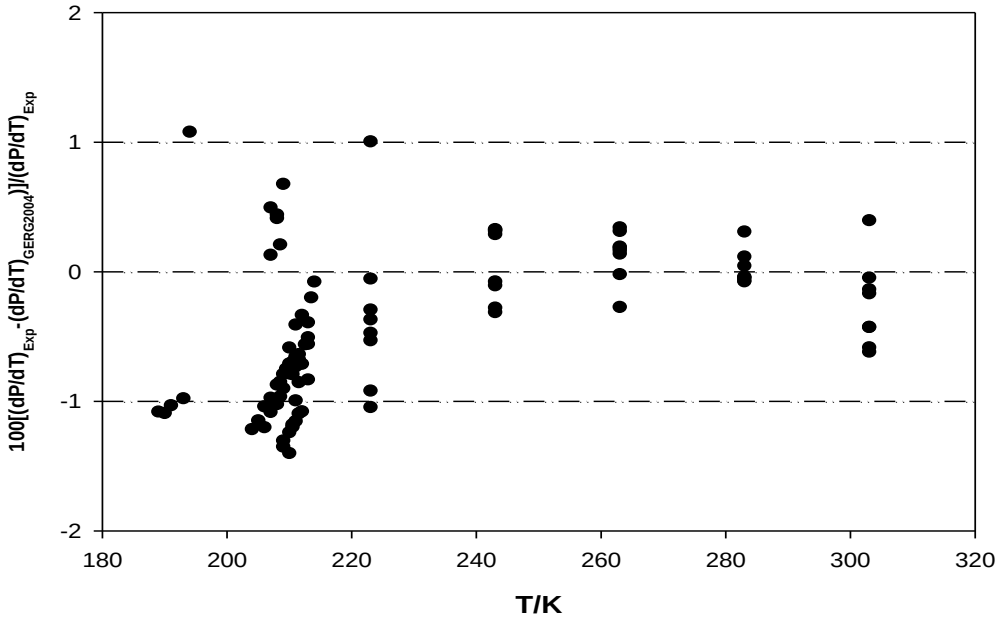

Figure 50. Relative deviations of the corrected $\left(dP/dT\right)_{\rho}$ derivative compared to GERG-2004.

4.2 Synthetic Natural Gas

Density and equilibrium data were measured for four synthetic natural gas mixtures using the MSD and the low pressure isochoric apparatus. The final data have been corrected using the methodologies for the isothermal densities and the isochoric data as presented in Chapter III. The apparatus contribution selected for the FTE was ϕ_0 =200 ppm. The compositions for the four synthetic samples were:

Table 17. Mixture Compositions (Mole Fraction)

	SAMPLE 1	**SAMPLE 2**	**SAMPLE 3**	**SAMPLE 4**
methane	0.89990	0.89982	0.89975	0.90001
ethane	0.03150	0.03009	0.02855	0.04565
propane	0.01583	0.01506	0.01427	0.02243
i-butane	0.00781	0.00752	0.00709	0.01140
n-butane	0.00790	0.00753	0.00722	0.01151
i-pentane	0.00150	0.00300	0.00450	0.00450
n-pentane	0.00150	0.00300	0.00450	0.00450
nitrogen	0.01699	0.01697	0.01713	—
carbon dioxide	0.01707	0.01701	0.01699	—

The $P\rho T$ data for samples 1 to 4 appear in Tables 18 to 21 along with comparisons to GERG-2004 [15] and AGA8-DC2 [30]. Figures 51 to 54 represent the density deviations compared to GERG-2004 and AGA8-DC2 for the four synthetic samples. Highest deviations for all the samples occur at 250 K, therefore low temperature data are necessary to improve the predictability of these multiparameter equations of state. No significant difference occurs between the two EoS for the other temperatures.

Table 18. *PρT* Data for Sample 1

T/K	P/MPa	ρ/kgm^{-3}	*ρGERG*/kgm^{-3}	100·(*ρ*-*ρGERG*)/*ρ*	*ρAGA8-DC2*/kgm^{-3}	100·(*ρ*-*ρAGA8-DC2*)/*ρ*
250.020	20.023	270.886	270.734	-0.056	272.353	0.542
250.028	29.950	314.558	314.024	-0.170	315.695	0.362
250.026	49.915	359.992	359.315	-0.188	360.489	0.138
250.003	75.019	393.058	392.694	-0.092	393.240	0.046
250.032	100.046	416.584	415.937	-0.155	416.000	-0.140
250.038	125.013	434.094	434.070	-0.005	433.751	-0.079
250.068	149.917	449.647	449.043	-0.134	448.403	-0.277
350.002	9.941	69.358	69.525	0.241	69.561	0.292
349.999	29.912	198.375	198.371	-0.002	198.505	0.066
349.997	49.954	268.390	268.265	-0.046	268.596	0.077
349.983	74.917	317.783	317.658	-0.039	317.998	0.068
350.009	99.972	350.354	350.285	-0.020	350.595	0.069
349.996	125.109	374.884	374.735	-0.040	375.030	0.039
349.990	149.891	394.219	394.060	-0.040	394.360	0.036
350.029	155.022	397.788	397.614	-0.044	397.917	0.033
450.038	9.966	49.749	49.957	0.418	49.975	0.454
450.045	29.976	141.437	141.498	0.043	141.547	0.078
450.043	49.975	206.865	206.769	-0.046	206.811	-0.026
450.059	68.914	249.744	249.671	-0.029	249.821	0.031
450.054	86.155	279.125	279.015	-0.039	279.220	0.034
450.027	114.952	315.989	315.903	-0.027	316.101	0.036
450.013	137.492	338.320	338.223	-0.028	338.393	0.022

Table 19. *PρT* Data for Sample 2

T/K	P/MPa	ρ/kgm^{-3}	*ρGERG*/kgm^{-3}	100·(*ρ*-*ρGERG*)/*ρ*	*ρAGA8-DC2*/kgm^{-3}	100·(*ρ*-*ρAGA8-DC2*)/*ρ*
250.076	12.023	190.110	190.995	0.465	192.411	1.210
250.019	14.014	219.762	220.323	0.255	222.032	1.033
249.999	16.024	242.106	242.208	0.042	244.129	0.835
249.968	17.998	259.073	258.775	-0.115	260.859	0.690
249.942	20.033	273.069	272.472	-0.219	274.679	0.590
249.894	21.996	284.284	283.503	-0.274	285.793	0.531
249.978	24.012	293.915	292.991	-0.314	295.327	0.480
250.051	26.003	302.193	301.186	-0.333	303.541	0.446
250.090	27.494	307.793	306.737	-0.343	309.096	0.423
249.986	14.995	231.398	231.848	0.195	233.669	0.982
250.033	29.999	316.320	315.294	-0.325	317.641	0.417
250.055	49.993	361.260	360.256	-0.278	362.149	0.246
249.991	68.972	387.532	386.629	-0.233	388.050	0.134
249.997	100.218	417.529	416.737	-0.190	417.550	0.005
249.969	149.856	450.256	449.633	-0.138	449.760	-0.110
349.963	9.975	70.094	70.250	0.222	70.290	0.279
349.984	11.967	85.109	85.266	0.184	85.322	0.250
350.000	13.958	100.016	100.200	0.184	100.275	0.259
349.992	15.985	114.995	115.132	0.119	115.226	0.202
350.000	17.955	129.035	129.178	0.110	129.291	0.198
350.018	19.959	142.743	142.834	0.064	142.965	0.156
349.982	21.940	155.617	155.658	0.026	155.807	0.122
349.996	23.914	167.667	167.641	-0.016	167.810	0.085

Table 19. Continued

T/K	P/MPa	ρ/kgm^{-3}	$\rho GERG$/kgm^{-3}	$100\cdot(\rho-\rho GERG)/\rho$	$\rho AGA8\text{-}DC2$/kgm^{-3}	$100\cdot(\rho-\rho AGA8\text{-}DC2)/\rho$
349.993	25.879	178.859	178.819	-0.023	179.014	0.087
349.996	27.959	189.911	189.836	-0.039	190.067	0.082
349.992	29.877	199.491	199.300	-0.096	199.571	0.040
349.983	9.998	70.244	70.418	0.248	70.458	0.304
350.020	29.988	199.950	199.808	-0.071	200.081	0.066
350.030	49.989	269.799	269.323	-0.176	269.968	0.063
349.992	68.941	309.320	308.790	-0.171	309.555	0.076
350.028	99.948	351.590	351.015	-0.163	351.844	0.072
350.012	149.913	395.369	394.732	-0.161	395.641	0.069
450.006	10.054	50.657	50.693	0.071	50.711	0.107
450.034	11.969	60.380	60.319	-0.100	60.344	-0.059
450.001	13.976	70.404	70.316	-0.125	70.348	-0.079
450.018	15.961	80.164	80.048	-0.145	80.090	-0.093
450.016	17.971	89.876	89.727	-0.165	89.779	-0.108
449.923	19.975	99.375	99.182	-0.195	99.243	-0.133
449.939	21.977	108.611	108.363	-0.228	108.433	-0.163
449.919	23.985	117.585	117.315	-0.229	117.393	-0.163
449.999	25.976	126.186	125.877	-0.245	125.961	-0.179
449.986	27.979	134.578	134.239	-0.252	134.326	-0.187
449.938	29.978	142.607	142.303	-0.213	142.393	-0.150
449.986	9.994	50.300	50.394	0.185	50.412	0.221
450.000	29.976	142.303	142.272	-0.022	142.362	0.042
449.998	49.981	207.882	207.692	-0.092	207.871	-0.005
450.000	68.945	250.899	250.634	-0.105	251.015	0.046

Table 19. Continued

T/K	P/MPa	ρ/kgm^{-3}	$\rho GERG$/kgm^{-3}	100·(ρ-$\rho GERG$)/ρ	$\rho AGA8$-$DC2$/kgm^{-3}	100·(ρ-$\rho AGA8$-$DC2$)/ρ
449.989	99.967	299.379	299.025	-0.118	299.581	0.068
450.000	149.899	350.038	349.589	-0.128	350.212	0.050

Table 20. $P\rho T$ Data for Sample 3

T/K	P/MPa	ρ/kgm^{-3}	$\rho GERG$/kgm^{-3}	100·(ρ-$\rho GERG$)/ρ	$\rho AGA8$-$DC2$/kgm^{-3}	100·(ρ-$\rho AGA8$-$DC2$)/ρ
250.016	13.964	221.001	221.647	0.292	223.755	1.246
249.977	16.015	243.888	243.878	-0.004	246.287	0.984
250.039	17.997	260.725	260.129	-0.228	262.754	0.778
250.060	20.044	274.663	273.669	-0.362	276.458	0.653
250.010	22.012	285.917	284.628	-0.451	287.528	0.564
250.043	24.019	295.545	294.069	-0.500	297.039	0.505
250.048	26.039	304.022	302.412	-0.529	305.422	0.461
250.033	27.998	311.340	309.629	-0.550	312.654	0.422
250.027	30.064	318.245	316.471	-0.557	319.493	0.392
249.954	14.972	232.693	233.495	0.345	235.763	1.320
249.955	29.966	317.501	316.262	-0.390	319.288	0.563
250.024	49.999	362.745	360.983	-0.486	363.597	0.235
250.025	68.966	388.959	387.170	-0.460	389.330	0.095
249.946	99.877	418.939	416.980	-0.468	418.554	-0.092
250.011	149.957	452.141	450.069	-0.458	450.972	-0.259
349.973	9.947	70.314	70.467	0.217	70.510	0.278

Table 20. Continued

T/K	P/MPa	ρ/kgm^{-3}	$\rho GERG$/kgm^{-3}	100·(ρ-$\rho GERG$)/ρ	$\rho AGA8$-DC2/kgm^{-3}	100·(ρ-$\rho AGA8$-DC2)/ρ
349.982	11.980	85.763	85.901	0.162	85.965	0.235
349.977	13.975	100.887	100.977	0.089	101.064	0.176
349.984	15.980	115.755	115.838	0.072	115.953	0.172
349.988	17.987	130.202	130.221	0.015	130.366	0.126
349.970	19.973	143.863	143.834	-0.020	144.010	0.102
349.976	21.985	156.940	156.870	-0.044	157.080	0.090
349.970	23.988	169.138	169.055	-0.050	169.304	0.098
349.981	25.975	180.228	180.334	0.059	180.630	0.223
349.976	27.967	191.240	190.886	-0.185	191.238	-0.001
349.986	29.925	200.884	200.529	-0.177	200.943	0.029
349.950	9.988	70.602	70.786	0.261	70.829	0.322
349.980	29.997	201.665	200.878	-0.390	201.295	-0.183
350.011	49.989	272.162	270.210	-0.717	271.175	-0.363
349.977	68.881	310.868	309.454	-0.455	310.642	-0.073
349.977	99.889	353.595	351.613	-0.560	352.967	-0.177
350.015	149.888	397.800	395.238	-0.644	396.761	-0.261
450.004	9.978	50.549	50.579	0.057	50.596	0.092
450.011	11.975	60.650	60.677	0.044	60.702	0.086
449.999	13.975	70.681	70.690	0.012	70.725	0.062
450.006	15.980	80.599	80.575	-0.030	80.621	0.027
450.011	15.981	80.598	80.576	-0.027	80.622	0.030
450.007	17.996	90.377	90.324	-0.058	90.383	0.007
449.972	19.972	99.746	99.681	-0.065	99.754	0.008
449.972	19.971	99.747	99.674	-0.074	99.746	-0.001

Table 20. Continued

T/K	P/MPa	ρ/kgm^{-3}	$\rho GERG$/kgm^{-3}	100·(ρ-$\rho GERG$)/ρ	$\rho AGA8$-$DC2$/kgm^{-3}	100·(ρ-$\rho AGA8$-$DC2$)/ρ
449.967	19.971	99.756	99.676	-0.080	99.748	-0.007
449.962	21.980	109.036	108.934	-0.093	109.020	-0.015
449.978	21.982	109.037	108.938	-0.091	109.024	-0.012
450.022	23.988	118.021	117.897	-0.105	117.996	-0.021
449.965	25.971	126.646	126.507	-0.109	126.618	-0.022
449.972	27.979	135.059	134.916	-0.106	135.038	-0.016
449.976	29.997	143.225	143.061	-0.115	143.193	-0.022
449.992	10.004	50.627	50.710	0.164	50.728	0.199
449.989	29.976	143.108	142.972	-0.095	143.104	-0.003
449.998	49.978	208.936	208.483	-0.217	208.804	-0.063
450.029	68.937	252.029	251.381	-0.257	251.995	-0.013
449.994	99.959	300.555	299.713	-0.280	300.619	0.021
449.995	149.926	351.272	350.214	-0.301	351.310	0.011

Table 21. $P\rho T$ Data for Sample 4

T/K	P/MPa	ρ/kgm^{-3}	$\rho GERG$/kgm^{-3}	100·(ρ-$\rho GERG$)/ρ	$\rho AGA8$-$DC2$/kgm^{-3}	100·(ρ-$\rho AGA8$-$DC2$)/ρ
249.983	20.028	282.336	281.855	-0.170	284.839	0.886
249.987	30.030	321.375	320.170	-0.375	323.110	0.540
249.997	49.946	362.707	361.178	-0.421	363.382	0.186
249.977	74.931	393.689	392.096	-0.405	393.508	-0.046
249.999	100.291	415.832	414.250	-0.380	415.070	-0.183

Table 21. Continued

T/K	P/MPa	ρ/kgm^{-3}	*ρGERG*/kgm^{-3}	100·(*ρ*-*ρGERG*)/*ρ*	*ρAGA8-DC2*/kgm^{-3}	100·(*ρ*-*ρAGA8-DC2*)/*ρ*
249.918	124.967	432.286	431.263	-0.236	431.632	-0.151
249.988	149.990	446.528	445.540	-0.221	445.532	-0.223
350.026	9.998	72.258	72.591	0.461	72.633	0.519
350.019	29.984	204.942	205.152	0.103	205.482	0.263
350.013	49.890	272.578	272.265	-0.115	273.020	0.162
349.993	74.991	320.091	319.592	-0.156	320.498	0.127
350.000	99.925	351.066	350.520	-0.156	351.462	0.113
350.018	124.942	374.231	373.751	-0.128	374.711	0.128
349.944	149.787	393.033	392.332	-0.178	393.310	0.070
450.043	9.999	51.020	51.413	0.770	51.429	0.802
450.050	30.001	144.981	145.343	0.249	145.399	0.288
450.057	49.945	210.468	210.419	-0.023	210.597	0.061
450.062	68.926	252.902	252.532	-0.146	252.947	0.018
450.027	99.965	300.112	299.522	-0.197	300.130	0.006
450.084	124.928	327.346	326.645	-0.214	327.302	-0.013
450.051	149.926	349.140	348.389	-0.215	349.073	-0.019

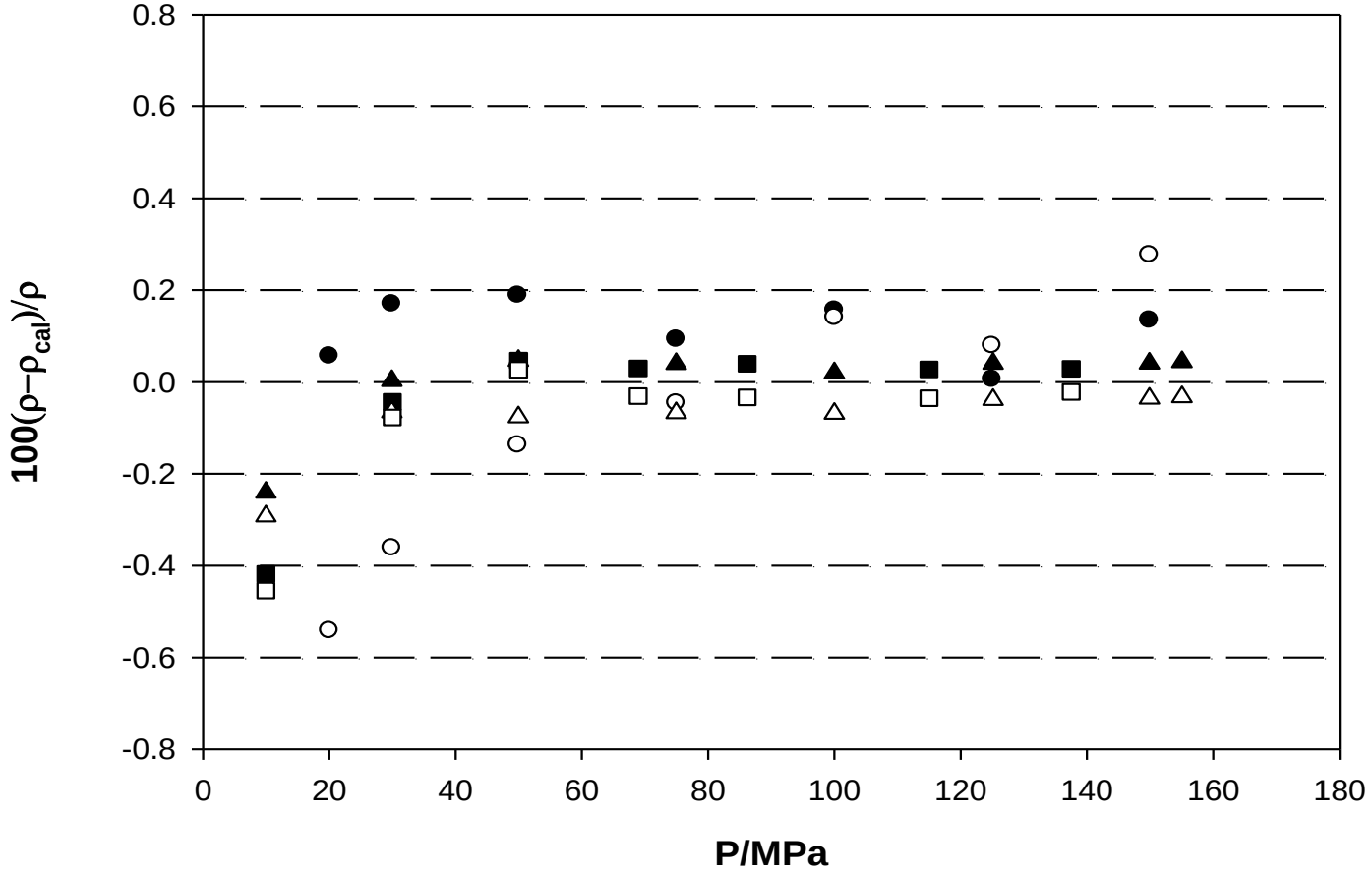

Figure 51. Sample 1 density deviations. GERG-2004, ● 250 K, ▲ 350 K, ■ 450 K; AGA8-DC2, ○ 250 K, Δ 350 K, □ 450 K.

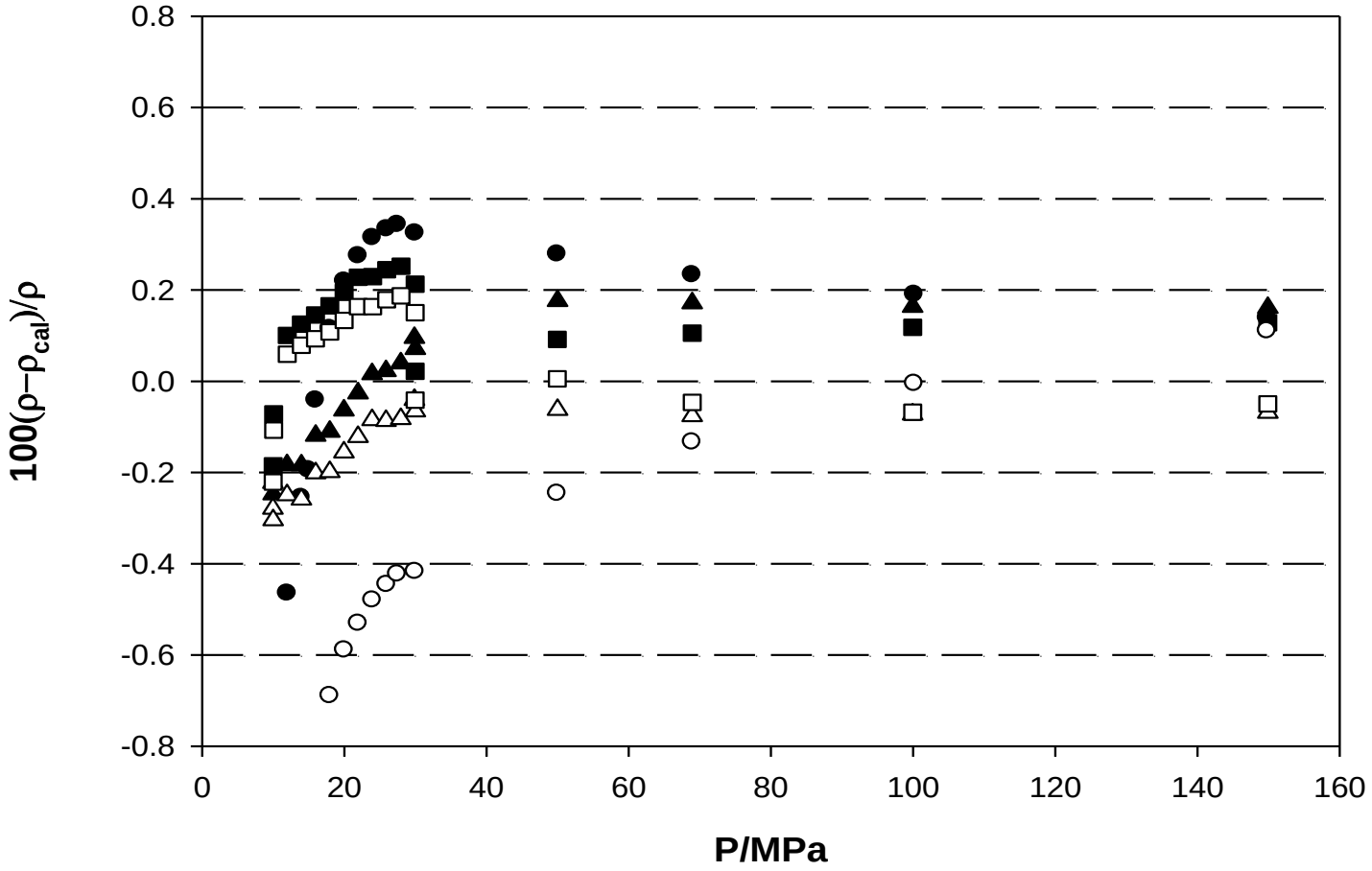

Figure 52. Sample 2 density deviations. GERG-2004, ● 250 K, ▲ 350 K, ■ 450 K; AGA8-DC2, ○ 250 K, Δ 350 K, □ 450 K.

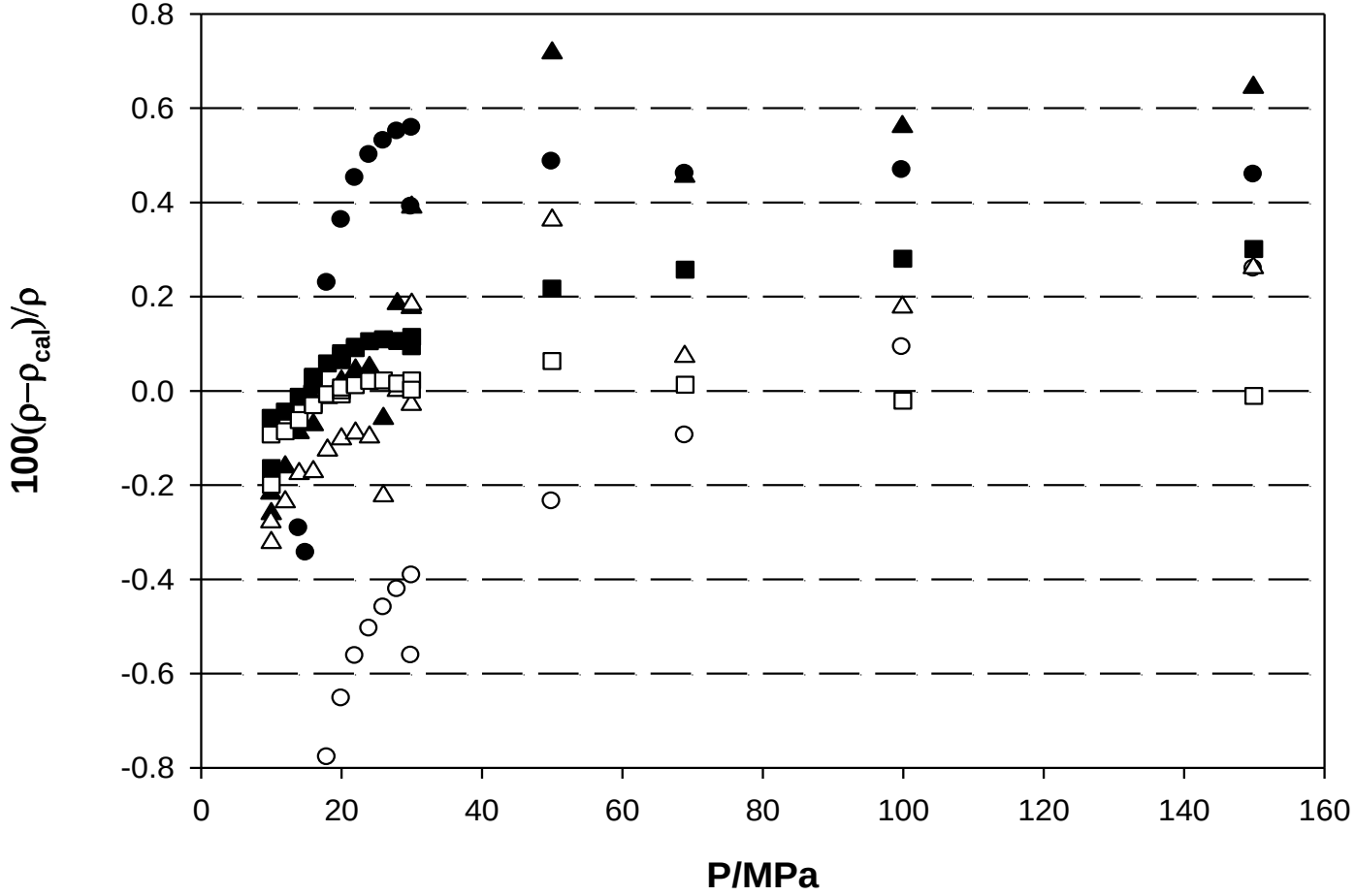

Figure 53. Sample 3 density deviations. GERG-2004, ● 250 K, ▲ 350 K, ■ 450 K; AGA8-DC2, ○ 250 K, Δ 350 K, □ 450 K.

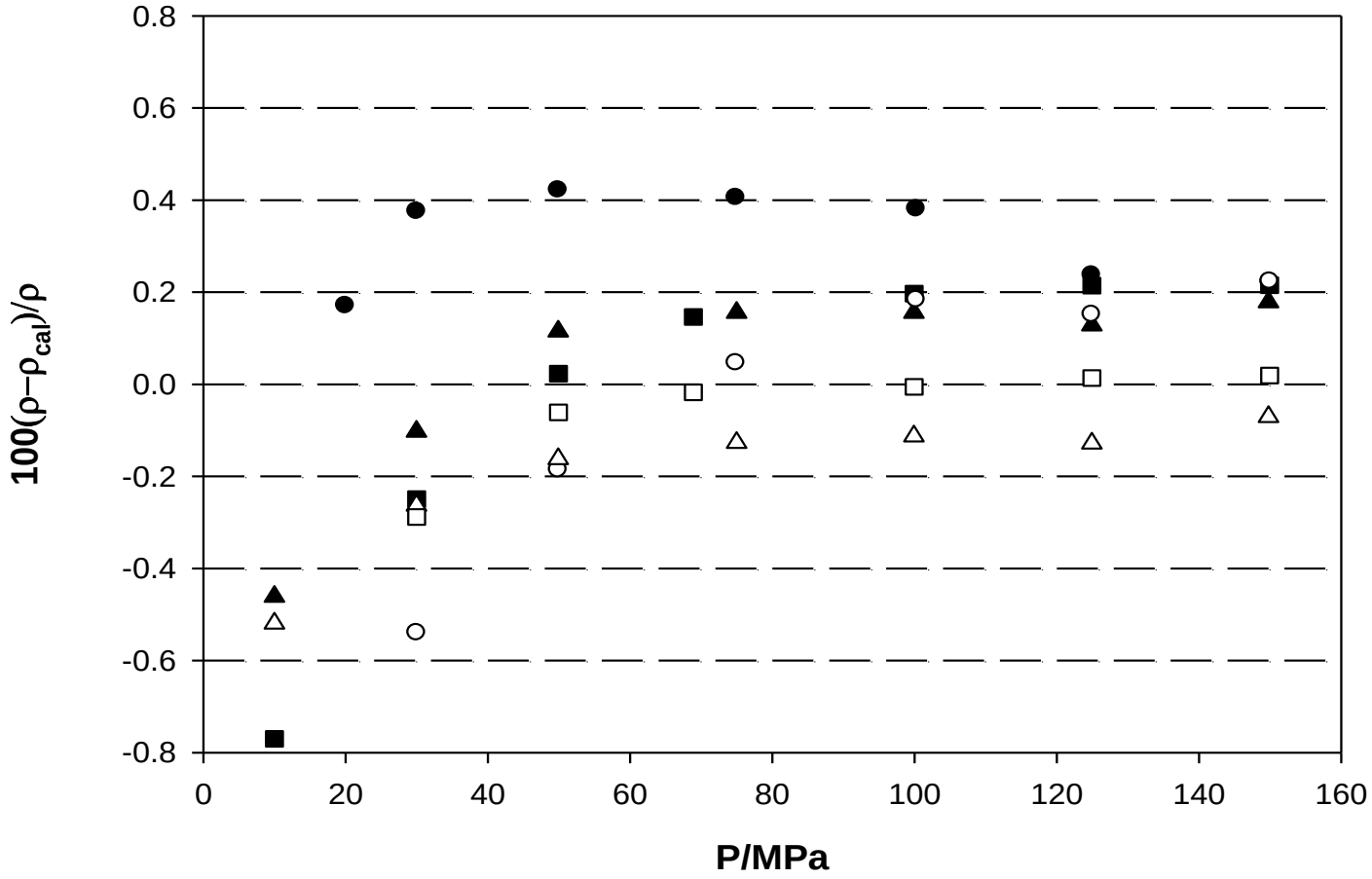

Figure 54. Sample 4 density deviations. GERG-2004, ● 250 K, ▲ 350 K, ■ 450 K; AGA8-DC2, ○ 250 K, Δ 350 K, □ 450 K.

Isochoric data determine the phase boundary data for the four synthetic samples. The raw isochoric data are in Appendix C. Tables 22 to 25 contains the phase boundary data for the synthetic samples. Figures 55 and 56 present the phase boundaries.

Table 22. Phase Boundary Data for the Sample 1

T/K	P/MPa	ρ' /Kgm^{-3}
225.6025	7.5882	158.7557
235.3435	7.9394	134.5477
241.0608	7.7931	116.7226
247.4203	7.1749	93.9198
252.5296	6.1611	71.8138
254.6000	4.8171	51.5162
252.0300	3.0468	30.5102
244.4553	1.5656	15.2759

Table 23. Phase Boundary Data for the Sample 2

T/K	P/MPa	ρ' /Kgm^{-3}
230.9600	8.7183	179.9815
240.1700	9.0836	157.2834
249.1000	9.1536	133.0381
255.6100	8.7152	114.3313
261.3700	7.7368	90.8631
263.7300	6.6819	73.2490
264.4200	5.3628	55.3067
263.6900	3.9726	38.9281
259.8900	2.3962	22.5349

Table 24. Phase Boundary Data for the Sample 3

T/K	P/MPa	ρ' /Kgm^{-3}
239.3400	9.6843	174.5326
246.5200	9.9628	158.5842
255.7300	10.0323	139.7027
264.0200	9.1559	111.9532
268.9100	7.9602	88.5818
271.6600	6.5538	67.6517
272.0400	4.9297	47.8727
271.2800	3.3136	30.5582

Table 25. Phase Boundary Data for the Sample 4

T/K	P/MPa	ρ' /Kgm^{-3}
265.6700	11.7705	164.2590
270.3900	11.1496	144.7030
276.5500	9.8675	115.4050
280.5300	8.5594	92.4190
283.8200	6.9924	69.7680
284.1000	5.3831	50.8200
280.3100	3.4557	31.2580
273.6100	1.5884	13.9260

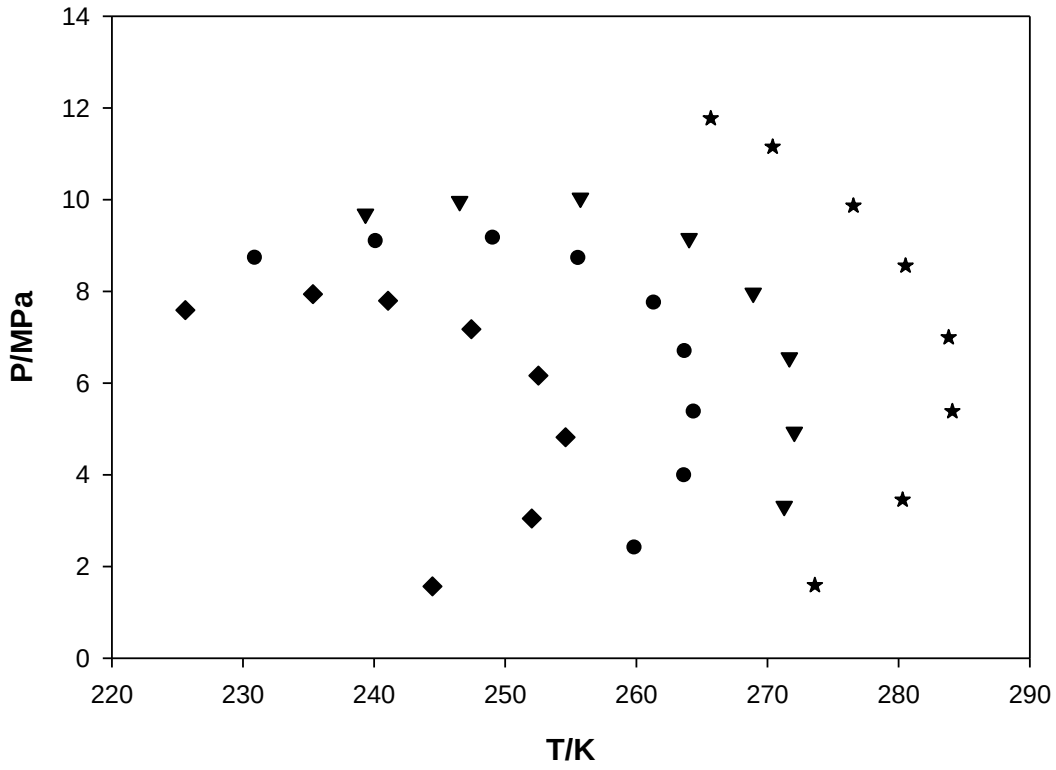

Figure 55. Phase boundaries for the samples ♦ 1, ● 2, ▼ 3, ★ 4.

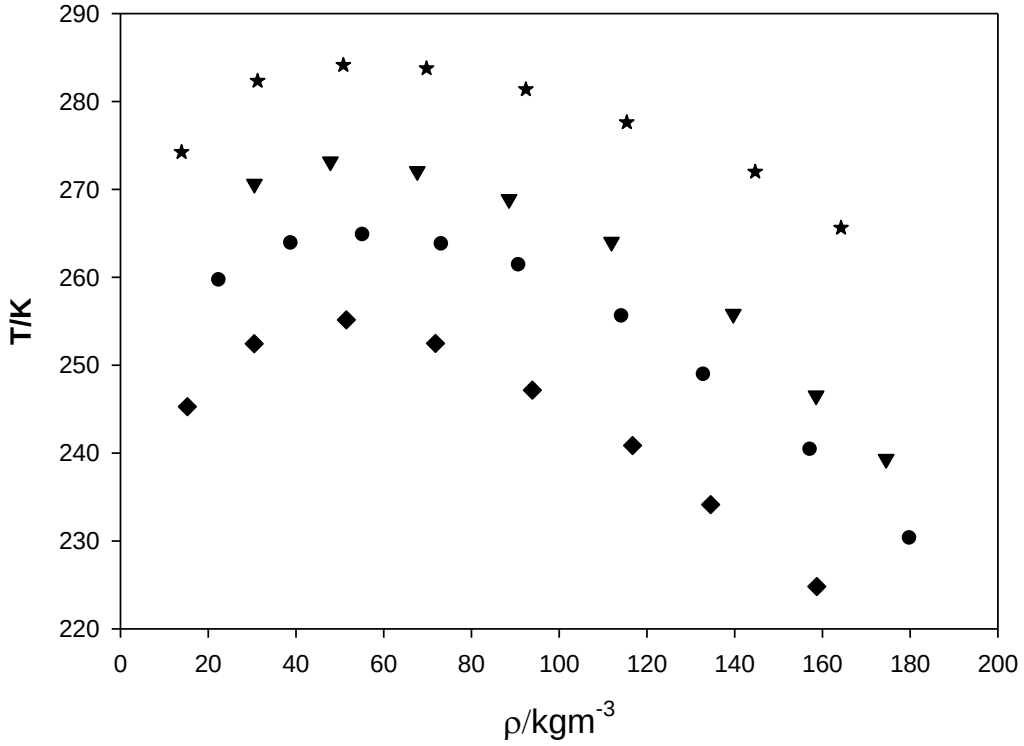

Figure 56. Temperature-density boundaries for the samples ♦ 1, ● 2, ▼ 3, ★ 4.

Figures 55 and 56 indicate that as the long-chain hydrocarbons concentrations increase, so do the cricodentherms and cricodenbars, as expected.

4.3 High Pressure Isochoric Data for a Pipeline Sample

Isochoric data for a pipeline-type mixture has been measured. The composition for this mixture appears in Table 26. The estimated uncertainty for this composition is ± 0.04 %. The data cover the range of (130 – 400) K up to 200 M. Low temperature data at high pressure were measured in the region of (130 – 250) K and (40 – 160) MPa. This region represents an important part of the thermodynamics space for natural gas mixtures unexplored in the past. Densities were determined by the intersection of densities measured at room temperature and using the methodology for the determination of saturation densities as explained in Chapter III.

Table 26. Pipeline Composition

Compound	mol %
Methane	95.014
Ethane	3.969
Propane	1.017

The experimental isochoric data and the determined densities appear in Tables 27 and 28. Additionally, bubble point determinations using the isochoric data establish the performance of the new isochoric apparatus for determining phase boundary data. Excellent consistency exists with the experimental data measured by Haynes et al. [103] and the predictions from GERG-2004.

Table 27. Isochoric 1 Experimental Data

T/K	P/MPa	ρ/kg·m^{-3}	100·(ρ-ρ*GERG*)/ρ
300.000	199.871	419.236	0.104
295.000	195.624	419.385	0.048
290.000	191.147	419.536	0.014
285.000	186.633	419.687	-0.022
280.000	182.090	419.840	-0.059
275.000	177.422	419.993	-0.087
270.000	172.833	420.146	-0.130
263.061	166.346	420.360	-0.185
259.991	163.152	420.459	-0.173
249.998	153.629	420.770	-0.258
239.999	143.910	421.084	-0.346
229.997	134.009	421.401	-0.441

Table 27. Continued

T/K	P/MPa	ρ/kg·m^{-3}	100·(*ρ*-*ρGERG*)/*ρ*
220.000	123.882	421.722	-0.539
210.000	113.535	422.047	-0.642
200.000	103.186	422.373	-0.787
190.000	92.171	422.709	-0.878
179.999	81.107	423.047	-1.011
169.999	69.828	423.391	-1.168
160.368	59.043	423.725	-1.395
159.999	58.336	423.742	-1.355
150.001	46.673	424.102	-1.590
140.984	36.172	424.434	-1.885
139.354	34.462	424.493	-1.984
137.597	24.525	424.684	-0.478

Table 28. Isochoric 2 Experimental Data

T/K	P/MPa	ρ/kg·m^{-3}	100·(*ρ*-*ρGERG*)/*ρ*
390.000	200.548	380.181	-0.09164
380.000	194.090	381.122	0.02012
375.000	190.858	381.594	0.07154
370.000	187.556	382.071	0.13057
360.000	180.895	383.032	0.24723
350.000	174.142	384.003	0.36404
340.000	167.295	384.985	0.48088

Table 28. Continued

T/K	P/MPa	ρ/kg·m^{-3}	100·(*ρ*-*ρGERG*)/*ρ*
330.000	160.343	385.977	0.59870
325.000	156.729	386.484	0.67512
320.000	153.290	386.981	0.71626
310.000	146.138	387.996	0.83222
300.000	138.943	389.019	0.93515
290.000	131.439	390.066	1.07335
279.999	123.947	391.118	1.18617
275.000	120.005	391.658	1.27172
270.000	116.329	392.183	1.29814
260.000	108.608	393.261	1.40246
249.999	100.747	394.354	1.50477
239.999	92.751	395.461	1.60238
230.000	84.608	396.585	1.69537
219.991	76.332	397.724	1.77533
210.000	67.925	398.879	1.84362
199.994	59.366	400.053	1.89354
189.999	50.678	401.244	1.91874
180.000	41.880	402.454	1.90231
170.000	33.034	403.682	1.81474
160.000	24.266	404.923	1.59846
150.000	15.646	406.177	1.20011
140.000	6.959	407.450	0.65124
135.000	2.433	408.101	0.36151
131.999	0.521	408.435	-0.11728
131.552	0.398	408.473	-0.24556

Table 28. Continued

T/K	P/MPa	ρ/kg·m^{-3}	100·(*ρ*-*ρGERG*)/*ρ*
131.647	0.426	408.465	-0.21877

Table 29 contains the experimental phase boundary data for isochoric 2. GERG-2004 reproduces the phase boundary data within the expected deviation for the EoS [15].

Table 29. Phase Boundary Data for the Isochoric 2

Phase Boundary Data	Experimental Data	GERG-2004 EoS
Temperature /K	131.243	131.243
Pressure / MPa	0.363	0.375
Density /kg·m^{-3}	408.911	409.969

MOLECULAR STUDY OF NATURAL GAS MIXTURES

A wide experimental characterization for natural gas, its main constituents and associated mixtures has appeared in the literature [15]. Thermal, volumetric and transport information have accumulated over almost a century of experimental research. However, because of variations in the compositions and the thermodynamic conditions in which natural gas occurs, important gaps remain for consideration [104]. Unfortunately, it is impossible to characterize all natural gas conditions experimentally, and in some cases experiments can be complex, unsafe and expensive.

Theoretical studies are always an important tool to overcome the limitations in experimental data. Starting from simple approximations such us the ideal gas equation, the theoretical understanding of natural gas mixtures has evolved to complex molecular simulations that involve state-of-the-art molecular theories and computational tools [104]. Despite all the results from these methods, the most useful and simple way to reproduce experimental data continues to be EOS. That is why in many cases theoretical effort focuses upon using modern molecular methods to generate molecular-based EOS [105-106]. These EOS use molecular understanding of the constituents to represent the possible interactions in the mixtures. However, gases, especially hydrocarbon gases, are "simple" systems compared to complex, highly polar and associated fluids. Still, molecular-based EOS for natural gas [18, 107-108] are not very accurate.

The main challenges for modeling natural gas from the molecular point of view are:

1. Introduce the conformational and shape effects of the long hydrocarbons (C_{4+}) in the calculations of pure and mixtures properties.
2. Develop realistic potential energy functions for the interactions of the constituents of natural gas that allow calculations of thermal, volumetric and transport properties. In some cases the so-called effective potentials improve considerably the predictions of the theoretical models [109].
3. Generate molecular based models that avoid using experimental, binary data to fit the model. In this case the model is usually called a predictive model.

4. Achieve accurate predictions of thermophysical properties. Although the molecular models are very useful for determining qualitative behaviors of natural gas mixtures, its quantitative capabilities are still low compared to empirical models for industrial needs.

This research project contains an extensive literature review analyzing the different alternatives to approach the molecular understanding of natural gases. Concepts such as "shape factor" have been developed to build molecular equations such as BACK and its family of equations [37-38, 110-111]. The Statistical Associated Fluid Theory (SAFT) has been used to develop molecular-based EOS [105-106, 112-115]. Monte Carlo methods [104, 116-118], molecular dynamics calculations [119-124] and density functional approaches [125-129] are some of the different alternatives that represent the wide spectrum of methodologies available to understand natural gas at the molecular level.

In order to establish a consistent set of molecular data based upon molecular mechanics calculations, this project used a detailed characterization using *Gaussian0*3 [130] for the main constituent of natural gas that appears in Table 30 as suggested by Kunz et al. [15]. However, Singh et al. [106] and Leonhard et al. [105] have performed an accurate description of the components. These results were tested and compared to experimental data; they suggested an excellent starting point for a systematic study of natural gases. Therefore, only calculations for molecules not considered in this reference were determined in this work. Here, the principal results are compiled for future developments, Table 31.

Singh et al. [106] determined an excellent frame of molecular data that consists essentially of dipole and quadrupole moments, and isotropic polarizabilities, Table 31. For perturbation theory treatment, which is the fundamental methodology for development of molecular EOS such as SAFT, these properties are the fundamental parameters for calculating molecular interaction and proposing new model interactions[105]. The simplified representation of the different contribution to the Helmholtz energy model is:

$$A^{res} = A^{hs} + A^{chain} + A^{assoc} + A^{disp} + A^{QQ} + A^{DD} \quad (5.1)$$

where hs, chain, assoc, disp, QQ and DD refer to the hard sphere, chain, association, dispersion, quadrupole and dipole Helmholtz energy contributions respectively.

Table 30. Natural Gas Main Constituents

Compound	**Compound**
Methane	Nonane
Ethane	Decane
Propane	Nitrogen
Butane	Carbon Dioxide
Iso-Butane	Carbon Monoxide
Pentane	Hydrogen Sulfide
Iso-Pentane	Hydrogen
Hexane	Water
Heptane	Oxygen
Octane	

Table 31. Dipole Moment, Quadrupole Moment and Isotropic Polarizability for the Main Constituents of Natural Gas

Molecule	Method for μ and θ	μ_x (D)	μ_y (D)	μ_z (D)	θ_{xx} (B)	θ_{yy} (B)	θ_{zz} (B)	α_1 (10^{-24}cm^3)	α_2 (10^{-24}cm^3)	α_3 (10^{-24}cm^3)
CH_4	B3LYP/6-31g(d)[a]	0	0	0	0	0	0	2.56[b131]		
C_2H_6	MP2/aug-cc-pVDTZ//B3LYP/TZVP	0	0	0	0.376	0.376	-0.752	4.207	4.221	-
C_3H_6	MP2/aug-cc-pVDTZ//B3LYP/TZVP	0	0.087	0	-0.637	-0.073	0.71	6.003	6.014	-
n-C_4H_6	MP2/aug-cc-pVDTZ//B3LYP/TZVP	0	-0.016	-0.033	-0.903	0.151	0.752	7.780	7.791	-
i-C_4H_6	MP2/aug-cc-pVDTZ//B3LYP/TZVP	0	0.000	-0.133	-0.343	-0.346	0.689	7.814	7.827	-
n-C_5H_6	MP2/aug-cc-pVDZ//B3LYP/TZVP	0	0	0	-1.036	-0.404	1.44	9.368	-	-
i-C_5H_6	B3LYP/6-31g(d)[a]	0.0843	0.0184	0	-0.0969	0.0239	0.0730	-	-	-
n-C_6H_6	MP2/aug-cc-pVDZ//B3LYP/TZVP	0	0	0	-1.286	0.0062	1.224	11.482	-	-
n-C_7H_6	B3LYP/6-31g(d)[a]	0	0.0543	0	-0.8542	-0.1707	1.0249	-	-	-
n-C_8H_6	MP2/aug-cc-pVDZ//B3LYP/TZVP	0	0	0	-2.400	-0.121	2.521	15.195	-	-
n-C_9H_6	B3LYP/6-31g(d)[a]	0	0.0543	0	-1.1344	-0.2411	1.3754	-	-	-
$C_{10}H_6$	MP2/aug-cc-pVDZ//B3LYP/TZVP	0	0	0	-0.362	-0.367	0.729	10.485	-	-
N_2	CCSD(T)/aug-cc-pVTZ	0	0	0	0.744	0.744	-1.488	1.679	1.707	1.753
CO_2	CCSD(T)/aug-cc-pVTZ	0	0	0	2.136	2.136	-4.272	2.558	2.643	2.595
CO	CCSD(T)/aug-cc-pVTZ	0	0	-0.101	0.985	0.985	-1.970	1.923	1.968	1.951
H_2S	CCSD(T)/aug-cc-pVTZ	0	0	0.980	-3.708	2.786	0.930	3.488	3.716	3.602
H_2	B3LYP/6-31g(d)[a]	0	0	0	-0.1415	-0.1415	0.2830	-	-	-
H_2O	CCSD(T)/aug-cc-pVTZ	0	0	1.841	2.573	-2.473	-0.125	1.372	1.450	1.391
O_2	B3LYP/6-31g(d)[a]	0	0	0	0.1529	0.1529	-0.3057	-	-	-

Multipole moments are reported in a quadropole principal axis. Methodology to calculate α_i appears in [106].

[a] Values determined in this research.

[b] Parameter extracted from literature.

The implementation of the PCP-SAFT EOS [105] using these parameters leads to a significant improvement in predictive capabilities when compared to similar molecular EOS such us PC-SAFT[18]. For instance, an average deviation of 0.6% exists for the vapor pressure predictions of pure components with PCP-SAFT; in the case of PC-SAFT, it is about 2%. However, the experimental uncertainty for the vapor pressure of most of the pure compounds is around 0.02%. The same result was found in the case of binary mixtures. Therefore, it appears that additional improvements are possible in the future.

5.1 Molecular Dynamics Simulations

Molecular dynamics calculations were performed during this research project to establish the accuracy of the method in the determination of volumetric properties such as density. A simple binary system of methane-ethane 0.5-.0.5% was simulated using the DL_POLY 2.12 program. NPT simulations were performed using the NPT Hoover algorithm with 0.1 ps as the barostat and thermostat relaxation times. The number of molecules were 200 and the force field was OPLS-AA [32]. An equilibration time of 0.1 ns was used, and the average was taken with simulations of up to 10 ns to observe the effect of the simulation time on the accuracy of the density predictions compared to REFPROP 8.0 [26].

Highest deviations were found for pressures up to 4 bar with a simulation time of 1 ns at room temperature, Figure 57. Therefore, the effect of the simulation time was analyzed in respect of the quality of the predictions. The effect of the simulation time is in Figure 58. For a simulation time higher than 2 ns, the deviations of the density predictions fall within a band of 5%. For higher pressures of 6, 7 and 8 bar the deviation band is around 2%, Figure 59. Therefore, increasing the simulation time and the pressure of the system leads to lower deviations compared to high accuracy standards. The highest deviations a low pressure and short simulation times can be attributed to high oscillations in the pressure during the simulations.

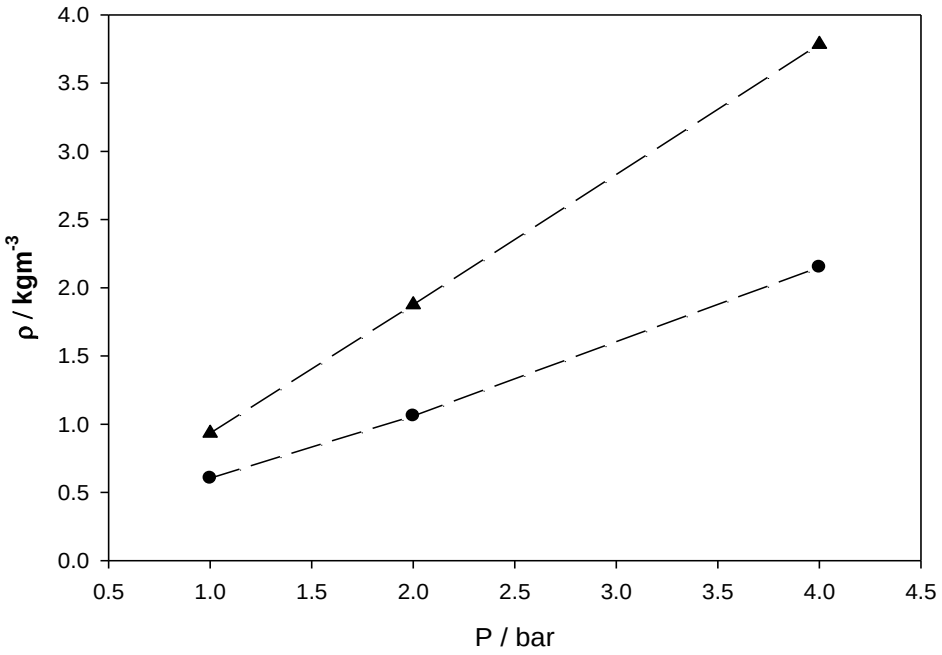

Figure 57. Density predictions for methane-ethane mixture. 298 K, 1 ns of simulation time ▲ REFPROP 8.0, ● DL_POLY 2.12.

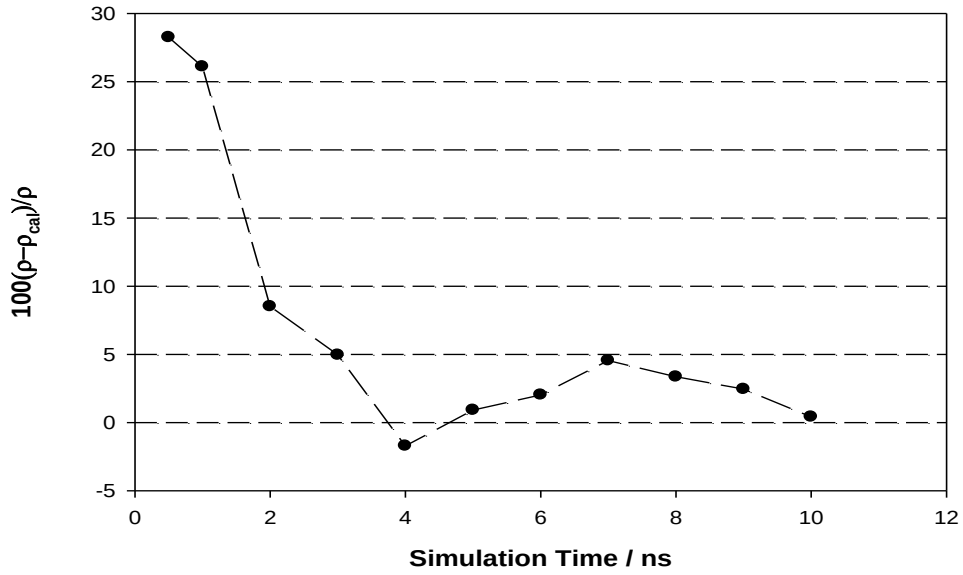

Figure 58. Density deviations for methane-ethane mixture at 5 bar and 298 K.

Finally, Figure 60 represents the radial distribution functions for this system at 298 K and 1 bar. This structural information can be used for further developments and comparisons of mixing rules using the energy equation.

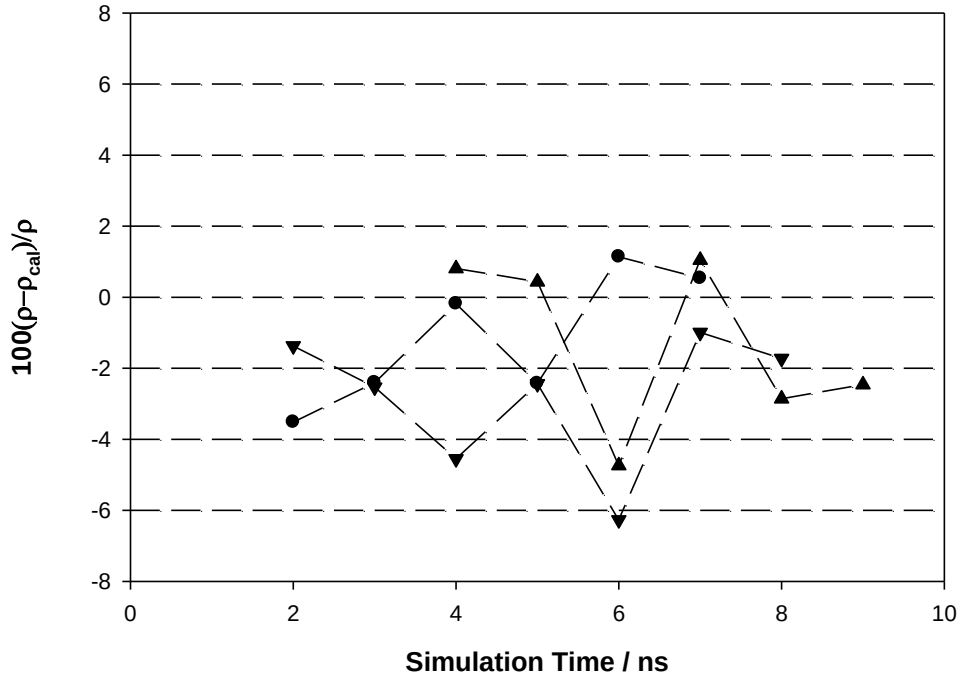

Figure 59. Density deviations for methane-ethane mixture. ● 6 bar, ▲ 7 bar, ▼ 8 bar.

5.2 Conformational Analysis and New Mixing Rule

A new technique to account for isomeric interactions in gas mixtures follows. The analysis uses the fact that, for the same type of molecule in the mixtures, there are different rotational isomers. Therefore, there are interactions not just between different types of molecules but different types of isomers of the same molecule with isomers of different molecules. This assumption leads to:

$$a_{mix} = \sum_{ij} x_i x_j a_{ij} \equiv \sum_{ij} \sum_{kl} x_i^k x_j^l a_{ij}^{kl} \,, \qquad (5.2.1)$$

where x_i^k is the composition of the k-isomer of the i-molecule and a_{ij}^{kl} is the binary interaction tensor that accounts for the interaction between the k-isomer of the i-molecule with the l-isomer of the j-molecule.

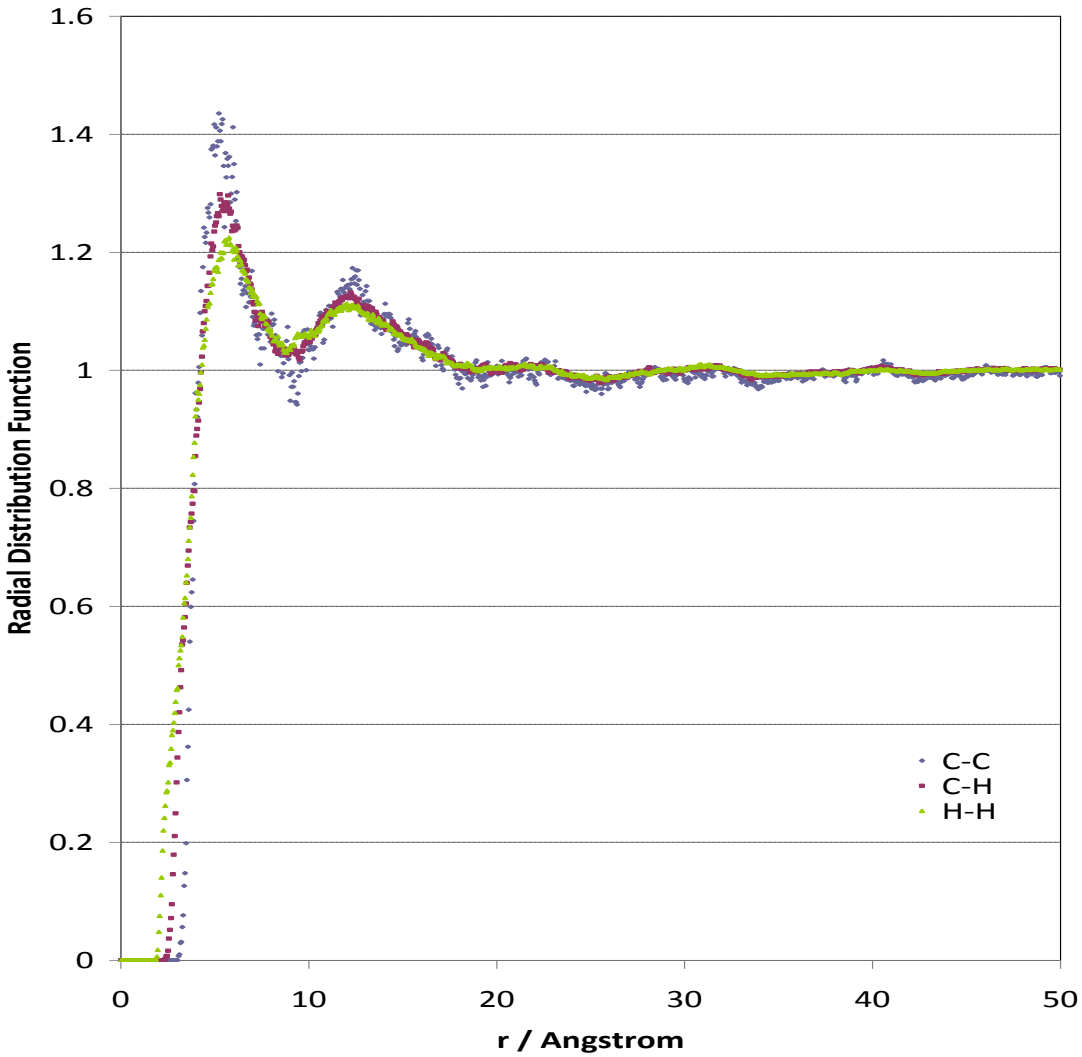

Figure 60. Radial distribution functions for methane-ethane mixture at 1 bar and 298 K.

Now, the x_i^k variable can be:

$$x_i^k = x_i P_i^k \tag{5.2.2}$$

where $P_i^k(T)$ is the probability of having the k-isomer of the i-molecule at temperature *T*. Then,

$$a_{mix} = \sum_{ij}\sum_{kl} x_i x_j P_i^k P_j^l a_{ij}^{kl} \ . \tag{5.2.3}$$

Now, the correlation proposed by Bartell and Khol [132] can determine the probability distribution of the i-isomer of the l-molecule as a function of temperature

$$P_l^i \Big/ P_l^j = m^i \Big/ m^j \exp\left(-(n_i - n_j)\Delta G^0 / RT\right). \tag{5.2.4}$$

where m_i is the multiplicity of each isomer, n_i is the number of *gauche* conformations in the isomer and ΔG^0 is a fitting parameter. Then, the a_i^k parameters can be found from the a_i parameter for pure compounds determined from any EOS using equations 5.2.4 and 5.2.5

$$a_i(T) = \sum_k P_i^k(T) a_i^k \ . \tag{5.2.5}$$

Finally the a_{ij}^{kl} parameter can be calculated from the geometric average $\sqrt{a_i^k a_j^l}$.

In order to proof the former hypothesis, a binary system of methane-heptane 50-50 mol% was analyzed. Volumetric data for methane and ethane came from REFPROP 8.0 to estimate the parameters of the model. The parameters for n-heptane are in Table 32. Methane does not have an isomer. The model to evaluate the hypothesis was the Redlich-Kwong EOS. Comparisons to the Peng-Robinson EOS and the Redlich-Kwong EOS used binary interaction parameters. Figures 61 to 63 indicate a considerable improvement for determining the compressibility factor, Z, compared to REFPROP 8.0, Peng-Robinson and Redlich-Kwong using binary interaction parameters. However,

these preliminary results are inconclusive without an extensive analysis of different systems and properties using this new formulation.

Table 32. Isomeric Data for Heptane Using Redlich-Kwong EOS

Isomer	ΔG	2399 J/mol	m_i	n_i
TTTT	a1	13135107	1	0
TTTG	a2	24632138	4	1
TTGT	a3	24632138	4	1
TTGG	a4	2918096	4	2
GTTG	a5	2918096	4	2
TGTG	a6	11671933	8	2
TGGT	a7	729498.7	2	2
TGGG	a8	333030.7	4	3
GTGG	a9	1385953	8	3
GGGG	a10	8695.221	2	4

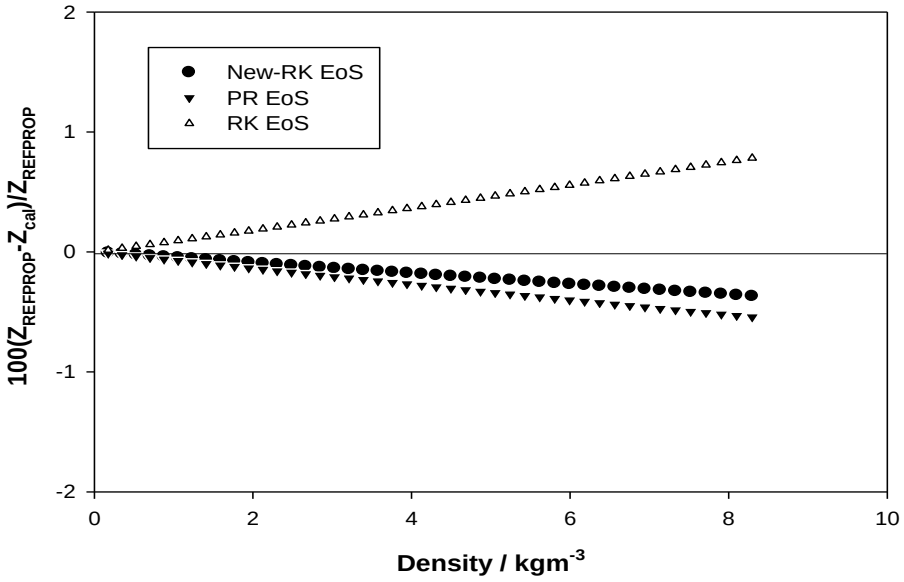

Figure 61. Compressibility factor deviations from new Redlich-Kwong EOS at 400 K.

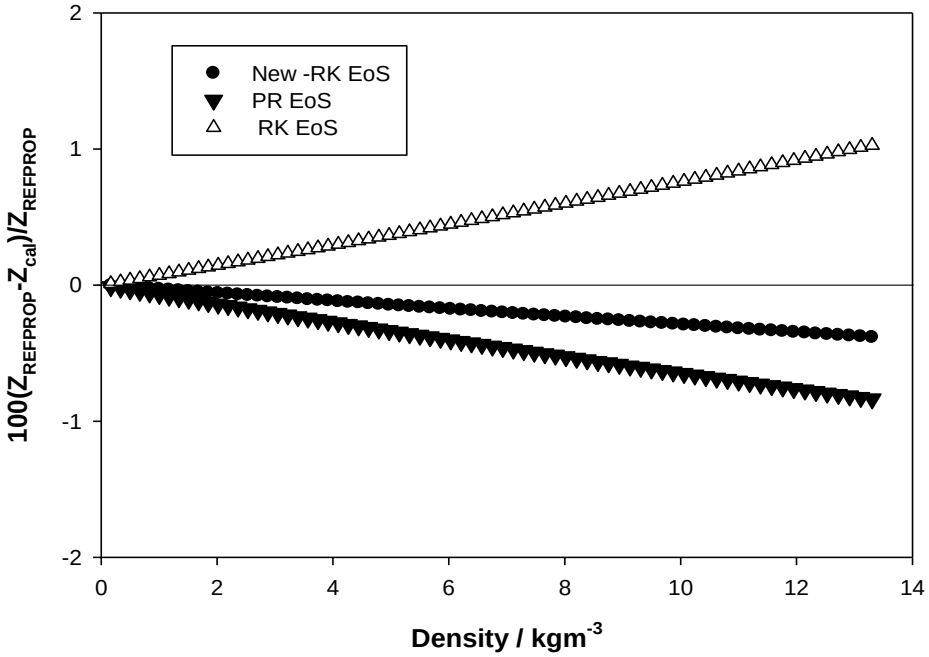

Figure 62. Compressibility factor deviations for the new Redlich-Kwon EoS at 420 K.

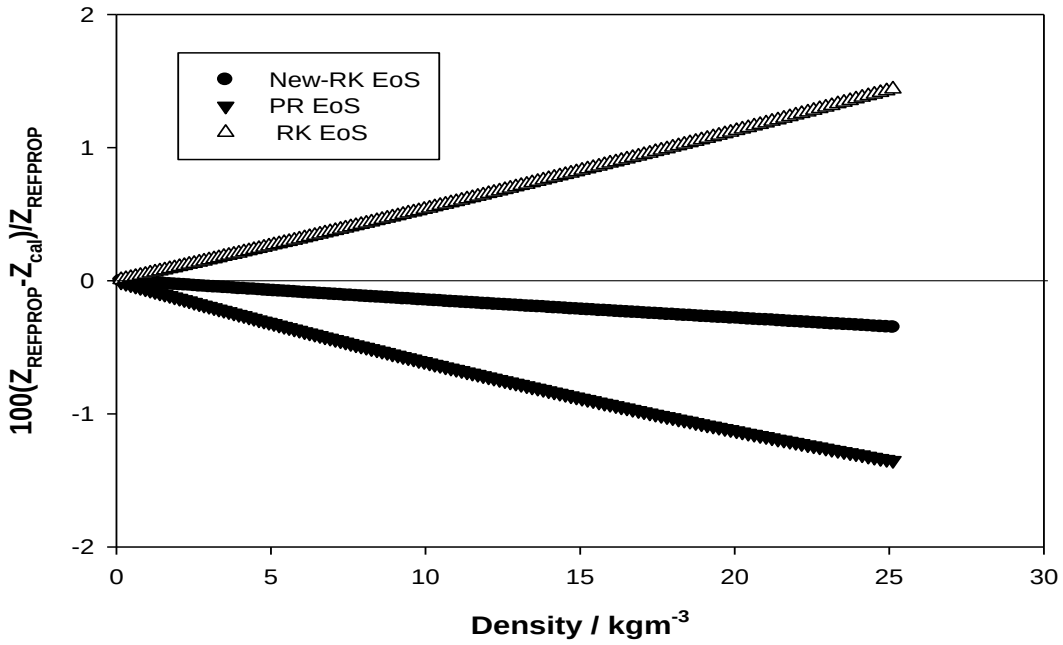

Figure 63. Compressibility factor deviations for the new Redlich-Kwon EOS at 450 K.

CONCLUSIONS AND RECOMMENDATIONS

Highly accurate experimental $P\rho T$ data for the main constituents of natural gas, methane and ethane, were measured up to 200 MPa. These are the first high-accuracy, high-pressure data reported in the literature for these compounds, they can be classified as reference data. After compensating for the force transmission error experienced by the high pressure MSD of the thermodynamics research group at Texas A&M University, a relative uncertainty for the density measurements is ≤ 0.05%. This result leads us to conclude that this apparatus is the most accurate, current, high-pressure densimeter.

Highly accurate experimental $P\rho T$ data were measured for synthetic natural gas mixtures up to 200 MPa. For two ternary mixtures of methane, ethane and propane, the GERG-2004 EOS displays better predictive capability than the AGA8-DC2 EOS. However, for four multicomponent synthetic natural gas mixtures (more than 8 components) the two EOS are comparable.

A new, high-accuracy high-pressure isochoric apparatus was developed to operate in the range of temperature from 100 to 500 K up to 200 MPa. This new apparatus allows determination of bubble points for natural gas mixtures and spans the range of high-pressure to low-temperature isochoric data; regions that were not available for previous experimental data. Additionally, a low-pressure isochoric apparatus was re-assembled and calibrated to determine dew points. For these two apparatus, a new methodology for the determination of phase envelope data was developed. The estimated relative uncertainties for the pressure, temperature and saturation density are 0.04%, 0.45% and 0.12% respectively. Finally, a methodology for correcting the isochoric experimental slope was developed; the estimated uncertainty for these data is 0.5% for temperatures distant from the phase loop of the mixture.

A new methodology for the determination of gas composition was proposed. This technique consists in coupling CARS-GC data to minimize the high uncertainty of the long-chain hydrocarbons in the mixture. A Raman gas chamber was built and initial tests performed. The well-defined line of the CARS spectrum leads to the conclusion that considerable improvements can be obtained using this new technique. The new

methodology can achieve uncertainties less than 0.0005 in the mole fraction for the long-chain hydrocarbons and low composition compounds present in natural gas mixtures.

The main constituents of natural gas were characterized by quantum mechanics calculations from accurate data found in the literature and obtained in this research project. The implementation of these new data into a new, predictive, molecular-based EOS leads to considerable improvements for these types of equations. However, the deviations in the predictions of vapor pressures compared to experimental data for pure compounds shows that additional improvements are necessary to satisfy industrial needs.

Molecular dynamics calculations for a methane+ethane mixture were performed to establish the accuracy of the predictions of volumetric properties with this technique compared to high-accuracy EOS. The main conclusions drawn were that simulation times greater than 2 ns are necessary to improve the results of the simulation, and that increasing the pressure of the analyzed system minimizes the deviations of the density calculations.

A new scheme to introduce the isomeric effects in cubic EOS was proposed. This methodology accounts for the isomer-isomer interaction in the gas mixture. Preliminary results for a mixture of methane+octane suggest that the predictions of compressibility factor are improved without using binary interaction parameters for the mixing rule.

The following recommendations are suggested to extend this research:

The low-pressure capabilities of the high-pressure MSD should be improved by introducing an additional low-pressure transducer (1500 psia) to minimize the uncertainties of the low pressure measurements.

An analysis of the sinker mass effect should be performed. Preliminary results suggest that reducing the mass of the sinker decreases the apparatus effect of the force transmission error. If this hypothesis is true, it should be possible to compensate the fluid effect in the force transmission error of the MSD and improve the accuracy of the measurements.

The proposed models for the quitinc EOS should be fit to accurate thermodynamics data. Using the inversion problem methodology, the non-linear fit

technique developed by Lemmon et al. [26] promises to be an excellent alternative for accurate predictions of thermodynamic properties using less computational time than a multiparameter EOS.

The CARS-GC methodology for determining gas compositions should be developed systematically; calibration curves should be determined for key components in the mixtures at constant temperature and pressure.

Real natural gas compositions for natural gas mixtures should be evaluated using molecular dynamics methods in order to establish the composition effect on the accuracy of the calculations. Additional analyses using Monte Carlo methods must be developed for equilibrium properties determinations.

A systematic analysis should be completed for the new isomer-isomer interaction mixing rule for gases. Volumetric, equilibrium and thermal properties should be studied in order to evaluate the capabilities of this new approach.

REFERENCES

(1) http://www.eia.doe.gov/emeu/mer/overview.html. Link last retrieved 2/11/2010.

(2) Patil, P. V. Commissioning of a magnetic suspension densitometer for high-accuracy density measurements of natural gas mixtures. PhD. Dissertation, Texas A&M University, College Station, 2005.

(3) http://www.eia.doe.gov/aer/pdf/aer.pdf. Link last retrieved 3/03/2010.

(4) http://www.fossil.energy.gov/news/techlines/2003/tl_liqphasemethanol_sucess.html. Link last retrieved 3/03/2010.

(5) U.S. Department of Energy. The tampa electric integrated gasification combined-cycle project: An update. U.S. DoE topical report No. 19; U.S. Department of Energy: Washington, DC, July 2000.

(6) http://www.netl.doe.gov/technologies/coalpower/fuelcells/publications/fuelcell/fc-cleanup/futuregen_report_march_04.pdf. Link last retrieved 3/03/2010.

(7) MacDougall, L.V. Methanol to fuels routes - the achievements and remaining problems. *Catalysis Today* **1991,** *8(3)*, 337-369.

(8) http://www.allbusiness.com/mining/oil-gas-extraction-crude-petroleum-natural/530964-1.html. Link last retrieved 3/03/2010.

(9) http://www.allbusiness.com/energy-utilities/oil-gas-industry-oil-processing-products/6148618-1.html. Link last retrieved 3/03/2010.

(10) http://wh.conocophillips.com/about/reports/ar/e_p.htm. Link last retrieved 3/03/2010.

(11) http://minerals.usgs.gov/minerals/pubs/country/2003/qamyb03.pdf. Link last retrieved 3/03/2010.

(12) Baud, R.D.; Peterson, R.H.; Richardson, G.E.; French, L.S.; Regg, J.; Montgomery, T.; Williams, T.S.; Doyle, C.; Dorner, M. Deepwater Gulf of Mexico 2002: America's expanding frontier. *US Department of the Interior Publication OCS*. OCS Report, MMS 2002-021, New Orleans, LA, Apr. 2002.

(13) Wang, X.; Bomba, J. G. *Proceedings of the 13th International Conference on Offshore Mechanics and Arctic Engineering*. Houston, February 27-March 3; American Society of Mechanical Engineers: Houston, **1994**; pp 343-350.

(14) Katz, D.L.; Cornell, D.; Vary, J.A.; Kobayashi, R.; Elenbaas, J.R.; Poettmann, F.H.; Weinaug, C.F. *Handbook of Natural Gas Engineering*, McGraw-Hill Book Co, New York, N.Y, **1959**.

(15) Kunz, O.; Klimeck, R.; Wagner, W.; Jaeschke, M. *The GERG-2004 Wide-Range Equation of State for Natural Gases and Other Mixtures*. Vol. 6, Fortschritt-Berichte VDI, Number 557, **2007**.

(16) Sengers, J.V.; Kayser, R.F.; Peters, C.J.; White Jr, H.J. *Equations of State for Fluids and Fluid Mixtures*. Vol. V, Elsevier, Amsterdam, **2000**.

(17) Zhou, J. Automated isochoric apparatus for pVT and phase equilibrium measurements on gas mixtures. PhD. Dissertation, Texas A&M University, College Station, 2005.

(18) Aparicio-Martinez, S.; Hall, K. R. Use of PC-SAFT for global phase diagrams in binary mixtures relevant to natural gases. 1. n-alkane plus n-alkane. *Industrial & Engineering Chemistry Research* **2007,** *46* (1), 273-284.

(19) Redlich, O.; Kwong, J. N. On the thermodynamics of solutions: An equation of state; fugacities of gaseous solutions. *Chem Rev* **1949,** *44* (1), 233-44.

(20) Soave, G. Equilibrium constants from a modified Redlich-Kwong equation of state. *Chem Eng Sci* **1972,** *27* (6), 1197-&.

(21) Peng, D.; Robinson, D. B. New 2-constant equation of state. *Industrial & Engineering Chemistry Fundamentals* **1976,** *15* (1), 59-64.

(22) Patel, N. C.; Teja, A. S. A new cubic equation of state for fluids and fluid mixtures. *Chem Eng Sci* **1982,** *37* (3), 463-473.

(23) Valderrama, J. O. The state of the cubic equations of state. *Industrial & Engineering Chemistry Research* **2003,** *42* (8), 1603-1618.

(24) Hall K.R.; Atilhan, M. New equation of state for argon. *J. Chem. Eng. Data*, to be submitted.

(25) Huang, S. H.; Radosz, M. Equation of state for small, large, polydisperse, and associating molecules: Extension to fluid mixtures. *Industrial & Engineering Chemistry Research* **1991,** *30* (8), 1994-2005.

(26) Lemmon, E. W., Huber, M.L., McLinden, M.O. *NIST Standard Reference Database 23: Reference Fluid Thermodynamic and Transport Properties-REFPROP, Version 8.0*; National Institute of Standards and Technology: Gaithersburg, 2007.

(27) Kamerlingh Onnes, H. Expression of the equation of state of gases and liquids by means of series. KNAW, Proceedings, 4, 1901-1902, Amsterdam, 1902, pp. 125-147.

(28) Jaeschke, M.; Audibert, S.; van Caneghem, P.; Humphreys, E.E.; Janssen-van Rosmalen, R.; Pellei, Q.; Michels, J.P.J.; Schouten, J.A.; Ten Seldam, C.A. High accuracy compressibility factor calculation for natural gases and similar mixtures by use of a truncated virial equation, GERG Technical Monograph TM 2, 1989.

(29) Schouten, J. A.; Michels, J.P.J.; Jaeschke, M. Calculation of the compressibility factor of natural gases based on the calorific value and the specific gravity. *Intl J. of Thermophysics* **1990,** *11* (1), 145-156.

(30) Starling, K. E.; Savidge, J. L. Compressibility Factors of Natural Gas and Other Related Hydrocarbon Gases. *Transmission Measurement Committee Report No. 8*, AGA (American Gas Association). Arlington, VA., 1992.

(31) Hall, K. R.; Iglesias-Silva, G. A.; Mansoori, G. A. Quadratic mixing rules for equations of state: Origins and relationships to the virial expansion. *Fluid Phase Equilib.* **1993,** *91* (1), 67-76.

(32) Jorgensen, W. L.; Maxwell, D. S.; Tiradorives, J. Development and testing of the OPLS all-atom force field on conformational energetics and properties of organic liquids. *J. Am. Chem. Soc.* **1996,** *118*, 11225.

(33) Panagiotopoulos, A. Z. Direct determination of phase coexistence properties of fluids by Monte Carlo simulation in a new ensemble. *Mol Phys* **2002,** *100* (1), 237-246.

(34) Neubauer, B.; Tavitian, B.; Boutin, A.; Ungerer, P. Molecular simulations on volumetric properties of natural gas. *Fluid Phase Equilib.* **1999,** *161* (1), 45-62.

(35) Reiss, H.; Frisch, H. L.; Lebowitz, J. L. Statistical mechanics of rigid spheres. *The Journal of Chemical Physics* **1959,** *31* (2), 369-380.

(36) Heying, M.; Corti, D. S. Scaled particle theory revisited: New conditions and improved predictions of the properties of the hard sphere fluids. *The Journal of Physical Chemistry B* **2004,** *108* (51), 19756-19768.

(37) Boublík, T. The BACK equation of state for hydrogen and related compounds. *Fluid Phase Equilib.* **2006,** *240* (1), 96-100.

(38) Boublík, T. BACK equation of state for simple compounds. *Journal of Molecular Liquids* **2007,** *134* (1-3), 151-155.

(39) Lemmon, E. W.; McLinden, M. O.; Wagner, W. Thermodynamic properties of propane. III. A reference equation of state for temperatures from the melting line to 650 K and pressures up to 1000 MPa. *J. Chem. Eng. Data* **2009**, *54* (12), 3141–3180.

(40) Setzmann, U.; Wagner, W. A new equation of state and tables of thermodynamic properties for methane covering the range from the melting line to 625 K at pressures up to 100 MPa. *Journal of Physical and Chemical Reference Data* **1991,** *20* (6), 1061-1155.

(41) Span, R.; Lemmon, E. W.; Jacobsen, R. T.; Wagner, W. A reference quality equation of state for nitrogen. *Int. J. Thermophys.* **1998,** *19* (4), 1121-1132.

(42) Bucker, D.; Wagner, W. A reference equation of state for the thermodynamic properties of ethane for temperatures from the melting line to 675 K and pressures up to 900 MPa. *Journal of Physical and Chemical Reference Data* **2006,** *35* (1), 205-266.

(43) Cristancho, D.; Hall, K. R.; Lemmon, E. Fundamental equation of state for propylene glycol. *J. Chem. Eng. Data*, to be submitted.

(44) Cristancho, D.; Ullas, P.; Iglesias-Silva, G.; Hall, K.R. Quintic equation of state. *J. Chem. Eng. Data*, to be submitted.

(45) Prausnitz, J.M.; Gomes de Azevedo, E.; Litchtenthaler, R. *Molecular Thermodynamics of Fluid-Phase Equilibria*. 3 ed., Prentice Hall PTR, N.J., **1998**.

(46) Ejaz, S. High-accuracy P-ρ-T measurements of pure gas and natural gas like mixtures using a compact magnetic suspension densimeter. PhD. Dissertation, Texas A&M University, College Station, TX, 2007.

(47) Atilhan, M. High-accuracy P-ρ-T measurements up to 200 MPa between 200 K to 500 K using a single sinker magnetic suspension densitometer for pure and natural gas like mixtures. PhD. Dissertation, Texas A&M University, College Station, TX, 2007.

(48) Kleinrahm, R.; Duschek, W.; Wagner, W. (Pressure, density, temperature) measurements in the critical region of methane. *J. Chem. Thermodyn.* **1986,** *18* (12), 1103-1114.

(49) Kleinrahm, R.; Wagner, W. Measurement and correlation of the equilibrium liquid and vapour densities and the vapour pressure along the coexistence curve of methane. *J. Chem. Thermodyn.* **1986,** *18* (8), 739-760.

(50) Wagner, W.; Kleinrahm, R. Densimeters for very accurate density measurements of fluids over large ranges of temperature, pressure, and density. *Metrologia* **2004,** *41* (2), S24-S39.

(51) McLinden, M.; Kleinrahm, R.; Wagner, W. Force transmission errors in magnetic suspension densimeters. *Int. J. Thermophys.* **2007,** *28* (2), 429-448.

(52) Kano, Y.; Kayukawa, Y.; Fujii, K.; Sato, H. A new method for correcting a force transmission error due to magnetic effects in a magnetic levitation densimeter. *Measurement Science and Technology* **2007,** *18* (3), 659-666.

(53) Wagner, W.; Brachthäuser, K.; Kleinrahm, R.; Lösch, H. W. A new, accurate single-sinker densitometer for temperatures from 233 to 523 K at pressures up to 30 MPa. *Int. J. Thermophys.* **1995,** *16* (2), 399-411.

(54) McLinden, M. O.; Splett, J. D. A Liquid density standard over wide ranges of temperature and pressure based on toluene. *J. Res. Natl. Inst. Stand. Technol.* **2008,** *113* (1), 29-67.

(55) Patil, P.; Ejaz, S.; Atilhan, M.; Cristancho, D.; Holste, J. C.; Hall, K. R. Accurate density measurements for a 91% methane natural gas-like mixture. *J. Chem. Thermodyn.* **2007,** *39* (8), 1157-1163.

(56) Span, R.; Wagner, W. A new equation of state for carbon dioxide covering the fluid region from the triple-point temperature to 1100 K at pressures up to 800 MPa. *Journal of Physical and Chemical Reference Data* **1996,** *25* (6), 1509-1596.

(57) Span, R.; Lemmon, E. W.; Jacobsen, R. T.; Wagner, W.; Yokozeki, A. A reference equation of state for the thermodynamic properties of nitrogen for temperatures from 63.151 to 1000 K and pressures to 2200 MPa. *Journal of Physical and Chemical Reference Data* **2000,** *29* (6), 1361-1433.

(58) Trappeniers, N. J.; Wassenaar, T.; Abels, J. C. Isotherms and thermodynamic properties of methane at temperatures between 0-degrees-C and 150-degrees-C and at densities up to 570 amagat. *Physica A* **1979,** *98* (1-2), 289-297.

(59) Morris, E. C. Accurate measurements of the PVT properties of methane from — 20 to 150 °C and to 690 MPa. *Int. J. Thermophys.* **1984,** *5* (3), 281-290.

(60) Mollerup, J. Measurement of the volumetric properties of methane and ethene at 310 K at pressures to 70 MPa and of propene from 270 to 345 K at pressures to 3 MPa by the Burnett method. *J. Chem. Thermodyn.* **1985,** *17* (5), 489-499.

(61) Kortbeek, P. J.; Schouten, J. A. Measurements of the compressibility and sound velocity in methane up to 1 GPa, revisited. *Int. J. Thermophys.* **1990,** *11* (3), 455-466.

(62) Douslin, D. R.; Harrison, R. H.; Moore, R. T.; MuCullough, J. P. P-V-T relations for methane. *J. Chem. Eng. Data* **1964,** *9* (3), 358-363.

(63) Kleinrahm, R.; Duschek, W.; Wagner, W.; Jaeschke, M. Measurement and correlation of the (pressure, density, temperature) relation of methane in the temperature-range from 273.15-K to 323.15-K at pressures up to 8 Mpa. *J Chem Thermodyn* **1988,** *20* (5), 621-631.

(64) Brugge, H. B.; Hwang, C. A.; Rogers, W. J.; Holste, J. C.; Hall, K. R.; Lemming, W.; Esper, G. J.; Marsh, K. N.; Gammon, B. E. Experimental cross virial-coefficients for binary-mixtures of carbon-dioxide with nitrogen, methane and ethane at 300 and 320-K. *Physica A* **1989,** *156* (1), 382-416.

(65) Handel, G.; Kleinrahm, R.; Wagner, W. Measurements of the (pressure, density, temperature) relation of methane in the homogeneous gas and liquid regions in the temperature-range from 100-K to 260-K and at pressures up to 8 Mpa. *J Chem Thermodyn* **1992,** *24* (7), 685-695.

(66) Pal, A. K.; Pope, G. A.; Arai, Y.; Carnahan, N. F.; Kobayashi, R. Experimental pressure-volume-temperature relations for saturated and compressed fluid ethane. *J. Chem. Eng. Data* **2002,** *21* (4), 394-397.

(67) Golovskii, Y. A.; Mitsevich, E. P.; Tsymarnyy, V. A. *Measurements of propane density at temperatures 88.24-272.99 K and pressures up to 609.97 bar.* Deposited at the Institute VNIIEGasprom, No. 45, 1978. Data are given in: Sychev, V. V.; Vasserman, A. A.; Kozlov, A. D.; Tsymarny, V. A. *Thermodynamic Properties of Propane*; Hemisphere Publishing Corporation: New York, 1991.

(68) Byun, H. S.; DiNoia, T. P.; McHugh, M. A. High-pressure densities of ethane, pentane, pentane-d12, 25.5 wt ethane in pentane-d12, 2.4 wt deuterated poly(ethylene-co-butene) (PEB) in ethane, 5.3 wt hydrogenated PEB in pentane,

5.1 wt hydrogenated PEB in pentane-d12, and 4.9 wt hydrogenated PEB in pentane-d12 + 23.1 wt ethane. *J. Chem. Eng. Data* **2000,** *45* (5), 810-814.

(69) Funke, M.; Kleinrahm, R.; Wagner, W. Measurement and correlation of the (p, [rho], T) relation of ethane I. The homogeneous gas and liquid regions in the temperature range from 95 K to 340 K at pressures up to 12 MPa. *J. Chem. Thermodyn.* **2002,** *34* (12), 2001-2015.

(70) Mansoorian, H.; Hall, K. R.; Holste, J. C.; Eubank, P. T. The density of gaseous ethane and of fluid methyl chloride, and the vapor pressure of methyl chloride. *J. Chem. Thermodyn.* **1981,** *13* (11), 1001-1024.

(71) Barrufet, M. A. Studies on criticality phenomena and collinearity constraints. PhD. Disseration, Texas A&M University, College Station, TX, 1987.

(72) Griffiths, R. B.; Wheeler, J. C. Critical points in multicomponent systems. *Physical Review A* **1970,** *2* (3), 1047.

(73) Hall, K. R.; Eubank, P. T.; Myerson, A. S.; Nixon, W. E. New technique for collecting binary vapor-liquid-equilibrium data without measuring composition - method of intersecting isochores. *AIChE Journal* **1975,** *21* (6), 1111-1114.

(74) Hall, K. R.; Eubank, P. T. Rectilinearity rule for isochoric slopes issuing from coexistence curve. *Industrial & Engineering Chemistry Fundamentals* **1976,** *15* (1), 80-81.

(75) Joffrion, L. L.; Barrufet, M. A.; Eubank, P. T. Isochoric collinearity studies with density dependent mixing rules. *Fluid Phase Equilib.* **1989,** *48*, 209-222.

(76) Duarte-Garza, H. A.; Holste, J. C.; Hall, K. R.; Marsh, K. N.; Gammon, B. E. Isochoric pVT and phase equilibrium measurements for carbon dioxide + nitrogen. *J. Chem. Eng. Data* **2002,** *40* (3), 704-711.

(77) Zhou, J.; Patil, P.; Ejaz, S.; Atilhan, M.; Holste, J. C.; Hall, K. R. (p, Vm, T) and phase equilibrium measurements for a natural gas-like mixture using an automated isochoric apparatus. *J. Chem. Thermodyn.* **2006,** *38* (11), 1489-1494.

(78) Lau, W.W.R. A continuously weighed pycnometer providing densities for carbon dioxide+ethane mixtures between 240 and 350 K at pressures up to 35 MPa. Ph.D. Dissertation, Texas A&M, College Station, TX, 1986.

(79) Atilhan, M. High-Accuracy P-ρ-T measurements up to 200 MPa between 200 K to 500 K using a single sinker magnetic suspension densitometer for pure and

natural gas like mixtures. PhD. Dissertation, Texas A&M University, College Station, TX, 2005.

(80) Matabe, A. Effects of some design parameters on the accuracy of 'isochoric' measurements. M.S. Thesis, Texas A&M University, College Station, TX, 1999.

(81) Melvin, A. *Natural gas: Basic science and technology*. IOP Publishing Limited, Bristol, In Association with British Gas plc, London, **1988**.

(82) Warner Jr, H. R.; Leamer, E. E.; Spence, A. P.; Bone, R. L.; Hubbard, R. A.; Bernos, J.; Kriel, W. A. Hydrocarbon dew point determination of lean natural gases. Proceedings of the 80th annual meeting, Gas Processors Association, San Antonio, Texas, San Antonio, Texas, March, 2001.

(83) Biswas, S. N.; Seldam, C. A. T. Determination of the coexistence curve of sulfur hexafluoride from isochoric intercepts. *Fluid Phase Equilib.* **1989,** *47* (1), 67-75.

(84) Doiron, T.; Behringer, R. P.; Meyer, H. Equation of state of a3He-4He mixture near its liquid-vapor critical point. *Journal of Low Temperature Physics* **1976,** *24* (3), 345-363.

(85) Rowlinson, J. S.; Esper, G. J.; Holste, J. C.; Hall, K. R.; Barrufet, M. A.; Eubank, P. T. The Collinearity of isochores at single-phase and 2-phase boundaries for fluid mixtures. *Acs Sym Ser* **1986,** *300*, 42-59.

(86) Di Nicola, G.; Giuliani, G.; Passerini, G.; Polonara, F.; Stryjek, R. Vapor-liquid-equilibrium (VLE) properties of R-32+R-134a system derived from isochoric measurements. *Fluid Phase Equilib.* **1998,** *153* (1), 143-165.

(87) Montgomery, D.C.; Runger, G.C. *Applied Statistics and Probability for Engineers*. fourth ed.; John Wiley & Sons Inc.: Hoboken, N. J., 2007.

(88) Hall, K. R. Density data for synthetic natural gas mixtures. *J. Chem. Eng. Data*, to be submitted.

(89) George, D. L. Preparation of natual gas blends used as calibration standards: Sources of uncertainty and best preparation practices. Final Report, Southwest Research Institute, San Antonio, TX, 2003.

(90) Karplus, M.; Richards, N. *Atoms & molecules: An introduction for students of physical chemestry*. Menlo Park, CA, 1970.

(91) Pestov, D.; Murawski, R. K.; Ariunbold, G. O.; Wang, X.; Zhi, M.; Sokolov, A. V.; Sautenkov, V. A.; Rostovtsev, Y. V.; Dogariu, A.; Huang, Y.; Scully, M. O.

Optimizing the laser-pulse configuration for coherent raman spectroscopy. *Science* **2007,** *316* (5822), 265-268.

(92) Pestov, D. X., Wang; Cristancho, D.; Hall, K.R.; Sokolov, A.V.; Scully, M.O. Real-time sensing of gas phase mixtures via coherent raman spectroscopy. *Lasers and Electro-Optics, 2008 and 2008 Conference on Quantum Electronics and Laser Science. CLEO/QELS 2008*, 2008; pp 1-2.

(93) Hansen, S. B.; Berg, R. W.; Stenby, E. H. High-pressure measuring cell for raman spectroscopic studies of natural gas. *Applied Spectroscopy* **2001,** *55*, 55-60.

(94) Diller, D. E.; Chang, R. F. Composition of mixtures of natural gas components determined by raman spectrometry. *Applied Spectroscopy* **1980,** *34*, 411-414.

(95) Wopenka, B.; Pasteris, J. D. Limitations to quantitative analysis of fluid inclusions in geological samples by laser raman microprobe spectroscopy. *Applied Spectroscopy* **1986,** *40*, 144-151.

(96) American Gas Association. Orifice metering of natural gas and other related hydrocarbon fluids. Report No 3. American Gas Association: Washington, D.C., 2000.

(97) Lemmon, E. W.; Jacobsen, R. T. A generalized model for the thermodynamic properties of mixtures. *Int. J. Thermophys.* **1999,** *20* (3), 825-835.

(98) Cristancho, D. E.; Mantilla, I. D.; Ejaz, S.; Hall, K. R.; Atilhan, M.; Iglesia-Silva, G. A. Accurate PρT data for methane from (300 to 450) K up to 180 MPa. *J Chem Eng Data* **2009**, DOI: 10.1021/je9004849.

(99) Cristancho, D. E.; Mantilla, I. D.; Ejaz, S.; Hall, K. R.; Atilhan, M.; Iglesia-Silva, G. A. Accurate PρT data for ethane from (298 to 450) K up to 200 MPa. *J. Chem. Eng. Data*, **2009**, DOI: 10.1021/je900978x.

(100) Mantilla, I. D.; Cristancho, D. E.; Ejaz, S.; Hall, K. R.; Atilhan, M.; Iglesia-Silva, G. A. Accurate PρT Data for nitrogen from (250 to 450) K up to 200 MPa. *J. Chem. Eng. Data*, to be submitted.

(101) Mantilla, I. D.; Cristancho, D. E.; Ejaz, S.; Hall, K. R.; Atilhan, M.; Iglesia-Silva, G. A. Accurate PρT data for carbon dioxide from (300 to 450) K up to 200 MPa. *J. Chem. Eng. Data*, submitted.

(102) Starling, K.E.; Savidge, J.L. *Compressibility Factors of Natural Gas and Other Related Hydrocarbon Gases*. American Gas Association, Arlington, VA, 1992.

(103) Haynes, W. M. Measurements of orthobaric-liquid densities of multicomponent mixtures of components (N2, CH4, C2H6, C3H8, CH3CH(CH3)CH3, C4H10, CH3CH(CH3)C2H5, and C5H12) between 110 and 130 K. *J. Chem. Thermodyn.* **1982,** *14* (7), 603-612.

(104) Ungerer, P.; Tavitian, B.; Boutin, A. *Applications of Molecular Simulation in the Oil and Gas Industry. Monte Carlo Methods*. IFP Publications: Paris, 2005.

(105) Leonhard, K.; Van Nhu, N.; Lucas, K. Making equation of state models predictive: Part 2: An improved PCP-SAFT equation of state. *Fluid Phase Equilib.* **2007,** *258* (1), 41-50.

(106) Singh, M.; Leonhard, K.; Lucas, K. Making equation of state models predictive: Part 1: Quantum chemical computation of molecular properties. *Fluid Phase Equilib.* **2007,** *258* (1), 16-28.

(107) Aparicio-Martinez, S.; Hall, K. R. Use of PC-SAFT for global phase diagrams in binary mixtures relevant to natural gases. 2. n-alkane plus other hydrocarbons. *Industrial & Engineering Chemistry Research* **2007,** *46* (1), 285-290.

(108) Aparicio-Martinez, S.; Hall, K. R. Use of PC-SAFT for global phase diagrams in binary mixtures relevant to natural gases. 3. Alkane plus non-hydrocarbons. *Industrial & Engineering Chemistry Research* **2007,** *46* (1), 291-296.

(109) del Río, F.; Guzmán, O.; Eloy Ramos, J.; Ibarra-Tandi, B. Effective intermolecular potentials in theoretical thermodynamics of pure substances and solutions. *Fluid Phase Equilib.* **2007,** *259* (1), 9-22.

(110) Boublik, T. Hard convex body equation of state. *The Journal of Chemical Physics* **1975,** *63* (9), 4084-4084.

(111) Wendland, M.; Saleh, B.; Fischer, J. Accurate thermodynamic properties from the BACKONE equation for the processing of natural gas. *Energy & Fuels* **2004,** *18* (4), 938-951.

(112) Gross, J.; Sadowski, G. Perturbed-chain SAFT: An equation of state based on a perturbation theory for chain molecules. *Industrial & Engineering Chemistry Research* **2001,** *40* (4), 1244-1260.

(113) Boukouvalas, C. J.; Magoulas, K. G.; Tassios, D. P.; Kikic, I. Comparison of the performance of the LCVM model (an EoS/GE model) and the PHCT EoS (the perturbed hard chain theory equation of state) in the prediction of the vapor-

liquid equilibria of binary systems containing light gases. *The Journal of Supercritical Fluids* **2001,** *19* (2), 123-132.

(114) Huang, S. H.; Radosz, M. Equation of state for small, large, polydisperse, and associating molecules. *Industrial & Engineering Chemistry Research* **2002,** *29* (11), 2284-2294.

(115) Huang, S. H.; Radosz, M. Equation of state for small, large, polydisperse, and associating molecules: Extension to fluid mixtures. *Industrial & Engineering Chemistry Research* **2002,** *30* (8), 1994-2005.

(116) Jorgensen, W. L. Theoretical studies of medium effects on conformational equilibria. *The Journal of Physical Chemistry* **2002,** *87* (26), 5304-5314.

(117) Jorgensen, W. L.; Tirado-Rives, J. The OPLS [optimized potentials for liquid simulations] potential functions for proteins, energy minimizations for crystals of cyclic peptides and crambin. *Journal of the American Chemical Society* **2002,** *110* (6), 1657-1666.

(118) Klauda, J. B.; Pastor, R. W.; Brooks, B. R. Adjacent gauche stabilization in linear alkanes: Implications for polymer models and conformational analysis. *The Journal of Physical Chemistry B* **2005,** *109* (33), 15684-15686.

(119) Tsige, M.; Curro, J. G.; Grest, G. S.; McCoy, J. D. Molecular dynamics simulations and integral equation theory of alkane chains: Comparison of explicit and united atom models. *Macromolecules* **2003,** *36* (6), 2158-2164.

(120) Toxvaerd, S. Equation of state of alkanes II. *The Journal of Chemical Physics* **1997,** *107* (13), 5197-5204.

(121) Toxvaerd, S. Molecular dynamics calculation of the equation of state of alkanes. *The Journal of Chemical Physics* **1990,** *93* (6), 4290-4295.

(122) Schuler, L. D.; Daura, X.; Van Gunsteren, W. F. An improved GROMOS96 force field for aliphatic hydrocarbons in the condensed phase. *J. Comput. Chem.* **2001,** *22*, 1205.

(123) Alder, B. J.; Young, D. A.; Mark, M. A. Studies in molecular dynamics. X. Corrections to the augmented van der Waals theory for the square well fluid. *The Journal of Chemical Physics* **1972,** *56* (6), 3013-3029.

(124) Assink, R. A. Molecular dynamics of octane in a gas liquid solution. *The Journal of Chemical Physics* **1975,** *62* (3), 790-794.

(125) Cinacchi, G.; Schmid, F. Density functional for anisotropic fluids. *Journal of Physics: Condensed Matter* **2002,** *14* (46), 12223-12234.

(126) Gloor, G. J.; Jackson, G.; Blas, F. J.; del Rio, E. M.; de Miguel, E. An accurate density functional theory for the vapor-liquid interface of associating chain molecules based on the statistical associating fluid theory for potentials of variable range. *The Journal of Chemical Physics* **2004,** *121* (24), 12740-12759.

(127) Lowen, H. Density functional theory of inhomogeneous classical fluids: recent developments and new perspectives. *Journal of Physics: Condensed Matter* **2002,** *14* (46), 11897-11905.

(128) Rosenfeld, Y. Phase separation of asymmetric binary hard-sphere fluids: Self-consistent density functional theory. *Physical Review Letters* **1994,** *72* (24), 3831.

(129) Tsuzuki, S.; Uchimaru, T.; Tanabe, K. Conformational analysis of *n*-alkanes using density functional theory: Comparison with ab initio calculations *Chem. Phys. Lett.* **1995,** *246*, 9-12.

(130) Frisch, M. J.; Trucks, G. W.; Schlegel, H. B.; Scuseria, G. E.; Robb, M. A.; Cheeseman, J. R.; Montgomery, J. A.; Vreven, T.; Kudin, K. N.; Burant, J. C.; Millam, J. M.; Iyengar, S. S.; Tomasi, J.; Barone, V.; Mennucci, B.; Cossi, M.; Scalmani, G.; Rega, N.; Petersson, G. A.; Nakatsuji, H.; Hada, M.; Ehara, M.; Toyota, K.; Fukuda, R.; Hasegawa, J.; Ishida, M.; Nakajima, T.; Honda, Y.; Kitao, O.; Nakai, H.; Klene, M.; Li, X.; Knox, J. E.; Hratchian, H. P.; Cross, J. B.; Bakken, V.; Adamo, C.; Jaramillo, J.; Gomperts, R.; Stratmann, R. E.; Yazyev, O.; Austin, A. J.; Cammi, R.; Pomelli, C.; Ochterski, J. W.; Ayala, P. Y.; Morokuma, K.; Voth, G. A.; Salvador, P.; Dannenberg, J. J.; Zakrzewski, V. G.; Dapprich, S.; Daniels, A. D.; Strain, M. C.; Farkas, O.; Malick, D. K.; Rabuck, A. D.; Raghavachari, K.; Foresman, J. B.; Ortiz, J. V.; Cui, Q.; Baboul, A. G.; Clifford, S.; Cioslowski, J.; Stefanov, B. B.; Liu, G.; Liashenko, A.; Piskorz, P.; Komaromi, I.; Martin, R. L.; Fox, D. J.; Keith, T.; Laham, A.; Peng, C. Y.; Nanayakkara, A.; Challacombe, M.; Gill, P. M. W.; Johnson, B.; Chen, W.; Wong, M. W.; Gonzalez, C.; Pople, J. A., Gaussian 03, Revision C.02. Gaussian, Inc., Wallingford, CT, 2004.

(131) Curik, R.; Carsky, P.; Allan, M. Vibrational excitation of methane by slow electrons revisited: Theoretical and experimental study. *Journal of Physics B: Atomic, Molecular and Optical Physics* **2008,** *41* (11), 115203.

(132) Bartell, L. S.; Kohl, D. A. Structure and rotational isomerization of free hydrocarbon chains. *The Journal of Chemical Physics* **1963,** *39* (11), 3097-3105.

APPENDIX A

PRESSURE TRANSDUCER CALIBRATION COEFFICIENTS

Transducer model: 430K-101

Serial Number: 102124

Temperature Coefficients

X = temperature period (μs)

$U = X - U_0$

Temperature : (deg C)

$Temp = Y_1U + Y_2U^2 + Y_3U^3$

Table A.1. Temperature Coefficients

U_0	5.840168 μsec
Y_1	-3923.084 deg C/ μsec
Y_2	-8226.233 deg C/ μsec^2
Y_3	0

Pressure Coefficients

T = pressure period (μsec)

$C = C_1 + C_2U + C_3U^2$

$D = D_1 + D_2U$

$T_0 = T_1 + T_2U + T_3U^2 + T_4U^3 + T_5U^4$

Pressure : (psia)

$P = C (1- T_0^2/T^2) (1 – D (1 - T_0^2/T^2))$

Table A.2 Pressure Coefficients

C_1	-182594.0 psia
C_2	-13644.09 psia/ μsec
C_3	661604.7 psia/ μsec^2

Table A.3 Pressure Coefficients

D_1	0.015583
D_2	0

Table A. 4 Pressure Coefficients

T_1	29.94125 μsec
T_2	1.040748 μsec/ μsec
T_3	66.89682 μsec/ μsec^2
T_4	-44.90226 μsec/ μsec^3
T_4	0

APPENDIX B

PRT CALIBRATION and ITS-90 COEFFICIENTS

The International Temperature Scale (ITS-90) is designed to characterize the absolute thermodynamic scale in the range of 0.65 K to 1358 K. ITS-90 expresses the temperature in Kelvin in terms of the ratio of the measured resistance of the PRT at the temperature and its resistance at triple point of water; 273.16 K:

$$W(T) = \frac{R(T)}{R(273.16\mathrm{K})} \tag{B.1}$$

The deviation equation given by equation D.2 and reference function given by equation D.3 are used to calculate the temperature below 273.16 K.

$$W_{\mathrm{ref}}(T) = W(T) - a_4[W(T)-1] - b_4[W(T)-1]\ln W(T) \tag{B.2}$$

$$\frac{T}{273.16K} = B_0 + \sum_{1}^{15} B_i \left[\frac{W_{\mathrm{ref}}(T)^{1/6} - 0.65}{0.35}\right]^i \tag{B.3}$$

The deviation equation given by equation B.4 and the reference function given by equation D.5 is used to calculate the temperature above 273.16 K.

$$W_{\mathrm{ref}}(T) = W(T) - a_8[W(T)-1] - b_8[W(T)-1]^2 \tag{B.4}$$

$$T - 273.15K = D_0 + \sum_{1}^{9} D_i \left[\frac{W_{\mathrm{ref}}(T) - 2.64}{1.64}\right]^i \tag{B.5}$$

The constants a_4, b_4, a_8 and b_8 were determined by Minco by calibrating the PRT at fixed temperature points defined by ITS-90. These constants and values of the constants B_i and D_i are given in Table B.1. The resistance of the PRT at the triple point of water measured during the original calibration done by Minco is R (273.16K) = 99.99731 Ω and the ratio R (373.15) / R (273.15) = 1.3927.

TABLE B.1 Constants in Deviation Equations and Reference Functions of ITS-90

a8	-1.3927129D-04	B(0)	+0.183324722
b8	-6.8843579D-04	B(1)	+0.240975303
a4	-7.0279407D-04	B(2)	+0.209108771
b4	-9.5605690D-06	B(3)	+0.190439972
		B(4)	+0.142648498
D(0)	+439.932854	B(5)	+0.077993465
D(1)	+472.418020	B(6)	+0.012475611
D(2)	+37.684494	B(7)	-0.032267127
D(3)	+7.472018	B(8)	-0.075291522
D(4)	+2.920828	B(9)	-0.056470670
D(5)	+0.005184	B(10)	+0.076201285
D(6)	-0.963864	B(11)	+0.123893204
D(7)	-0.188732	B(12)	-0.029201193
D(8)	+0.191203	B(13)	-0.091173542
D(9)	+0.049025	B(14)	+0.001317696
		B(15)	+0.026025526

APPENDIX C

ISOCHORIC DATA FOR THE SYNTHETIC NARURAL GAS SAMPLES

RESULTS FOR SAMPLE 1

Table C1. Isochoric Results for Sample 1. Black: Single Phase; Blue: Two Phase

Isochore 1		Isochore 2		Isochore 3		Isochore 4		Isochore 5	
T / K	P / MPa	T / K	P / MPa	T / K	P / MPa	T / K	P / MPa	T / K	P / MPa
343.15	21.236	343.15	17.924	343.15	15.561	343.15	12.663	343.15	9.876
333.15	20.088	333.15	17.010	333.15	14.820	333.15	12.097	333.15	9.471
323.15	18.937	323.15	16.088	323.15	14.056	323.15	11.529	323.15	9.064
313.15	17.781	313.15	15.165	313.15	13.296	313.15	10.956	313.15	8.654
303.15	16.617	303.15	14.241	303.15	12.533	303.15	10.378	303.15	8.241
293.15	15.455	293.15	13.313	293.15	11.763	293.15	9.800	293.15	7.827
283.15	14.280	283.15	12.387	283.15	10.994	283.15	9.224	283.15	7.414
273.15	13.112	273.15	11.453	273.15	10.229	273.15	8.648	273.15	7.000
263.15	12.017	263.15	10.528	263.15	9.469	263.15	8.075	263.15	6.602
258.15	11.383	258.15	10.076	258.15	9.096	258.15	7.792	258.15	6.392
253.15	10.816	253.15	9.601	253.15	8.726	253.15	7.507	253.15	6.188
248.15	10.222	248.15	9.137	248.15	8.334	248.15	7.221	248.15	5.991
243.15	9.630	243.15	8.665	243.15	7.955	243.15	6.947	243.15	5.795
238.15	9.066	238.15	8.203	238.15	7.585	238.25	6.689	238.25	5.606
233.15	8.463	233.15	7.762	233.15	7.227	233.50	6.433		
228.15	7.882	228.15	7.341	228.15	6.871	228.15	6.150		
223.15	7.353	223.15	6.927	223.15	6.514				
218.15	6.867	218.15	6.521						
213.25	6.398								

Table C1. Continued

Isochore 6		Isochore 7		Isochore 8	
T / K	P / MPa	T / K	P / MPa	T / K	P / MPa
343.15	7.272	343.15	4.449	343.15	2.290
333.15	6.998	333.15	4.298	333.15	2.218
323.15	6.723	323.15	4.146	323.15	2.146
313.15	6.447	313.15	3.992	313.15	2.073
303.15	6.168	303.15	3.839	303.15	2.000
293.15	5.889	293.15	3.684	293.15	1.926
283.15	5.609	283.15	3.529	283.15	1.852
273.15	5.330	273.15	3.374	273.15	1.776
263.15	5.052	263.15	3.216	263.15	1.702
258.15	4.917	258.15	3.139	258.15	1.666
253.15	4.780	253.15	3.063	253.15	1.629
248.15	4.640	248.15	2.984	248.15	1.593
243.15	4.507	243.15	2.903	243.15	1.555
238.15	4.374	238.15	2.821	238.15	1.517
		233.15	2.741	233.15	1.478
				228.15	1.439

RESULTS FOR SAMPLE 2

Table C2. Isochoric Results for Sample 2. Black: Single Phase; Blue: Two Phase

Isochore 1		Isochore 2		Isochore 3		Isochore 4		Isochore 5		Isochore 6	
T / K	P / MPa	T / K	P / MPa	T / K	P / MPa	T / K	P / MPa	T / K	P / MPa	T / K	P / MPa
343.15	24.712	343.15	21.264	343.15	17.645	343.15	15.166	343.15	12.227	343.15	10.008
333.15	23.287	333.15	20.081	333.15	16.751	333.15	14.438	333.15	11.678	333.15	9.592
323.15	21.861	323.15	18.898	323.15	15.854	323.15	13.705	323.15	11.128	323.15	9.177
313.15	20.419	313.15	17.716	313.15	14.953	313.15	12.969	313.15	10.583	313.15	8.760
308.15	19.728	303.15	16.533	303.15	14.047	303.15	12.229	303.15	10.033	303.15	8.338
303.15	19.002	293.15	15.350	293.15	13.134	293.15	11.488	293.15	9.481	293.15	7.917
293.15	17.585	283.15	14.167	283.15	12.216	283.15	10.749	283.15	8.932	283.15	7.497
283.15	16.156	273.15	12.984	273.15	11.303	278.15	10.375	278.15	8.656	278.15	7.285
273.15	14.739	263.15	11.803	263.15	10.443	273.15	10.007	273.15	8.381	273.15	7.075
263.15	13.339	253.15	10.617	253.15	9.523	271.15	9.861	271.15	8.272	271.15	6.991
253.15	11.906	243.15	9.437	248.15	9.075	269.15	9.711	269.15	8.163	269.15	6.909
243.15	10.449	238.15	8.885	243.15	8.662	267.15	9.563	267.15	8.055	267.15	6.825
238.15	9.733	233.15	8.377	238.15	8.247	265.15	9.418	265.15	7.947	265.15	6.742
233.15	9.007	228.15	7.872	234.60	7.947	263.15	9.272	264.15	7.890	264.15	6.700
228.15	8.368	223.15	7.351	229.00	7.490	262.15	9.199	263.15	7.835	263.15	6.659
223.15	7.757	218.15	6.850	223.15	7.011	261.15	9.125	262.15	7.781	262.15	6.620
218.15	7.147	213.15	6.360			260.15	9.052	261.15	7.726	261.15	6.580
213.15	6.555					259.15	8.976	260.15	7.677	260.15	6.541
						258.15	8.902	259.15	7.629		
						257.15	8.829	258.15	7.581		
						256.15	8.757				
						255.15	8.684				
						254.15	8.617				
						253.15	8.551				

Table C2. Continued

Isochore 7		Isochore 8		Isochore 9	
T / K	P / MPa	T / K	P / MPa	T / K	P / MPa
343.15	7.735	343.15	5.582	343.15	3.329
333.15	7.433	333.15	5.380	333.15	3.217
323.15	7.131	323.15	5.177	323.15	3.105
313.15	6.831	313.15	4.973	313.15	2.992
303.15	6.530	303.15	4.771	303.15	2.881
293.15	6.229	293.15	4.571	293.15	2.769
283.15	5.929	283.15	4.368	283.15	2.658
278.15	5.776	278.15	4.266	278.15	2.601
273.15	5.625	273.15	4.164	273.15	2.546
271.15	5.565	271.15	4.123	271.15	2.522
269.15	5.505	269.15	4.083	269.15	2.500
267.15	5.445	267.15	4.042	267.15	2.477
265.15	5.385	265.15	4.002	265.15	2.455
264.15	5.356	264.15	3.982	264.15	2.444
263.15	5.326	263.15	3.961	263.15	2.433
262.15	5.297	262.15	3.939	262.15	2.421
261.15	5.267	261.15	3.918	261.15	2.410
260.15	5.239	260.15	3.896	260.15	2.399
				259.15	2.387
				258.15	2.375
				257.15	2.362

RESULTS FOR SAMPLE 3

Table C3. Isochoric Results for Sample 3. Black: Single Phase; Blue: Two Phase

Isochore 1		Isochore 2		Isochore 3		Isochore 4		Isochore 5	
T / K	P / MPa	T / K	P / MPa	T / K	P / MPa	T / K	P / MPa	T / K	P / MPa
323.15	20.829	343.15	21.114	343.15	18.470	343.15	14.803	343.15	11.873
313.15	19.506	333.15	19.976	333.15	17.525	333.15	14.096	333.15	11.350
303.15	18.172	323.15	18.828	323.15	16.569	323.15	13.387	323.15	10.825
293.15	16.836	313.15	17.675	313.15	15.605	313.15	12.675	313.15	10.298
283.15	15.495	303.15	16.516	303.15	14.636	303.15	11.958	303.15	9.769
273.15	14.151	293.15	15.348	293.15	13.660	293.15	11.236	293.15	9.238
263.15	12.826	283.15	14.177	283.15	12.685	283.15	10.522	283.15	8.709
258.15	12.222	273.15	13.006	273.15	11.708	278.15	10.162	278.15	8.445
253.15	11.542	263.15	11.914	263.15	10.742	273.15	9.804	273.15	8.183
243.15	10.182	253.15	10.731	253.15	9.808	271.15	9.662	271.15	8.079
238.15	9.555	243.15	9.621	243.15	8.883	269.15	9.521	269.15	7.975
233.15	8.943	238.15	9.078	238.15	8.429	267.15	9.382	267.15	7.872
228.15	8.358	233.15	8.537	233.24	7.979	265.15	9.241	265.15	7.771
223.21	7.773	228.15	8.015	228.40	7.541	263.15	9.102	263.15	7.670
218.37	7.210	223.15	7.496	223.55	7.123	262.15	9.038	262.15	7.621
213.50	6.634	218.15	6.981			261.15	8.977		
		213.29	6.456						

Table C3. Continued

Isochore 6		Isochore 7		Isochore 8	
T / K	P / MPa	T / K	P / MPa	T / K	P / MPa
343.15	9.262	343.15	6.724	343.15	4.414
333.15	8.884	333.15	6.474	333.15	4.263
323.15	8.507	323.15	6.224	323.15	4.111
313.15	8.128	313.15	5.972	313.15	3.958
303.15	7.748	303.15	5.717	303.15	3.805
293.15	7.367	293.15	5.463	293.15	3.650
283.15	6.989	283.15	5.210	283.15	3.496
278.15	6.800	278.15	5.083	278.15	3.418
273.15	6.610	273.15	4.957	273.15	3.341
271.15	6.536	271.15	4.906	271.15	3.311
269.15	6.461	269.15	4.854	269.15	3.279
267.15	6.386	267.15	4.803	267.15	3.247
265.15	6.312	266.15	4.777	265.15	3.214
263.15	6.241	265.15	4.750	264.15	3.198
		264.15	4.725	263.15	3.182
		263.15	4.698		

RESULTS FOR SAMPLE 4

Table C4. Isochoric Results for Sample 4. Black: Single Phase; Blue: Two Phase

Isochore 1		Isochore 2		Isochore 3		Isochore 4		Isochore 5	
T / K	P / MPa	T / K	P / MPa	T / K	P / MPa	T / K	P / MPa	T / K	P / MPa
343.15	21.395	343.15	18.614	343.15	14.846	343.15	12.059	343.15	9.331
333.15	20.150	333.15	17.584	333.15	14.101	333.15	11.505	333.15	8.933
323.15	18.912	323.15	16.564	323.15	13.357	323.15	10.947	323.15	8.541
313.15	17.671	313.15	15.541	313.15	12.611	313.15	10.389	313.15	8.148
303.15	16.435	303.15	14.515	303.15	11.862	303.15	9.823	303.15	7.754
293.15	15.183	293.15	13.488	293.15	11.105	293.15	9.263	293.15	7.360
283.15	13.939	283.15	12.455	283.15	10.359	283.15	8.706	283.15	6.967
278.15	13.321	278.15	11.946	278.15	9.987	278.15	8.434	278.15	6.778
273.15	12.702	273.15	11.430	273.15	9.629	273.15	8.171	273.15	6.590
268.15	12.075	268.15	10.937	270.15	9.413	271.15	8.063	271.15	6.513
264.15	11.604	264.15	10.542	268.15	9.277	269.15	7.960	269.15	6.440
263.15	11.494	263.15	10.440	266.15	9.131	267.15	7.849	267.15	6.364
262.15	11.385	262.15	10.345	264.15	8.988	265.15	7.742	265.15	6.289
261.15	11.275	261.15	10.249	262.15	8.845				

Table C4. Continued

Isochore 6		Isochore 7		Isochore 8	
T / K	P / MPa	T / K	P / MPa	T / K	P / MPa
343.15	6.981	343.15	4.448	343.15	2.054
333.15	6.713	333.15	4.292	333.15	1.989
323.15	6.443	323.15	4.134	323.15	1.922
313.15	6.172	313.15	3.976	313.15	1.854
303.15	5.900	303.15	3.818	303.15	1.788
293.15	5.626	293.15	3.659	293.15	1.720
283.15	5.352	283.15	3.499	283.15	1.652
278.15	5.217	278.15	3.419	278.15	1.618
273.15	5.081	273.15	3.336	273.15	1.584
271.15	5.026	271.15	3.303	271.15	1.567
269.15	4.971	269.15	3.270	269.15	1.549
267.15	4.917	267.15	3.237	267.15	1.533
265.15	4.863	265.15	3.204	265.15	1.517
263.15	4.808	263.15	3.170	263.15	1.500

VITA

Diego Edison Cristancho Blanco is a son of Jose Rafael Cristancho, Audrey Blanco and younger brother of Deissy Cristancho and Byron Cristancho.

Diego Edison Cristancho Blanco has both a B.S. in chemical engineering and a B.S. in physics from the Industrial University of Santander, Colombia. He also has a M.S. in chemical engineering from the same university. He was a member of the Environmental Research Center of the Industrial University of Santander as a technical advisor for about three years. At the same time, he was part of the Gravitational and Cosmology research group in the Physics department. From 2002 to 2005, he taught courses in both the Chemical Engineering and the Physics departments. During his doctoral studies, he has had the opportunity to work for industry as an intern covering projects related to industrial software applications and supercritical extraction. Recently, he worked at the National Institute of Standards and Technology (NIST) in Boulder, Colorado developing a new fundamental equation of state for propylene glycol. He graduated with his Ph.D. in chemical engineering at Texas A&M University in May 2010.

Diego Edison Cristancho Blanco is married to Jennifer Carvajal. His wife is also pursuing a Ph.D. degree in the Department of Chemical Engineering at Texas A&M University.

Dr. Cristancho can be reached through Dr. Kenneth R Hall, Department of Chemical Engineering, Texas A&M University, College Station, TX 77843-3122. His email is: krhall@tamu.edu.